

The role of heparan sulfate glycosaminoglycan supplementation in periodontitis

Duplančić, Roko

Doctoral thesis / Disertacija

2023

Degree Grantor / Ustanova koja je dodijelila akademski / stručni stupanj: **University of Split, School of Medicine / Sveučilište u Splitu, Medicinski fakultet**

Permanent link / Trajna poveznica: <https://um.nsk.hr/um:nbn:hr:171:935856>

Rights / Prava: [In copyright](#) / [Zaštićeno autorskim pravom.](#)

Download date / Datum preuzimanja: **2025-03-10**



Repository / Repozitorij:

[MEFST Repository](#)



**UNIVERSITY OF SPLIT
SCHOOL OF MEDICINE**

Roko Duplančić

**THE ROLE OF HEPARAN SULFATE GLYCOSAMINOGLYCAN
SUPPLEMENTATION IN PERIODONTITIS**

Doctoral dissertation

Mentor: Darko Kero, DMD, PhD

Split, 2023.

Research included in this doctoral dissertation was conducted in the periodontology clinics of *Department of Maxillofacial Surgery of University Hospital of Split* and the *Department of Periodontology of University of Zagreb, School of Dentistry* where biological samples were collected. Further processing of the samples was performed in the laboratories of the *Department of Anatomy, Histology and Embryology of University of, Split School of Medicine* and *Mediterranean Institute for Life Sciences* in Split.

The head of research was associate professor Darko Kero, DMD, PhD.

ACKNOWLEDGMENTS

Seven years have passed since I wrote an acknowledgment like this, and it was a part of my first master's thesis. A lot has happened and changed in the meantime, but I would still like to extend my gratitude to all the professors and colleagues who guided me towards new knowledge and skills. If it weren't for them – I'd miss out on a lot of tips and tricks.

I am also going to mention my friends and family again. Their thoughts, ideas and shared memories made me who I am today. I will not mention anyone by name but there is one person I am most grateful for, one who is closest to me – my wife. So special thanks go to Mia for putting up with my extremes: be they potentially lethal hobbies or late-night hours at the dental practice. If it weren't for her – I'd develop a rather different lifestyle.

Special thanks are in order for a group of three more people who helped me in the development of my academic character. Firstly, that's my mentor, Darko Kero who had endless patience for my hybrid way of dealing with the whole process. The second acknowledgment is basically shared between my "academic mothers" Renata Pecotić and Katarina Vukojević. They, all in their own unique way, helped me a lot in my professional development. If it weren't for them – I'd miss out on some very important guidance.

I would also like to express my thanks to all the people that were in some way a part of the development of any two-wheeled vehicles. If it weren't for them – instead of completing this dissertation in time, I'd still be trying to find a free parking space.

In the end, you cannot do things right if you don't make some enemies along the way, but I cannot phrase it better than Oscar Wilde: "Some cause happiness wherever they go; others, whenever they go.". On that note, I would like to point out that academia is not what I pictured seven years ago but I am going to try to justify taxpayers' further investment in me and persist to change things for the better.

Roko Duplančić

CONTENTS

1. LIST OF ABBREVIATIONS AND ACRONYMS	2
2. POOLED ARTICLES OVERVIEW	3
2.1. INTRODUCTION, RESEARCH PROBLEMATICS AND AIMS	4
2.2. MATERIALS AND METHODS OVERVIEW	9
2.2.1. PARTICIPANTS SCREENING AND RECRUITMENT	9
2.2.2. TISSUE SAMPLES COLLECTION	9
2.2.3. TISSUE SAMPLES PROCESSING	10
2.2.4. SAMPLE STAINING.....	11
2.2.5. IMAGE ACQUISITION AND PROCESSING	12
2.2.6. SIGNAL QUANTIFICATION AND IMAGE ANALYSIS	16
2.2.7. STATISTICAL ANALYSIS AND MODELING.....	16
2.3. RESULTS OVERVIEW.....	19
2.3.1. FIRST ARTICLE.....	19
2.3.2. SECOND ARTICLE	24
2.3.3. THIRD ARTICLE	27
2.4. DISCUSSION.....	33
2.5. CONCLUSIONS.....	38
2.6. ABSTRACT	39
2.7. SAŽETAK.....	40
2.8. CURRICULUM VITAE	41
2.9. LITERATURE	44
3. POOLED ARTICLES	53

1. LIST OF ABBREVIATIONS AND ACRONYMS

ECM – extracellular matrix

HS – heparan sulfate

GAG – glycosaminoglycan

PG – proteoglycan

Sdc – syndecan

NET – neutrophil extracellular trap

EXT – exostosin

NDST – N-Deacetylase and N-Sulfotransferase

HPSE – heparanase

SULF – sulfatase

RANKL / TNFSF11 – receptor activator of nuclear factor kappa-B ligand

OPG / TNFRSF11B – osteoprotegerin

IHC – immunohistochemistry

IF – immunofluorescence

BF – brightfield

H&E – hematoxylin and eosin

AB – Alcian Blue

DAPI – 4',6-diamidino-2-phenylindole

dpi – dots per inch

px – pixel

GV – grey value

ROI – region of interest

T-D – top-down

SplR – spline regression

MLR – multiple linear regression

2. POOLED ARTICLES OVERVIEW

- Duplancic R, Roguljic M, Puhar I, Veccek N, Dragun R, Vukojevic K, et al. **Syndecans and enzymes for heparan sulfate biosynthesis and modification differentially correlate with presence of inflammatory infiltrate in periodontitis.** *Frontiers in Physiology.* 2019;10:1248.
- Duplancic R, Kero D. **Novel approach for quantification of multiple immunofluorescent signals using histograms and 2D plot profiling of whole-section panoramic images.** *Scientific Reports.* 2021;11(1):8619.
- Duplancic R, Roguljic M, Bozic D, Kero D. **Heparan sulfate glycosaminoglycan is predicted to stabilize inflammatory infiltrate formation and RANKL/OPG ratio in severe periodontitis in humans.** *Bioengineering.* 2022;9(10):566.

2.1. INTRODUCTION, RESEARCH PROBLEMATIC AND AIMS

Periodontitis is a chronic inflammatory disease that affects the supporting tissues of the teeth, including the gingiva, periodontal ligament, and alveolar bone. In severe forms of periodontitis these tissues are gradually degraded, leading to a permanent reduction/loss of masticatory function. The etiology of periodontitis is multifactorial and involves various demographic and environmental risk factors (age, smoking, poor oral hygiene), infectious agents (chronic bacterial and endotoxin exposure from the microbial biofilm on the tooth surface), and host traits (genetic and epigenetic) (1, 2). These factors collectively influence the host's inflammatory response. Inadequate immune response to microbial biofilm on the tooth surface perpetuates a vicious cycle of inflammation and breakdown of periodontal tissue, which if left untreated, can ultimately result in tooth loss (3). Severe forms of periodontitis are one of the most common chronic infectious diseases in the world with worldwide prevalence estimated at 11% (4, 5). Current gold standard for the treatment of periodontitis (initial therapy) is based on nonsurgical mechanical removal of the supra- and subgingival microbial biofilm from the surfaces of the affected teeth and, in some cases, application of antimicrobials with antiseptic and/or antibiotic effect (6, 7). Initial therapy is aimed at calming the inflammation in order to slow down or completely stop the degradation of the supporting tissues of the teeth. Apart from the initial therapy, various forms of regenerative therapy procedures can also be applied for the treatment of advanced forms of periodontitis to reverse the periodontal tissue damage. Since chronically inflamed periodontal tissues exhibit persistent degradation of the extracellular matrix (ECM) components, another way to treat periodontitis is to supplement ECM or ECM components by their natural or synthetic derivatives. This approach (which is combined with surgical procedures) utilizes bone grafts (of natural or synthetic origin) and substances based on decellularized natural ECM such as *Emdogain*[®] (a derivative of enamel matrix protein) (8-10). Substances based on glycosaminoglycans (GAGs), such as hyaluronan, are also used in the treatment of periodontal disease, but mainly to promote healing of soft periodontal tissue after surgical treatment of non-inflammatory defects such as gingival recessions (11, 12). However, the efficacy of the mentioned agents and treatment approaches depends on the degree of destruction of the periodontium: the more extensive the destruction, the less likely it is that periodontal tissue will regenerate completely.

Heparan sulfate glycosaminoglycan (HS GAG) is a polysaccharide built from repeating disaccharide units, each of which is composed of uronic acid (iduronic acid, glucuronic acid) and amino sugars (glucosamine, galactosamine). Together with chondroitin sulfate, keratan sulfate and dermatan sulfate, HS GAG belongs to the group of partially saturated GAGs, while the remaining members of the GAG group are fully saturated heparin and unsaturated hyaluronan (13). HS GAG is one of the key components of the ECM and can be present either anchored on its corresponding cell surface receptors such as HS proteoglycans (HSPGs) or as a shedded soluble substance within the ECM (14, 15). Major cell-surface HSPGs that bind HS GAG belong to a four-member family of Syndecans (Sdc1-4) which are expressed in most mammalian tissues (16). Sdcs are type II receptors comprised of a core protein (with cytoplasmic, transmembrane, and ectoplasmic domains) to which several HS GAG linear side chains are covalently attached (17, 18). As a modulator of cell signaling, HS GAG is involved in the regulation of various processes important for tissue development and homeostasis, including proliferation, differentiation, adhesion and migration of cells (13, 15, 17, 19). The role of HS GAG in the above processes depends on the degree of polymerization/fragmentation and structure/saturation of the glycan chain and the way HS GAG molecules are incorporated into the ECM; as free polysaccharide chains or covalently bound in complexes with HSPGs such as Sdcs (19, 20). Accordingly, the structure and the overall expression of HS GAG are tissue specific and subject to dynamic changes during pathological events in the tissue (inflammation, infection, healing, etc.) (20, 21).

As the major ligand of HSPGs, HS GAG interacts with released chemokines, integrins and selectins and participates in the regulation of different aspects of inflammatory response including the formation and breakdown of gradients of inflammatory mediators, as well as the recruitment of leukocytes (rolling, adhesion, and transmigration) from the circulation to the site of infection/injury (15, 22). One of the obstacles in studying the mechanistic effects of altered expression of HS GAG on the course of the inflammatory response has been that no viable HS GAG knockout animals could be generated because HS GAG is essential during organogenesis (23-25). However, it has been possible to generate viable knockout animals for certain cell surface HSPGs (such as Sdc1 and Sdc4), and the response of these animals to noxious stimuli has been studied in detail. Because the presence of cell surface HSPGs strongly influences the bioavailability of HS GAG in tissues and diverse physiological functions of HSPGs are in fact mediated by HS GAG, the reported effects of knockout of individual HSPGs can be attributed in part to altered

expression of HS GAG. For example, studies using Sdc1 knockout mice have demonstrated that the absence of Sdc1 (and therefore disrupted bioavailability of cell surface HS GAG in tissues) exacerbates the inflammatory response and prolongs wound healing (26, 27). There are also findings that argue how Sdc4 plays a role in inhibiting the production of interleukin-1-beta which suggests that Sdc4 may have a protective function (28). Apart from HSPGs, certain enzymes for modifications of HS GAG may also affect the overall expression of HS GAG in tissues. HS GAG can be enzymatically cleaved into shorter fragments by endoglycosidase heparanase 1 (HPSE1). HPSE1 has been reported to exhibit increased expression and enzymatic activity in conditions such as inflammation (29-32). The possible effects of major HS GAG biosynthesis enzymes from the GAGosome complex on the course of inflammation have been studied recently. In contrast to prior examples, mice with conditional NDST1 knockout (and consequently reduced N-sulfation of HS GAG) seem to exhibit mild inflammatory response compared to the wild-type mice (33, 34). This confirms the importance of the site-specific structure and sulfation pattern of HS GAG and its general role as a modulator with both proinflammatory and anti-inflammatory properties. While the association of HS GAG/HSPGs with the propagation of inflammation is well documented, its role in the resolution of inflammation and remodeling of the ECM in terms of restoring normal tissue structure and function must also be mentioned. In general, cleavage of the side chains of HS GAG can facilitate the shedding of HSPG ectodomains. This in turn can have an anti-inflammatory effect due to degradation of the chemokine gradients promoting the resolution of inflammation (15, 35, 36).

HS GAG can effectively bind a wide range of proteins from both host and microbial sources (37). Epithelial cells are often the primary targets of bacterial pathogens during the early stages of infection. The HS GAG chains attached to Sdc1 play a crucial role in infection by facilitating the attachment of bacteria to host cells (38). This is the rationale behind reports that showed how HS GAG deficient cells, as well as Sdc1 knockout mice were less susceptible to various viral and bacterial infections, respectively (15, 39, 40). When bound, bacteria can be internalized within the cell, although not all bacteria utilize this pathway. Studies have shown that some bacteria like *P. aeruginosa* and *S. aureus* induce proteolytic cleavage of the HS GAG side chains on HSPG ectodomains to modulate the host's immune response (41, 42). Thus, by masking their antigens with those of the host's origin, bacterial pathogens can successfully evade the host's immune response (43). By doing so, the pathogens enhance their virulence and the chance of survival within

the challenging host environment (15, 44, 45). It appears that local changes in the expression of HS GAG and HSPGs may also influence the inflammatory response by modulating host susceptibility to microbial infection. In diseases such as periodontitis, bacterial invasion triggers and partially sustains the inflammatory response which is ultimately responsible for periodontal tissue destruction (46). In this context, it may be plausible that depletion of HS GAG content (rather than supplementation of HS GAG) can reverse the destructive course of the disease.

At present, there is a lack of data regarding the effectiveness of HS GAG supplementation in treating severe forms of periodontitis in humans. However, various studies conducted on experimental rodent models of periodontitis have demonstrated that supplementing the ECM with a synthetic derivative of HS GAG called *RGTA*[®] can effectively reduce inflammation in periodontal tissues, facilitate healing, and promote regeneration of both soft and hard tissues, including the alveolar bone (47, 48). *RGTA*[®] is a synthetically derived functional mimetic of HS GAG, which is spontaneously incorporated into defects of the ECM structure, preventing proteolysis and stimulating ECM neosynthesis, resulting in more optimal tissue healing (48, 49). Application of *RGTA*[®] in the regenerative therapy of periodontitis of rodent models displayed that all of its positive effects, such as the reduction of inflammatory cell infiltrates in the gingiva, the reduction of osteoclastic activity and the regeneration of the alveolar bone, are achieved without prior initial periodontal therapy (47-50).

To date, no experimental clinical research aimed at demonstrating similar effects of synthetic derivatives of HS GAG in humans suffering from severe forms of periodontitis has been registered, although the first data on the regenerative potential of ECM supplementation with synthetic derivatives of HS GAG on an experimental basis in a rodent periodontitis model were published two decades ago (47, 49). Assessing the effectiveness of supplementation of HS GAG by its synthetic derivatives in the treatment of periodontitis in humans, either independently or in conjunction with prior surgical or non-surgical treatments, is challenging for several reasons. Firstly, there are general limitations inherent to all periodontitis models in experimental animals; these models cannot fully replicate the complex pathogenetic mechanisms and long-term episodic nature of the disease as observed in humans due to factors such as simplified diet, accelerated disease progression, mono- or bi-microbial inoculation, and genetic variations among animals (48, 51, 52). Secondly, native HS GAG can act as both the inhibitor and promoter of the

inflammatory response and infection, which is influenced by changes in its structure and bioavailability in tissues in homeostasis and disease conditions alike (15). Finally, the presence of conflicting data on the mechanism of action of native HS GAG and synthetic derivatives of HS GAG in bone metabolism, which, according the recent research, point that the former can be attributed with the role of an intermediate promoter of osteoclast formation and bone resorption (53).

The aim of this doctoral dissertation and its pooled articles was to predict the influence of native HS GAG on the formation of inflammatory infiltrate in the gingiva and the resorption of alveolar bone during advanced generalized periodontitis in humans. In order to achieve this aim, it was necessary to improve the existing protocols for quantifying and analyzing immunofluorescence (IF). These improvements aimed to enable the generation of statistical models based on the expression of investigated factors which include HS GAG cell surface receptors, enzymes involved in HS GAG biosynthesis, modification, and degradation as well as HS GAG specific markers along with inflammation and bone resorption involved markers, that are all present in histological gingival tissue sections. Additionally, considering the known role of HS GAG in regulation of the inflammatory response and overall bone metabolism, a statistical model was developed to simulate the effect of modifying HS GAG expression on the formation of an inflammatory infiltrate in the gingiva and the resorption of alveolar bone in individuals with advanced generalized periodontitis.

2.2. MATERIALS AND METHODS OVERVIEW

2.2.1. PARTICIPANTS SCREENING AND RECRUITMENT

Tissue samples of human gingiva were taken from a total of 40 participants who were treated by a periodontist at the *Department of Maxillofacial Surgery of University Hospital of Split* and the *Department of Periodontology of University of Zagreb, School of Dentistry*. Periodontitis was diagnosed by two experienced periodontists who evaluated participant's medical history, as well as clinical and radiographic status of their periodontal tissues. Measurements such as probing depth (PD), gingival recession (RE), clinical attachment level (CAL), full-mouth plaque (FMPS) and bleeding (FMBS) scores were recorded at six different sites per tooth using conventional periodontal probe (PCP 15; Hu-Friedy, Chicago, IL, United States). Severity of periodontitis was determined based on the new classification of periodontal diseases by the 2017 World Workshop on the Classification of Periodontal and Peri-Implant Diseases and Conditions (54).

Participants were divided into a control group (n = 20) and a group with advanced generalized periodontitis (n = 20). The inclusion criteria were age of at least 18 years, good general health (no systemic diseases), healthy periodontal tissue (controls) and generalized periodontitis stage III or IV with at least one tooth indicated for extraction due to poor condition of periodontal tissue (periodontitis group). The exclusion criteria were presence of periodontal abscess and endo-periodontal lesions in the vicinity of the sampling area, systemic conditions affecting periodontal tissue (e.g., diabetes mellitus), long-term medication, medical history of systemic antibiotic therapy within the last 6 months, pregnancy, alcohol, or drug abuse.

2.2.2. TISSUE SAMPLES COLLECTION

Participants from the control group underwent crown lengthening as a part of preparatory phase for prosthetic treatment. The surgical procedure for crown lengthening was conducted under local anesthesia and involved gingivectomy, osteotomy and osteoplasty. The samples of healthy gingiva (average dimensions of 2,5 mm × 1,5 mm) were excised from the buccal aspect of the gingival margin down to the alveolar bone crest, before the osteotomy and osteoplasty procedures

were carried out. Participants from the periodontitis group either underwent crown lengthening or (in preparation for the initial periodontal therapy) tooth extraction using a periosteal elevator (Aesculap AG, Tuttlingen, Germany). During the extraction process the sample of diseased gingiva (average dimensions 4 mm × 2,5 mm) was excised from the gingival margin down to the alveolar bone crest with a type 15C scalpel blade (Aesculap AG, Tuttlingen, Germany) on the buccal aspect of tooth extraction site. The clinical follow-up procedures for participants from both groups adhered to established guidelines for the type of treatment they received.

Prior to any procedure, all the participants were informed about the purpose of this study and clinical procedures related to it. Participants signed an informed consent form for participation in the research along with a consent form for processing of personal data in accordance with the World Medical Association's Declaration of Helsinki (55), the European Union's General Data Protection Regulation (GDPR), and Croatian laws: Health Protection Act, Health Data and Information Act, Patients' Rights Protection Act, and Dentistry Act.

2.2.3. TISSUE SAMPLES PROCESSING

After the samples of gingiva were obtained, vestibular (labial/buccal) surfaces were marked by waterproof color. Then the samples were placed in sealed containers with 4% paraformaldehyde and delivered to the laboratory within the next 24 h for paraffin embedding. The waterproof color marking of vestibular surfaces was used for proper orientation of the samples during the paraffin embedding procedure.

Paraffin blocks containing the samples were later cut into serial 5 µm thick sections and subsequently mounted on glass slides. Slides were stored in the bio-archives of the *Department of Anatomy, Histology and Embryology of University of Split School of Medicine* and designated with unique depersonalized codes representing participants from whom the tissues were sampled.

2.2.4. SAMPLE STAINING

Gingival tissue sections were deparaffinized in xylene and ethanol, rehydrated in distilled water and incubated for 10 min in 0,1% H₂O₂ for suppression of endogenous peroxidase activity. Afterwards, sections were washed in phosphate buffer solution (PBS) and put in sodium citrate buffer and heated for 15 min at 95°C in a microwave oven. Prior the 24 h incubation in the dark chamber with primary antibodies, sections were left to cool down to room temperature (56). Immunohistochemical staining (IHC) was divided into two groups: slides designated for brightfield (BF) microscopy (orientation slides) and those for immunofluorescent (IF) microscopy.

BF slides were stained using hematoxylin and eosin (H&E) in order to verify the preservation of tissue morphology and proper alignment of tissue compartments (gingival epithelium, gingival sulcus epithelium, and subepithelial stroma (every 10th slide in each sample). Additional batch of BF slides was stained with Alcian Blue (AB) staining kit (pH 1, mucin staining) (ab150661; Abcam plc, Cambridge, UK), a polyvalent basic dye that binds to highly sulfated mucosubstances (including GAGs).

IF slides were stained using primary and secondary antibodies displayed in Table 1 following the standardized protocol of the laboratory of the *Department of Anatomy, Histology and Embryology of University of Split School of Medicine*. Before the application of primary antibodies, all slides were incubated in protein block (ab64226; Abcam plc, Cambridge, UK) for 30 min at room temperature. According to manufacturer's instructions, slides designated for staining with anti-HS3G10 primary antibody (ab150105; Abcam plc, Cambridge, UK) had to be additionally treated with the enzyme Heparinase III (0,02 IU/50 µL) at 37°C for 2h prior the application of the primary antibody. To stain cell nuclei, sections were shortly incubated with 4'6'-diamidino-2-phenylindole (DAPI).

Table 1. *Primary and secondary antibodies used for IF staining of the samples.*

Primary antibody ○ Secondary antibody	Dilution	Manufacturer
• Mouse monoclonal Anti-Sdc1 (ab34164) ○ Donkey polyclonal Anti-mouse Alexa Fluor 594 (ab150108)	1:100	Abcam plc, Cambridge, UK
• Rabbit polyclonal Anti-Sdc2 (ab191062) ○ Goat polyclonal Anti-rabbit Alexa Fluor 488 (ab150077)	1:200	Abcam plc, Cambridge, UK
• Rabbit polyclonal Anti-Sdc4 (ab24511) ○ Goat polyclonal Anti-rabbit Alexa Fluor 488 (ab150077)	1:100	Abcam plc, Cambridge, UK
• Rabbit polyclonal anti-EXT1 (ab126305) ○ Goat polyclonal Anti-rabbit Alexa Fluor 488 (ab150077)	1:100	Abcam plc, Cambridge, UK
• Rabbit polyclonal anti-EXT2 (ab102843) ○ Goat polyclonal Anti-rabbit Alexa Fluor 488 (ab150077)	1:50	Abcam plc, Cambridge, UK
• Rabbit polyclonal anti-NDST1 (ab129248) ○ Goat polyclonal Anti-rabbit Alexa Fluor 488 (ab150077)	1:50	Abcam plc, Cambridge, UK
• Rabbit polyclonal Anti-NDST2 (ab151141) ○ Goat polyclonal Anti-rabbit Alexa Fluor 488 (ab150077)	1:100	Abcam plc, Cambridge, UK
• Mouse monoclonal anti-HS3G10 (370260-1) ○ Donkey polyclonal Anti-mouse Alexa Fluor 488 (ab150105)	1:100	Seikagaku corp, Tokyo, Japan Abcam plc, Cambridge, UK
• Mouse monoclonal anti-HS10E4 (370255-1) ○ Donkey polyclonal Anti-mouse Alexa Fluor 488 (ab150105)	1:100	Seikagaku corp, Tokyo, Japan Abcam plc, Cambridge, UK
• Rabbit polyclonal Anti-HPSE1 (ab85543) ○ Goat polyclonal Anti-rabbit Alexa Fluor 488 (ab150077)	1:200	Abcam plc, Cambridge, UK
• Rabbit polyclonal Anti-SULF1 (ab32763) ○ Goat polyclonal Anti-rabbit Alexa Fluor 488 (ab150077)	1:200	Abcam plc, Cambridge, UK
• Mouse monoclonal [2B4] Anti-SULF2 (ab113405) ○ Donkey polyclonal Anti-mouse Alexa Fluor 488 (ab150105)	1:25	Abcam plc, Cambridge, UK
• Rabbit polyclonal Anti-SLC26A2 (ab238591) ○ Goat polyclonal Anti-rabbit Alexa Fluor 488 (ab150077)	1:200	Abcam plc, Cambridge, UK
• Rabbit polyclonal Anti-CD44 (ab157107) ○ Goat polyclonal Anti-rabbit Alexa Fluor 488 (ab150077)	1:500	Abcam plc, Cambridge, UK
• Mouse monoclonal Anti-CD45 (ab8216) ○ Donkey polyclonal Anti-mouse Alexa Fluor 488 (ab150105)	1:200	Abcam plc, Cambridge, UK
• Rabbit polyclonal anti-RANKL (LS-B1425-0.05) ○ Goat polyclonal Anti-rabbit Alexa Fluor 488 (ab150077)	1:200	LSBio inc, Seattle, USA Abcam plc, Cambridge, UK
• Rabbit polyclonal Anti-OPG (ab73400) ○ Goat polyclonal Anti-rabbit Alexa Fluor 488 (ab150077)	1:500	Abcam plc, Cambridge, UK

2.2.5. IMAGE ACQUISITION AND PROCESSING

H&E stained slides were examined under Olympus BX40 light microscope (Olympus, Tokyo, Japan) equipped with a manual slide scanner (Microvisioner, Esslingen am Neckar, Germany), standard (Olympus DP27, Olympus, Japan) and area-scan high-resolution camera (Basler aceA2500-14gm, Basler, Germany). H&E panoramic images were captured at objective lens magnification $\times 20$ with exposure time set to 8 ms and ISO to 100. They were exported as

JPEG files and post processed in Adobe Photoshop® 2014 (Adobe, San Jose, CA, USA). Post processing consisted of rotation and alignment which was done using action presets customized for every sample individually (40 in total) because of sample size and shape variation. The presets contained 4 basic operations for orientational alignment (“Transform”, “Rotate”, “Crop” and “Merge”). Overall size of these images (600 MB on average) was reduced by converting them from TIFF to JPEG format on a high-resolution background (600 dpi) regarding minimalization of image detail loss and preservation of data storage space since these images were only used for preliminary histomorphometry.

IF stained slides were examined in the microscopy laboratory of *Mediterranean Institute for Life Sciences* using Zeiss Axio Observer (Carl Zeiss Microscopy GmbH, Jena, Germany) equipped with Zeiss AxioCam 506 color camera (Carl Zeiss Microscopy GmbH, Jena, Germany). IF images were captured at objective lens magnification $\times 10$ at full frame resolution (2752×2208 px) in original black and white 8-bit depth (256 px grey values (GV)) pseudo-colorizer mode using multichannel and panorama modules in ZEN 2.5 software (Carl Zeiss Microscopy GmbH; Jena, Germany). After background calibration (0 px GV), exposure time in multichannel module was set at 35 ms for DAPI, 800 ms for green (AF488) and 12000 ms for red (AF594) fluorescence while keeping camera sensitivity at the lowest ISO (ISO = 100). This way IF images were rendered to display full dynamic range of px GV on a scale from 0 (pure black) to 255 (pure white). Depending on the fluorescence channel (color), this also allowed a 2- to 5-fold reduction of the overall exposure time for image acquisition and significantly reduced the risk of photo-bleaching of IF signals. Panorama module facilitated manual navigation through tile images along x/y axes guided by the on-screen live view of DAPI channel with minimal 20% overlap (x axis) and 10% maximal shift (y axis) between individual tiles. A built-in stitching tool was used to merge individual tiles into a complete panoramic image of a gingival tissue section from the slide. Panoramic IF images were closely inspected for quality (tiles alignment, absence of stitching artifacts) and stored in raw format (CZI – Zeiss proprietary file format) containing original data and metadata. Each file was then exported in multiple TIFF format files (original black & white 8-bit, pseudo-colored 8-bit and merged 16-bit).

The original black & white 8-bit panoramic IF images alone were post-processed and utilized for further analysis. Specifically, the pseudo-colorization tends to decrease the overall dynamic

range of IF signals. This reduction in dynamic range results in less precise adjustment of the cut-off signal threshold, which is crucial for distinguishing true IF signals from autofluorescence, making the quantification of IF signals less accurate. The reason for the reduction in dynamic range lies in the fact that all software used for image editing or analysis interprets colors as varying shades of grey, automatically converting color images into black & white. It should be noted that different software and image modes can impact the measurement of signal intensity (57).

For H&E images, epithelial tissue compartment (gingival epithelium, gingival sulcus epithelium) and stromal tissue compartment were masked using graphic pen tablet (Wacom Intuos PRO, Wacom Co., Saitama, Japan). Whole section area and areas of specific tissue compartments (epithelia, subepithelial stroma) were measured in Adobe Photoshop® 2014 (Adobe, San Jose, CA, USA) using Magic Wand selection and histogram tool. Values were expressed as absolute values in px (number of px) (whole-section area), and as relative values (proportion of the whole-section area) expressed in percentages (areas of tissue compartments).

The post-processing of panoramic IF images was carried out using Adobe Photoshop® 2014 and 2020 (Adobe, San Jose, CA, USA). All images were thresholded to a px GV of 10 using “threshold” tool. The authors have agreed that IF signals lower than px GV = 10 were considered autofluorescence and were excluded from the image. Panoramic IF images orientational alignment was conducted like the approach employed for panoramic H&E images using action presets customized for each sample. The accuracy of alignment was verified by comparison of the merged panoramic IF images of different channels (primary antibody staining vs. DAPI staining) before and after the alignment. As the panoramic IF images were captured at objective lens magnification $\times 10$ with full-frame resolution, consisting of fewer individual images, there was no significant requirement for size reduction compared to panoramic H&E images.

To generate panoramic images encompassing the entire section area, the IF signal and corresponding DAPI panoramic IF images were merged using the "Lighten" blending mode. A threshold value of px GV = 1 was applied, and the border at the interface between the background was traced using the "Brush" tool to enable the selection of the entire section with the "Magic Wand" tool. Blending masks for tissue compartments (epithelial/stromal) were created in a similar manner by tracing the interface between the epithelial and stromal tissues. Consequently, for each pair of IF signal and DAPI panoramic images, an additional nine panoramic images were generated,

including epithelial and stromal IF signal images, epithelial and stromal DAPI images, binary 8-bit images of the entire section area, as well as two blending masks representing the epithelial and stromal compartments. The image editing workflow is displayed in Figure 1.

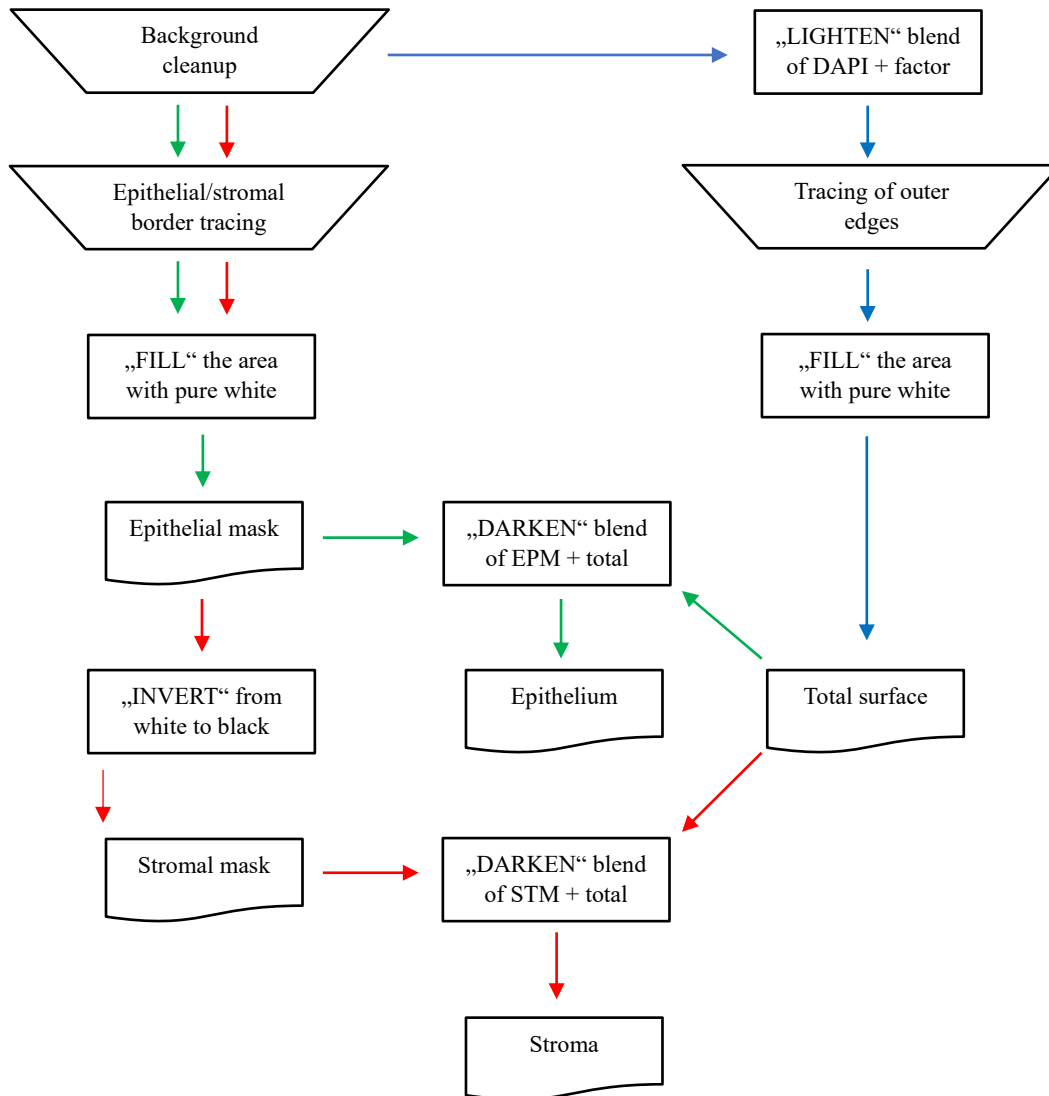


Figure 1. Flowchart displaying the image editing workflow.

2.2.6. SIGNAL QUANTIFICATION AND IMAGE ANALYSIS

IF signal quantification was done by means of histograms and 2D plot profiles generated using ImageJ (National Institutes of Health, Bethesda, MD, USA). Histograms are tables with listed x-values (IF signal intensity ranging from px GV 0 to 255) and their corresponding y-values (number of px with corresponding GV). These tables were utilized to determine the size of expression domains (are of the sample covered by IF signal), both as cumulative and fractional values expressed in percentages, for individual samples and as mean values for group of samples. Quantification of IF signals by histograms is based on the number of px per unit of intensity (px GV).

2D plot profiles of panoramic IF images in a top-down (T-D) vertical (marginal-apical) direction. They were calibrated to fit the μm scale (at objective lens magnification $\times 10$, 1 px equals $0,53937 \mu\text{m}$). 2D plot profiles calculate and list the average px GVs row sections of the panoramic IF image sized 1 px x number of px corresponding to the width of the panoramic IF image. Thus, in contrast to histograms, this means that the total number of output values depends on image dimensions. For the panoramic IF images of gingival samples taken at objective lens magnification $\times 10$, 2D plot profile output ranges between 5000 and 12000 values. Quantification of IF signals by 2D plots is based on the mean intensity (px GV) of IF signal per unit of space. Therefore, by quantifying and plotting the spatial gradients, 2D plot profiles are suitable for in silico colocalization of multiple IF signals from serial sections and subsequent correlation analysis and statistical modeling.

The generated data sets for both histogram and 2D plot profiles were exported to Microsoft Office Excel 2016 (Microsoft Corp., Redmond, WA, USA) spreadsheets and used for further statistical analysis.

2.2.7. STATISTICAL ANALYSIS AND MODELING

To ensure meaningful comparisons between samples of different shapes, histomorphometric analysis was conducted first. Gingival samples consist of two tissue compartments: epithelial and

stromal. Given the different shape and size of each tissue section, the sizes of the compartments were calculated as proportions (percentages) of the total sample size. Descriptive statistics and t-tests were employed to analyze histomorphometric parameters of gingiva samples, including the whole section area, fraction areas of tissue compartments, and cellularity. For the basic histomorphometric profiling, the significance level was set at $\alpha = 0,1$ ($P < 0,1$) since these parameters were calculated as single values per tissue section.

Only T-D plots of panoramic images of gingival sections from the periodontitis group were used for statistical modeling. By aggregating T-D plots for each marker and calculating moving averages (1000 data points interval), spatial gradients were ultimately presented with 7000 data points. These compressed datasets were more manageable for the subsequent statistical modeling. Next, the compressed T-D plots were integrated into a set of regression equations known as first level models containing a pair of variables (one predictor and one outcome). Determination of variable pairs was done according to reconstruction of investigated factors reactome using STRING database (58). These models were created using spline regression where each 7000 line dataset representing the spatial gradient of individual marker was split into segments by manual positioning of the knots. Each segment was modeled individually either by simple linear regression function or polynomial nonlinear regression function (2nd and 3rd order) to enable tight fit between the pair of variables of no less than $R^2 = 0,99$. An additional set of guidelines was also considered for modeling segments in first level models: (i) known effect of the predictor on the outcome variable based on experimental data from the relevant literature dictating the type of correlation between the two (positive/negative correlation, linear/non-linear); (ii) known effect of the predictor on the outcome variable based on comparison of spatial gradients measured in controls and samples from periodontitis group; (iii) the value of y-axis intercept should fall within the range of 0-100 since the data in T-D plots are expressed as percentages of maximal px GV; (iv) for very short segments up to 4 data points, linear fitting is preferred to non-linear fitting if the y-axis intercept condition is met; (v) the functions included in SplR must reflect the effect of peak or floor plateaus since the model variables represent ECM components and factors associated with ECM components whose interactions are determined by feedback loops with the effect of peak or floor plateaus; (vi) when two functions were of the (nearly) same fit, those that described the relationship between the pairs more truthfully (according to *STRING* and existing literature) were preferred while aligning with the general tendency to opt for simpler functions when possible.

When the regression functions for second level models were calculated, variable pairs were rearranged into another set of matrices representing the third level models. Thus, the entire functional network of investigated factors reconstructed from *STRING* reactome could be translated into regression equation system. This was done by two means; examination of existing research, conducted on cell cultures and animal models, describing relationships and dependencies between factors of interest and consulting the *STRING* reactome database (58). Factors were grouped by the similarity/synergy of their functions and the relationships between individual pairs of factors or groups of factors were modeled by spline regression (SplR) and multiple linear regression (MLR). This system of regression equations was divided into 4 modules considering the effect of the studied factors according to the principle of feedback loops and the existence of functional links within the groups. Each module had one variable as the main outcome and this variable served as a link (main predictor) for the next module until all modules were closed in a loop.

Predictions from the original regression equations were calculated for each outcome variable. To generate these predictions, the mean spatial gradient value of the predictor was systematically adjusted in 60 increments, ranging from 0 (virtual knockout) to a 4-fold overexpression relative to the baseline observed in diseased gingiva. The predictors were documented as both the mean spatial gradient of the outcome variable and the deviation from the baseline's mean spatial gradient value in diseased gingiva (expressed as a percentage change). To facilitate this process, an additional set of matrices was generated. These matrices were then employed to calculate supplementary regression functions (second level models), which were subsequently integrated into the overall system of regression equations (third level models). This comprehensive model enabled the prediction of expression profiles for the studied factors.

According to American Statistical Association's Statement on Statistical Significance and *P*-values, *P*-values for regression tests were presented as calculated and should be interpreted accordingly (59). Statistical analysis was performed in Microsoft Office Excel 2016 (Microsoft Corporation, Redmond, WA, USA).

2.3. RESULTS OVERVIEW

The demographic and clinical parameters of the participants are shown in Table 2. On average, participants from the periodontitis group were older than the control group. Most of the participants from the periodontitis group were smokers, whereas there were no smokers in the control group. Statistically significant differences between the control and periodontitis groups were found in FMPS (Full Mouth Bleeding Score), PD (Probing Depth), and CAL (Clinical Attachment Level). There was no statistically significant difference in the proportion of female and male participants in either group.

Table 2. Demographic and clinical parameters of the participants.

	Controls (n = 20)	Periodontitis (n = 20)	P-values
Age (years)	38,9 ± 9,23	50,26 ± 10,6	0,007 ^t
Sex (F / M)	8 F/12 M	9 F/11 M	1,000 ^{chi}
Smokers	0	17	< 0,001 ^{chi}
FMPS (%)	21,95 ± 8,95	36,17 ± 15,76	0,001 ^t
FMBS (%)	8,95 ± 3,73	43 ± 11,27	< 0,001 ^t
PD (mm)	1,47 ± 0,22	4,53 ± 1,19	< 0,001 ^t
CAL (mm)	1,52 ± 0,22	6,1 ± 1,43	< 0,001 ^t

^t – *t*-test used, ^{chi} – Chi squared test used, FMPS – Full Mouth Plaque Score; FMBS – Full mouth bleeding score; PD – Probing depth; CAL – Clinical attachment level.

2.3.1. FIRST ARTICLE

The aim of the first article was to compare the differences in expression of factors functionally related to HS GAG between healthy gingiva and gingiva of patients with advanced generalized periodontitis (60). This includes markers specific to HS GAG cell receptors from the syndecan group (Sdc1, Sdc2, and Sdc4), HS GAG synthesis/polymerization enzymes (EXT1 and EXT2), as well as enzymes involved in initial modification (deacetylation and sulfation – NDST1 and NDST2) and degradation (HPSE1) of HS GAG chains. The expression of the investigated

markers in specific regions of gingiva and the distribution of intensity of their expression on a whole tissue-section level are visible on Figure 2 and Figure 3, respectively. Additionally, general inflammatory cell marker CD45 marked the presence of leukocytes in the gingiva as this was necessary to evaluate the amount of inflammatory infiltrate. Initially, a comparison of group means was conducted to assess the total expression domains of all the investigated factors at a significance level of $\alpha = 0,01$. This analysis revealed that only EXT1 exhibited differential regulation in periodontitis ($P < 0,0001$). Furthermore, a comparison of group means for the expression domains within the epithelial and stromal compartments was performed. While no significant differences were observed in the epithelial expression domains of the investigated factors between the control and periodontitis groups, they were found in the stromal expression domains for Sdc1 ($P < 0,0001$), EXT1 ($P < 0,0001$), NDST1 ($P = 0,0001$), HPSE1 ($P = 0,0023$) and CD45 ($P = 0,0037$) between the control and periodontitis groups. A graphic display of comparison of mean group values of expression domains and epithelial and stromal expression domain ratios of investigated factors in both groups is visible in Figure 4. Based on the observed expression patterns, it appears that the investigated factors may play a role in regulation of the inflammatory response in gingiva affected with advanced generalized periodontitis. Given that these factors are primarily involved in the biosynthesis, modifications, and degradation of HS GAG, the findings also point to potential alterations in the quantity and structure of HS GAG in the gingiva of patients with advanced generalized periodontitis compared to healthy gingiva.

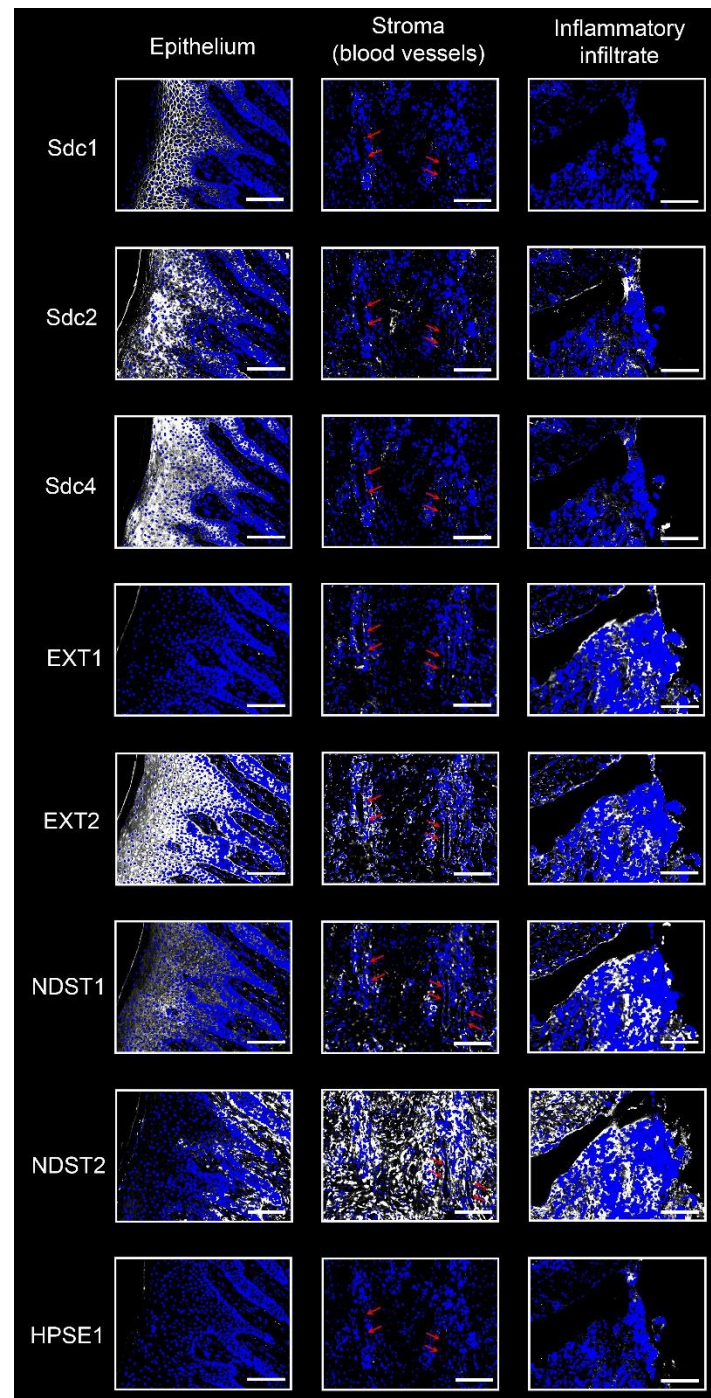


Figure 2. Expression of Sdcs, EXTs, NDSTs and HPSE1 in different regions of gingiva from a subject with advanced periodontitis (sample: DK-SL17-CHP) (IF signals – white; DAPI nuclear staining – blue). Enlarged portions of the section are shown emphasizing how Sdcs, EXTs, NDSTs and HPSE1 are expressed in various regions of the diseased gingiva. Red arrows are pointing at blood vessels. Objective lens magnification $\times 20$; scale bar: 50 μm .

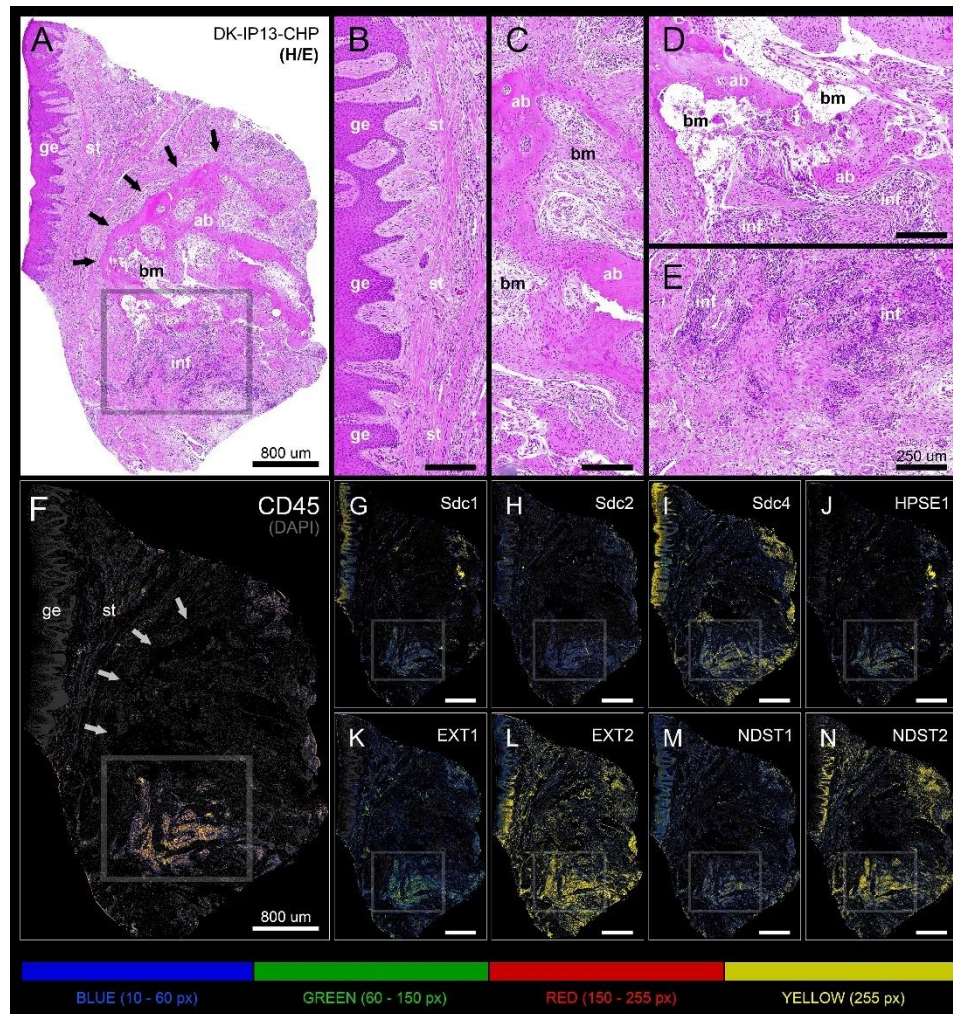


Figure 3. Panoramic H/E image (A) and panoramic multi-color heatmaps (F-N) of diseased gingiva (sample: DK-IP13-CHP) of expression domains of Sdcs (G-I), HPSE1 (J), EXTs (K, L), NDSTs (M, N) and inflammatory marker CD45 (F) merged with DAPI nuclear staining (dark gray). Inflammatory infiltrate degrading alveolar bone is visible (framed areas) (D, E). Subepithelial stroma between the gingival epithelium and intact lamellae of alveolar bone is mostly devoid of inflammatory infiltrate (B). Bone marrow contains portions of fibrotic tissue (C). All investigated factors are expressed in the area of inflammatory infiltrate (G-N) with variable intensity. Objective lens magnification: (A-N) $\times 10$; scale bars – (A, F-N) 800 μm ; (B-E) 250 μm . Designations: gingival epithelium (ge), subepithelial stroma (st), alveolar bone (ab), bone marrow (bm), inflammatory infiltrate (inf). Interface of subepithelial stroma and alveolar bone (black and white thick arrows). Intensity range increments: BLUE (10-60 px), GREEN (60-150 px), RED (150-255 px), YELLOW (255 px).

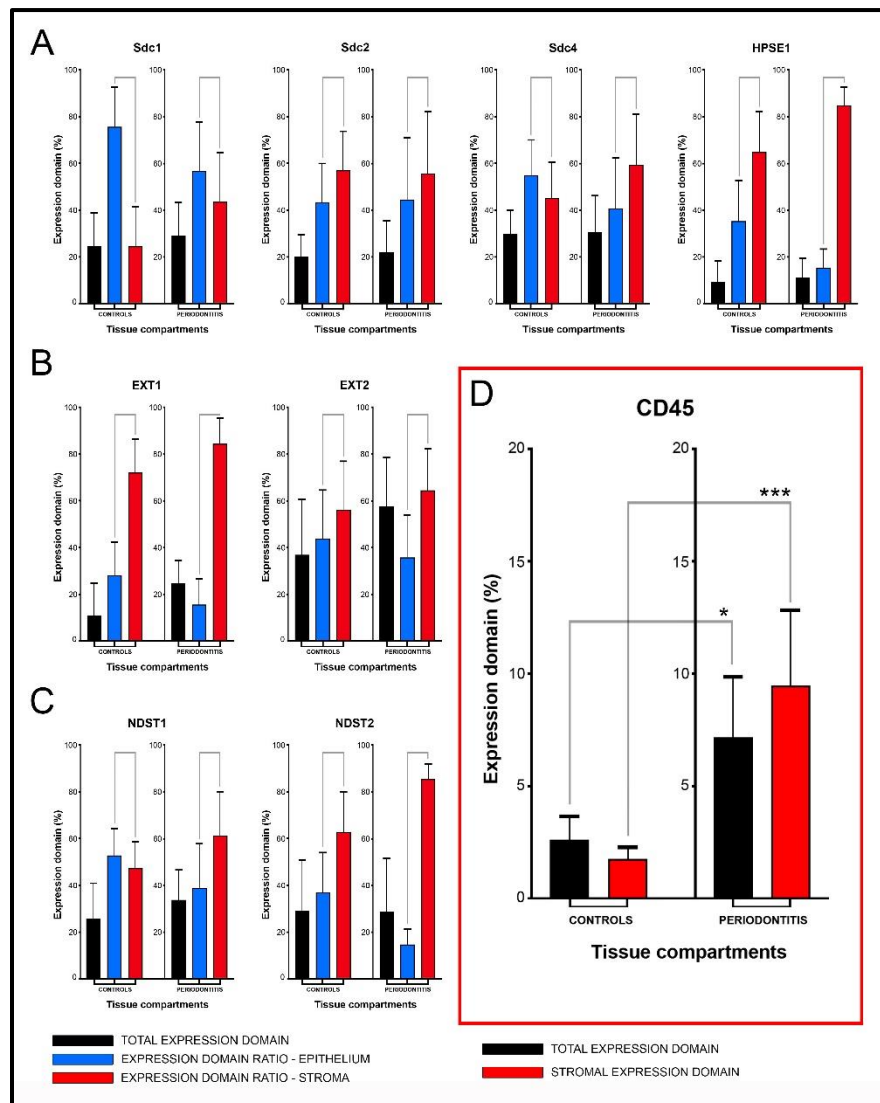


Figure 4. Mean group values of total expression domains (expressed in percentages as fractions of total section area) compared with epithelial and stromal expression domain ratios (expressed in percentages fractions of total expression domain) of investigated factors in control and periodontitis group (A-C). The total availability of Sdcs and HPSE1 seems to be on comparable levels in controls and periodontitis, but their distribution (apart from Sdc2) in epithelial and stromal compartments of gingival tissue differs between two groups (A). EXTs and NDST1 display similar pattern of changes in epithelial/stromal expression domain ratios in favor of stromal compartment (B, C), which corresponds with increased presence of inflammatory infiltrate in periodontitis group (** $p = 0,003747$) (D). Level of significance was set at $\alpha = 0,01$ (** $p < 0,01$; *border values $\alpha = 0,05$).

2.3.2. SECOND ARTICLE

Confirming the presence or absence of expression of a specific factor in a histological tissue section is only the entry point in understanding the factor's involvement in the cellular and/or tissue processes. To accurately compare the overall expression differences of factors functionally associated with HS GAG between healthy and diseased gingiva, as well as the influence of HS GAG and HS GAG related factors on the course of inflammation in gingiva of patients with advanced generalized periodontitis, a new protocol for quantification and co-localization of IF signals from multiple markers had to be designed (57). As the expression of the investigated factors in gingiva is ubiquitous, IF signals from the corresponding markers had to be acquired on panoramic images and quantified from the entire area of histological sections. In contrast to this, conventional protocols for quantification of IF signals are based on the pre-selection of smaller segments of the histological sections known as regions of interest (ROIs). In some cases, ROIs are subjectively picked by researchers which can introduce inaccuracy and bias into the analysis of findings.

Quantification of two basic properties of IF signals was described. The first property is the expression domain (area of tissue/tissue section covered by the IF signal), which is quantified by histograms – representations of the area of IF signal per unit of IF signal intensity. Graphical display of expression domains and field of view proportions is displayed in Figure 5. The second property relates to the spatial gradient (distribution of the IF signal of different intensities within the tissue/tissue compartment) quantified by 2D plot profiles – representations of the IF signal intensity value per unit of area. 2D plot profiles are superior to histograms since the data from 2D plot profiles is suitable for *in silico* colocalization of multiple markers' spatial gradients as shown in Figure 6. By employing 2D plot profiles on panoramic images of serial histological sections stained with distinct primary antibodies, it is possible to colocalize up to 30 different markers/factors. The number of colocalized markers depends on the similarity of shape (compatibility) of serial histological sections as presented in Table 3. This approach to quantification and colocalization of IF signals from multiple markers offers an additional advantage. Namely, this type of data can be used for statistical modeling of the effects of changes in expression of one or several factors on the expression of factor/factors of interest.

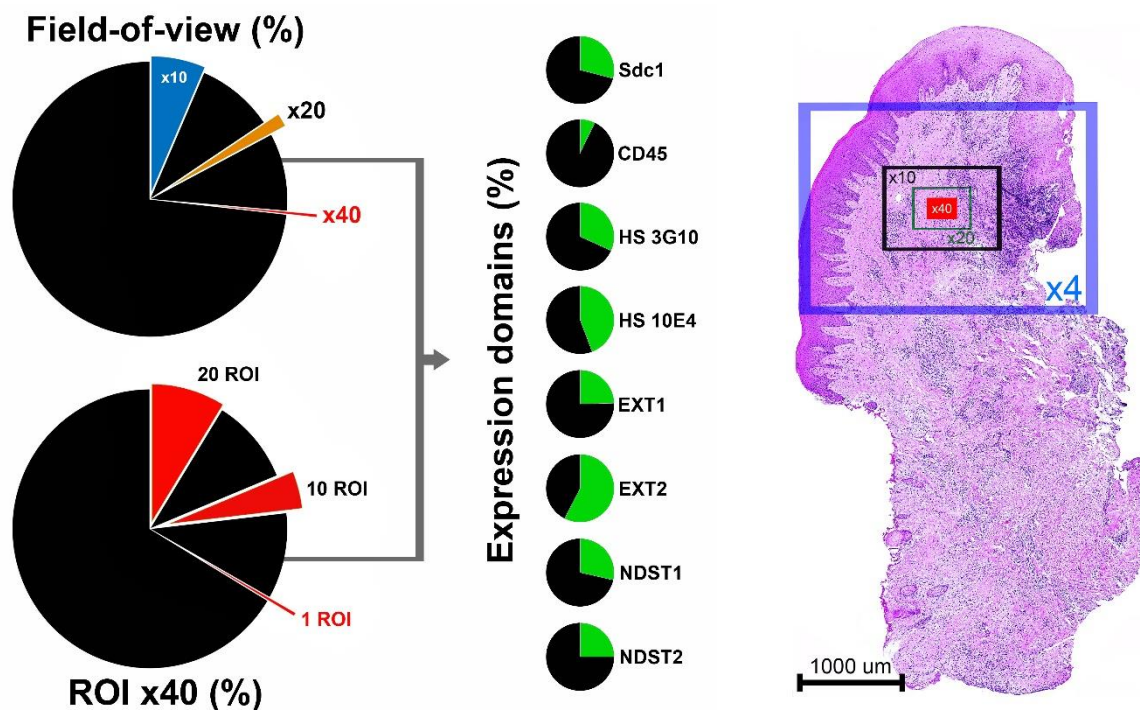


Figure 5. Left: Pie chart comparison of expression domains of investigated factors with field-of-view (objective lens magnifications $\times 10$, $\times 20$ and $\times 40$) and ROIs ($\times 40$) expressed as fraction areas (%) from the whole-section area of samples of human gingiva. Whole-section areas absent of IF signals, outside of field-of-view or excluded from ROIs are presented in black color. The expression domains are presented as cumulatively which does not account for the actual spatial distribution of IF signals. Right: Histological sections of human gingiva analyzed here are relatively small (between 9 mm^2 and 12 mm^2) – a single ROI at objective lens magnification $\times 40$, covers only 0,44% of the whole-section area, meaning that selection of any number of ROIs cannot cover the entire expression domain of investigated factors. Practical comparison of 4 field of views of different objective lens magnifications (from $\times 4$ to $\times 40$) on the same section (sample: DK-JN19-CHP), scale bar: $1000 \mu\text{m}$.

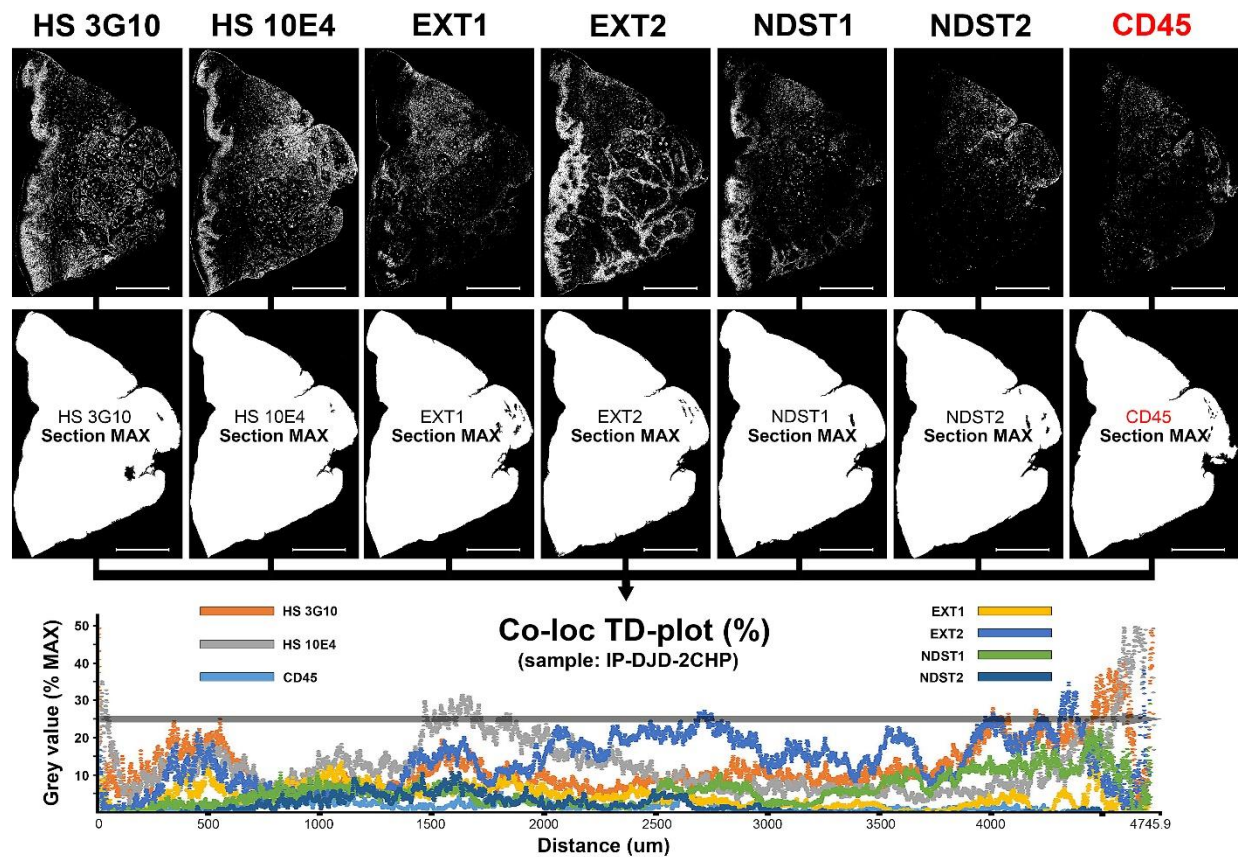


Figure 6. 2D plot profiling for quantification and correlation of spatial gradients of IF signals from primary antibodies against HS GAG, HS GAG biosynthesis enzymes and common leukocyte antigen (CD45) in histological sections of gingiva from patient with advanced generalized periodontitis (sample: IP-DJD-2CHP). (Objective lens magnification: $\times 10$; scale bar: 1000 μm). Spatial gradients of IF signals are plotted simultaneously on a single T-D plot.

Table 3. *Compatibility of serial sections for in silico colocalization and regression analysis of multiple IF signals based on correlation of spatial gradients of DAPI staining in whole-section panoramic images (sample: IP-DJD-2CHP).*

Simple linear regression – DAPI staining T-D plots							
Sections Sequence*	R²	Std. Error[†]	Coefficient	CI[‡]		Significance[§]	
				Lower	Upper	F value	P
REF (x)/(y)	1	$1,9553 \times 10^{-14}$	1	1	1	$2,6303 \times 10^{34}$	0
5th (x)	0,9989	1,0879	1,0022	1,0007	1,0038	$8,4859 \times 10^6$	0
10th (x)	0,9980	1,4998	1,0082	1,0062	1,0103	$4,4611 \times 10^6$	0
15th (x)	0,9943	2,5441	0,9883	0,9848	0,9919	$1,5447 \times 10^6$	0
20th (x)	0,9940	2,6178	1,0091	1,0053	1,0127	$1,4584 \times 10^6$	0
25th (x)	0,9846	4,1924	1,0086	1,0027	1,0146	$5,6328 \times 10^5$	0
30th (x)	0,9814	4,6084	1,0317	1,0251	1,0384	$4,6466 \times 10^5$	0

*Serial number of histological sections stained with DAPI — the first section was used as reference (REF) (dependent variable — y) for autocorrelation (reference model); DAPI staining of every fifth consecutive section up to 30th section (independent variables — x) was correlated with the DAPI staining of the referent section.

[†]Standard error and coefficients (slopes) are expressed in px GVs.

[‡]Confidence interval for coefficients is set at 99%.

[§]Statistical significance is set at $\alpha = 1 \times 10^{-8}$ ($P < 1 \times 10^{-8}$).

2.3.3. THIRD ARTICLE

In the third article, statistical model predictions were presented to evaluate the effects of changes in the expression and structure of HS GAG on the formation of inflammatory infiltrate in the gingiva and the resorption of alveolar bone in patients with advanced generalized periodontitis (61). One of the assumptions, based on the findings from the first article, suggests a difference in the amount and structure of HS GAG in healthy gingiva and gingiva of patients with advanced generalized periodontitis. The expression of HS GAG in gingiva was visualized by two markers that selectively bind to sulfated (HS10E4) and non-sulfated (HS3G10) HS GAG regions. The

expression of these and other investigated factors are displayed in Figure 7 and Figure 8, while their interaction according to STRING reactome database is displayed in Figure 9.

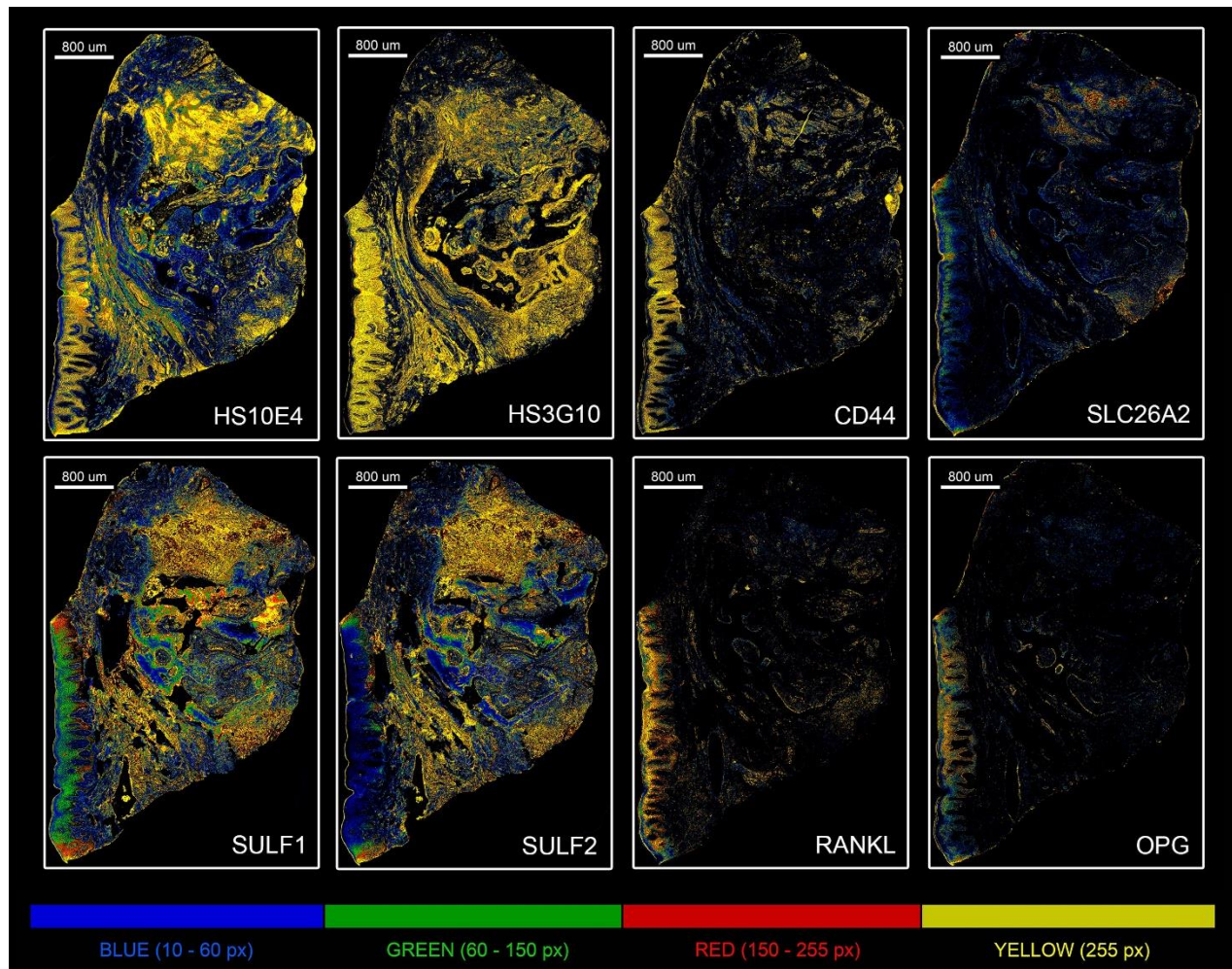


Figure 7. Panoramic multi-color heatmaps of diseased gingiva (sample: DK-IP13-CHP) of expression domains of *HS10E4*, *HS3G10*, *CD44*, *SLC26A2*, *SULF1*, *SULF2*, *RANKL* and *OPG*. Objective lens magnification: $\times 10$; scale bars – 800 μm . Intensity range increments: BLUE (10-60 px), GREEN (60-150 px), RED (150-255 px), YELLOW (255 px).

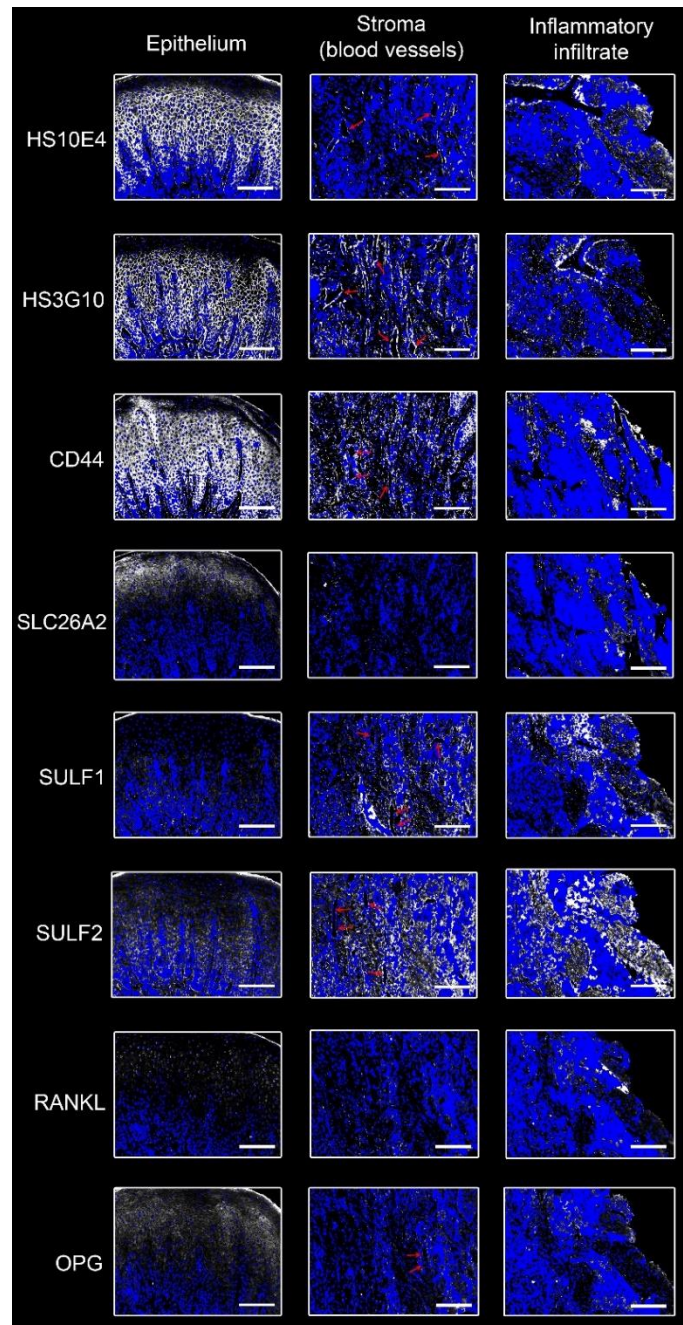


Figure 8. Expression of HS GAG (HS10E4 and HS3G10 markers), sulfatases (SULF1, 2), CD44, ion channel SLC26A2 and bone resorption markers (RANKL and OPG) in different regions of gingiva from a subject with advanced periodontitis (sample: DK-SL17-CHP) (IF signals – white; DAPI nuclear staining – blue).. Enlarged portions of the section are shown emphasizing how the examined markers are expressed in different tissue sections of the gingiva. Red arrows are pointing at blood vessels. Objective lens magnification $\times 20$; scale bar: 50 μm .

As expected, in healthy gingiva there was a significant presence of highly sulfated mucosubstances in the subepithelial stroma, whereas the subepithelial stroma of gingiva from patients with periodontitis displays a lesser abundance of these substances. Both healthy and diseased gingiva exhibit a high expression of HS GAGs in the epithelial compartment (as indicated by the staining with HS10E4 and HS3G10). However, the presence of HS GAG in the non-infiltrated subepithelial stroma is sparse. By comparing the average spatial gradients of HS GAG in healthy and diseased gingiva, distinct expression patterns are observed between the two; the diseased gingiva exhibits a slightly lower quantity of less sulfated HS GAG, a significantly higher RANKL/OPG (TNFSF11/TNFRSF11B) ratio, and the presence of inflammatory infiltrate (CD45). These findings are presented in Figure 10.

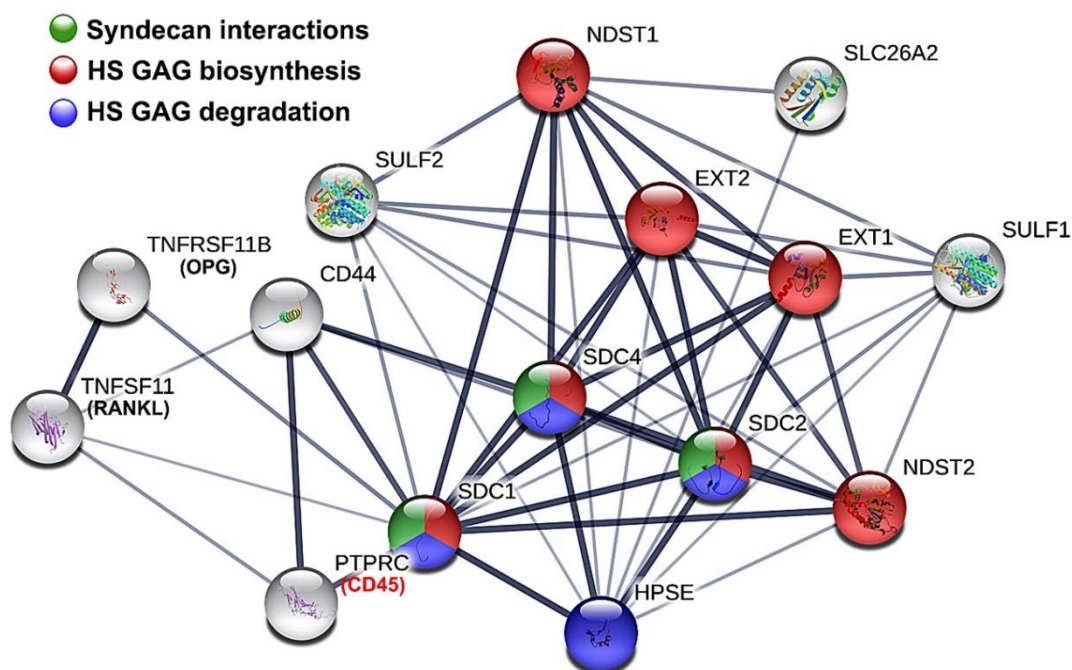


Figure 9. Functional protein network and enrichment from the STRING Reactome database. Network nodes represent the first shell and only 5 proteins from the second shell of interactors. Edges indicate confidence in functional and physical protein association. Colored nodes represent significantly enriched reactome pathways HSA-2022928 (HS GAG biosynthesis), HSA-2024096 (HS GAG degradation) and HSA-3000170 (Sdc interactions).

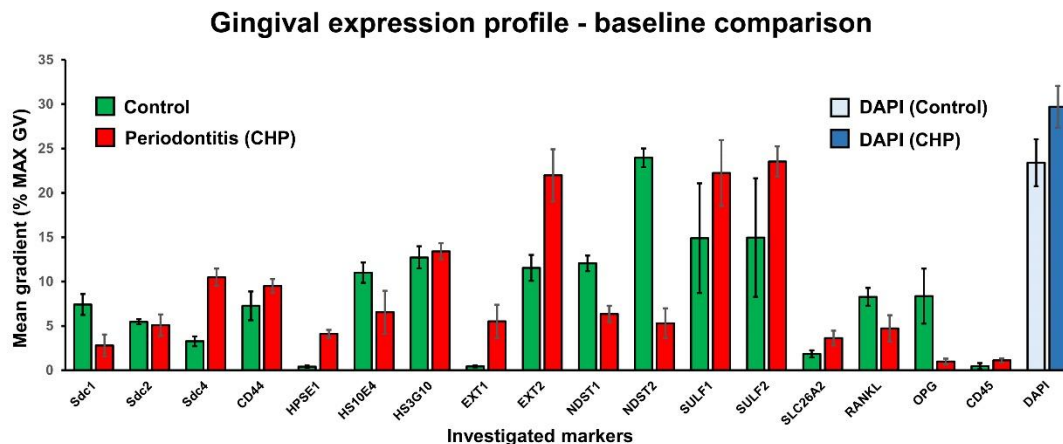


Figure 10. Bar chart comparison of the expression profiles of the investigated markers in healthy (control) and diseased (severe periodontitis) gingiva samples. The expression of each marker is shown as the mean spatial gradient with standard deviation. The mean spatial gradients of DAPI staining are shown as reference values.

The overall statistical model consisted of four interconnected modules. In module 1, the effects of HPSE1 and Sdcs on the expression of cell surface and ECM-located HS GAG were modeled based on the assumption that the increase in the expression of HPSE1 correlates negatively with the expression of Sdcs and HS GAG (62-64). In module 2, the feedback loop between HS GAG and HS GAG biosynthesis enzymes from the GAGosome complex (EXTs, NDSTs) was modeled. The models from module 2 were based on the assumptions that: (i) the expression of HS GAG affects the composition of GAGosome regarding relative expressions of EXTs and NDSTs, and that (ii) the quadruple knockout of EXTs and NDSTs attenuates synthesis of HS GAG (39, 65-67). In module 3, the effects of changing expressions of several enzymes (SULF1, 2) and ion channel (SLC26A2) on variation in the sulfation of HS GAG were modeled. The models from module 3 were based on the assumptions that the increased expression of SULF1, 2 correlates negatively with the overall sulfation/saturation level of HS GAG, while the increased expression of SLC26A2 has the opposite effect (68-71). In module 4, the effects of expression of HS GAG on the formation of inflammatory infiltrate and alveolar bone resorption were modeled. The models from module 4 were based on the following assumptions: (i) the increased expression of HS GAG and Sdc1 correlates negatively with the presence of inflammatory infiltrate and the

same time (ii) promotes the alveolar bone resorption since HS GAG and Sdc1 block OPG (as a decoy receptor for RANKL) shifting RANK/OPG ratio in favor of RANKL (53, 72-76).

According to the overall statistical model predictions, a decrease in the presence of native HS GAG (ranging from the level measured in diseased gingiva to no expression) could lead to further expansion of inflammatory cell infiltrate. However, it would also reduce the potential for alveolar bone resorption by altering the RANKL/OPG ratio in favor of OPG. On the other hand, increased expression of native HS GAG (ranging continuously from the level measured in diseased gingiva to a 3,5-fold increase) would not significantly affect the gingival inflammation and alveolar bone resorption; the spread of inflammatory cell infiltrate and RANKL/OPG ratio would be stabilized, but at levels close to those measured in diseased gingiva (Figure 11).

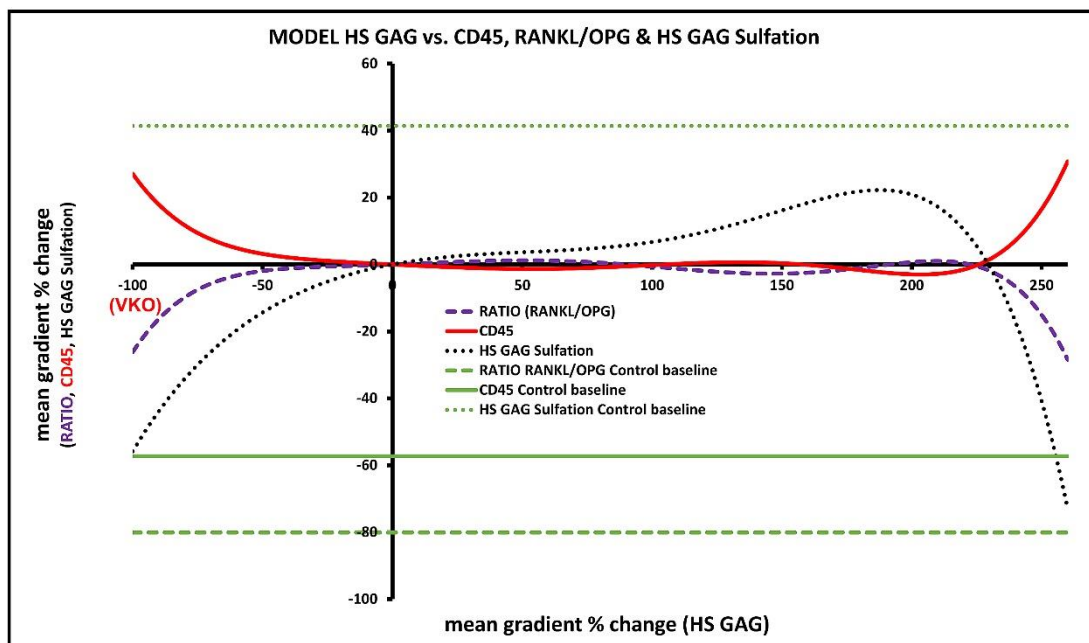


Figure 11. Overall model predictions for the effect of native HS GAG on inflammatory infiltrate in the gingiva and alveolar bone formation/degradation. Note the contrasting effects of altered expression of HS GAG (from VKO to 3,5-fold overexpression of HS GAG from baseline in diseased gingiva) on the RANKL/OPG ratio and CD45. However, for most of the overexpression range, HS GAG is predicted to stabilize the RANKL/OPG ratio and CD45 expression above control values in healthy gingiva.

2.4. DISCUSSION

Periodontitis, a prevalent degenerative disease, is initiated by bacteria present in the subgingival biofilm. These microorganisms trigger an inflammatory response of the host, the progression of which ultimately leads to the degradation of the alveolar bone and surrounding soft tissues that support the teeth resulting in the loss of teeth (77, 78). So far, considerable effort has been dedicated to investigating how host cells and inflammatory mediators regulate the inflammatory response in periodontitis but the contribution of HS GAG (along with its supporting enzymes and receptors) in the development and progress of periodontitis remains relatively unexplored. (3). Therefore, the aim of this thesis was to assess the effects of native HS GAG on inflammatory infiltrate formation and alveolar bone resorption in severe periodontitis in humans using statistical modeling of data from IF staining of human gingiva samples. According to predictions from statistical model, the decreased presence (or absence) of native HS GAG could promote the spread of inflammatory infiltrate while having an inhibitory effect on osteoclastogenic activity by lowering the RANKL/OPG ratio. Conversely, the increase in amount of HS GAG above baseline levels measured in diseased gingiva could stabilize the spread of inflammatory infiltrate and RANKL/OPG. However, both the inflammatory infiltrate and RANKL/OPG ratio would still be above levels measured in healthy gingiva. This means that neither the inflammation nor the bone resorption could be reversed by supplementing native HS GAG content in gingiva of humans affected by severe periodontitis.

The predictions from the model presented here do not fully correspond to the findings from studies on the effects of supplementation of degraded native HS GAG with its synthetic derivative (HS GAG mimetic) performed on experimental rodent models of periodontitis (47-50). The supplementation of native HS GAG by synthetic derivative caused reduction of soft periodontal tissue inflammation and there were detectable signs of periodontal tissue regeneration after the treatment. According to authors, the possible explanation for these findings is related to biochemical properties of synthetic HS GAG which is more resistant to fragmentation by degradative enzymes whose tissue levels and activity are normally increased during inflammation. However, the complete regeneration of alveolar bone (by volume and height) could not be achieved. It was also reported that the described effects depend on the optimal dosage of synthetic

HS GAG – namely, the administration of lower or higher doses of synthetic HS GAG than the optimal one could equally exacerbate the course of experimental periodontitis. There are several reasons for the disparity of findings on the effects of supplementation of native HS GAG during periodontitis and they stem from the diverse physiological roles which HS GAG and HS GAG related proteins have in tissues, as well as from the limitations of different models (either experimental animal models or in silico statistical models) utilized for studying the effects of HS GAG and HS GAG related proteins.

In the first study from the thesis, the differences in expression of factors functionally related to HS GAG between healthy gingiva and gingiva of patients with advanced generalized periodontitis were compared (60). According to findings, the expression profiles of Sdcs exhibit variations between healthy and diseased periodontal tissue which aligns with earlier similar studies (79-81). Furthermore, the differences in expression profiles of enzymes involved in biosynthesis and modification of HS GAG (EXTs, NDSTs, and HPSE1) in healthy and diseased gingiva were also found and they follow similar patterns to those documented in other chronic degenerative disorders, like osteoarthritis (21). Based on that, we formulated the hypothesis that Sdcs and enzymes for HS biosynthesis and modification might play a role in regulation of the inflammatory response in periodontitis. Sdcs possess the capability to interact with an extensive array of inflammation mediators (15). Through these interactions, Sdcs are involved in various segments of the host immune/inflammatory response including the recruitment of leukocytes, formation of chemokine/cytokine gradients, interaction with microbes, and the processes of ECM remodeling during the resolution of inflammation and tissue healing (15, 22, 82). Because of that, Sdcs (and HS GAG for that matter) cannot be designated as strictly pro-inflammatory or anti-inflammatory factors. Evidence for this lies in existing experimental Sdc1 knockout studies of mice colitis and myocardial infarction that demonstrate how Sdc roles in inflammation change depending on both the type of the disease and the tissue it affects. Based on these studies, Sdc1 could be considered as an inhibitor of excessive leukocyte recruitment, where increased neutrophil infiltration and prolonged cardiac/mucosal healing occur (27, 83). However, some amount of Sdc1 is still required for proper leukocyte recruitment because Sdc1 participates in formation of chemokine gradients on endothelial surface of blood vessels (26, 84, 85). While there is a lot of circumstantial evidence about the possible role of HS GAG in inflammation, there are only a few experimental studies which confirm that changes in biochemical properties of HS GAG itself can affect the course of

inflammatory response. Namely, in several studies involving experimental animal models of allergic lung disease and diabetic nephropathy it was reported that the targeted removal of genes responsible for encoding enzymes crucial to HS GAG biosynthesis within endothelial cells can lead to attenuation of inflammatory response (33, 34). This seems to be equally dependent on HS GAG chain length (controlled by EXTs polymerases) and the structure of HS GAG chains regarding the arrangement and sequence of sulfation modifications (regulated by NDSTs) (66, 67, 86). Based on the data presented from the first and the third study of this thesis, it is possible to draw limited conclusions about the changes of quantity and composition of HS GAG in healthy and diseased gingiva. However, different expression profiles of EXT1, NDST1, HPSE1, and HS GAG markers (HS3G10 and HS10E4) suggest that reduction in quantity and structure of gingival HS GAG do occur during periodontitis and that these changes might be involved in dysregulation of the inflammatory response in gingival tissue during periodontitis. What is not entirely clear is whether these changes are the cause of inflammatory response dysregulation in periodontitis, or they are simply reflective of it. Furthermore, the observed correlation between the changes of HS GAG content and structure and the actual enzymatic activity of EXTs, NDSTs and HPSE1 (when deduced based on comparison of expression profiles) is not as straightforward as it seems. For example, the observed upregulated expression of EXTs and downregulated expression of NDSTs did not correspond to increased quantity of less sulfated HS GAG in the diseased gingiva, but rather the decreased quantity of less sulfated HS GAG compared to healthy gingiva. While the lower quantity of HS GAG in diseased gingiva can be partly explained by the increased expression of HPSE1, it should be noted that the actual increase in HPSE1 enzymatic activity could not be confirmed by IF/IHC staining. This is because the commercially available antibodies against HPSE1 do not discriminate between the inactive (pro-enzyme) and active (enzyme) forms of HPSE1 (29-32, 87, 88). In general, the problem with HS GAG and the proteins associated with HS GAG is that their regulatory roles in homeostasis and disease are as diverse as they are tissue and species specific. To assess these roles in humans is difficult because performing experiments for the loss-of-function or gain-of-function on humans is not feasible due to ethical considerations. Therefore, a different approach is required where the effects of inhibition/absence or overexpression of specific factors (usually achieved by knockout/knockin of the corresponding genes or by blocking antibodies against specific proteins in experimental animals) are simulated in silico using statistical modeling. It should be emphasized that the effects on HS GAG and HS GAG

related proteins on the course of disease (in this case periodontitis) could not be postulated simply by comparing their expression profiles in healthy and diseased tissue, nor could they be taken at face value from the previous studies on experimental animals (52, 89).

The main advantage of the model of periodontitis presented in this thesis is that it is based on the raw data obtained from human participants suffering from the real form of severe periodontitis. By combining the data from protein reactome databases and various regression techniques, a dynamic statistical model was created, in which different roles of HS GAG and investigated related proteins could be introduced, while simultaneously replicating the effects of their chaining expression on the outcome(s) of interest. All procedures for statistical modeling as described here were made under the assumption that the key determinants of HS GAG and HS GAG related proteins' biological roles (apart from the biochemical properties of individual molecules) are their hierarchical positioning within regulatory networks and spatial distribution within tissue (90-92). In animal models of periodontitis, researchers can replicate clinical signs of the disease (gingivitis, alveolar bone resorption) but they do so either by application of ligatures around molars (thus artificially expanding the plaque retention surface), by administering mono- or poly-microbe lavage over a period of time, or by combining both ligatures and oral microbe lavage (3, 51, 52, 93, 94). However, the disadvantage of such animal models of periodontitis is that they do not replicate the exact pathogenic mechanisms of periodontitis as it occurs in humans. Furthermore, animal models of periodontitis can only be applied on specific genetic strains (for example AKR/J, DBA/2J, BALB/cJ and BALB/cByJ in mice) as rodents are generally not susceptible to periodontitis (52). These disease models do not reflect the genetic diversity of humans afflicted by this highly prevalent chronic disease. It should be noted that the rodent models of periodontitis can be of greater use when studying rare entities of periodontitis associated with some genetic disorders such as leukocyte adhesion deficiencies, when there is a clear connection between the disease and genetic background (95).

Several study limitations also need to be addressed as previously explained; due to ethical considerations for research on human subjects, it was only possible to create an *in silico* statistical model whose predictions could not be experimentally tested *in vivo*. The model presented here was nested model meaning that not all proteins from the entire HS GAG reactome could be included. For example, no data for the expression of enzymes responsible for HS GAG chain elongation

(EXTL1-3), sulfation (NDST3, NDST4, 2-O- and 3-O-sulfotransferases), other cell-surface/ECM proteoglycans that bind HS GAG (agrin, HSPG2, glypicans) were included in the model. Likewise, in this model there was no representation of gradients of many inflammatory mediators which are formed by HS GAG (21, 96). The limited number of variables used in the model is related to the number of markers whose IF staining gradients on serial histological tissue sections can be successfully quantified and colocalized in silico for modeling. The soft upper limit of 20 to 30 markers therefore depends on the morphological similarity of the serial histological sections if one wants to avoid the introduction of biases and errors (57). This can be significantly improved by application of high-plex single cell IF staining where the same histological section can be stained with multiple markers as was demonstrated with Multi Epitope Ligand Cartography (MELC), the staining technique based on repeated “staining-acquisition-bleaching-staining” cycles where the same histological section can be stained with up to 100 different markers (90, 97). Recently, a novel high-plex IF staining platform was introduced that performs simultaneous IF staining of up to 15 markers on the same histological section ending with H&E staining for morphology (98-100). Potentially, this could increase the number of markers suitable for modeling by 5- to 10-fold. It should also be noted that the statistical modeling protocol itself still needs to be optimized. In particular, curve fitting in first level models is extremely time consuming, as knots or inflection points for curve trends from 2D plots of spatial gradients of IF staining which contain many data points (several thousand data points on average), must be positioned manually. It should be investigated in the future if the process can be fully or partially automated by using dedicated trend analysis software or artificial intelligence platforms (101).

Finally, it should be emphasized that the statistical model presented in this context is not deterministic and requires extension. However, statistical modeling with human tissue data could be used as an alternative way to evaluate potential molecular targets for novel therapeutics and provide a basis for in vivo experiments aimed at alternative treatments for chronic diseases such as severe periodontitis. This applies to both experimental animals and human subjects. This is particularly crucial for chronic diseases, as their complex pathogenic mechanisms are difficult to faithfully replicate in controlled laboratory settings.

2.5. CONCLUSIONS

According to the presented statistical model's predictions, it is proposed that introducing native HS GAG supplementation may offer some potential benefits in managing severe periodontitis in humans. However, this should not be considered a standalone treatment, as observed in experimental animal models of periodontitis. The model supports the idea that intrinsic alterations in the molecular structure of periodontal tissue play a crucial role in the irreversible progression of severe periodontitis. This suggests that effectively influencing the host's immune response for severe periodontitis treatment should extend beyond the conventional approach, which primarily focuses on controlling infectious agents within the microbial biofilm. Supplementing and/or targeting deteriorated ECM components with their synthetic counterparts (such as HS GAG mimetics) could prove beneficial in enhancing the outcomes of standard treatment for severe forms of periodontitis, which typically falls short of achieving periodontal tissue regeneration.

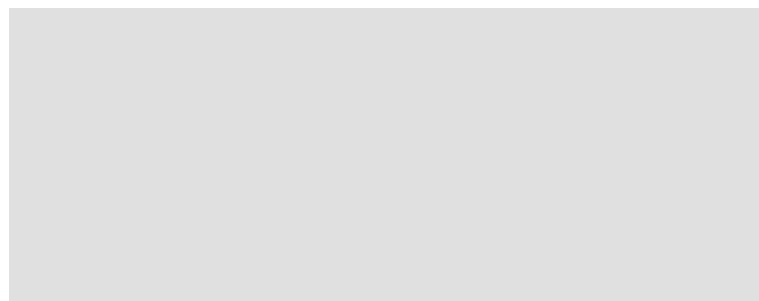
2.6. ABSTRACT

Periodontitis is a highly prevalent chronic degenerative disease initiated by the bacteria present in biofilm on the surface of the teeth. The exposure to bacterial biofilm triggers host inflammatory response whose dysregulation is ultimately responsible for the destruction of hard and soft periodontal tissues resulting in tooth loss. Since chronically inflamed periodontal tissue exhibits extracellular matrix (ECM) degradation, the possible alternative and/or addition to standard periodontitis treatment is to restore ECM by supplementing its components, including heparan sulfate glycosaminoglycan (HS GAG). In experimental animal models of periodontitis, the use of synthetic derivatives of HS GAGs to supplement degraded ECM has shown effectiveness in reducing inflammation and promoting partial regeneration of both soft and hard periodontal tissues. However, the effects of HS GAG supplementation for treating periodontal disease in humans remains are still unknown. To address this uncertainty, a statistical model was developed to assess the effect of HS GAG supplementation on inflammatory infiltrate formation and alveolar bone resorption in humans with severe periodontitis. Gingival samples from patients with severe periodontitis were stained with markers for HS GAG and proteins functionally related to HS GAG (immunofluorescence). A statistical model in the form of a system of regression equations was constructed using quantified spatial gradients of IF staining and the ontology database for STRING reactomes, to predict the effects of changes in the expression of native HS GAG on the amount of inflammatory infiltrate (represented by the general inflammatory cell marker CD45) and alveolar bone resorption (represented by the expression ratio of receptor activator of nuclear KB-ligand (RANKL) and osteoprotegerin (OPG)). According to the model, increased expression of native HS GAG may stabilize the accumulation of inflammatory infiltrate in the gingiva and slow the resorption of alveolar bone, but not stimulate alveolar bone resorption Therefore, supplementation of native HS GAG may have limited benefits as a standalone treatment for severe periodontitis in humans.

2.7. SAŽETAK

Parodontitis je česta degenerativna bolest koju iniciraju bakterije prisutne u biofilmu nastalom na površini zuba. Izloženost bakterijskom biofilmu pokreće upalni odgovor domaćina čija je deregulacija u konačnici odgovorna za uništavanje tvrdih i mekih parodontnih tkiva što rezultira gubitkom zuba. Budući da u kronično upaljenom parodontnom tkivu dolazi do razgradnje izvanstaničnog matriksa (ECM), moguća alternativa i/ili dodatak standardnom liječenju parodontitisa je obnavljanje ECM-a suplementacijom njegovih komponenti, uključujući i heparan sulfat glikozaminoglikan (HS GAG). Suplementacija ECM-a sintetičkim derivatima HS GAG na eksperimentalnim životinjskim modelima pokazala je relativnu učinkovitost u smanjenju upale i poticanju regeneracije mekih i tvrdih parodontnih tkiva. Međutim, opravdanost upotrebe sintetičkih derivata HS GAG za liječenje parodontne bolesti kod ljudi i dalje je nejasna. Stoga, razvijen je statistički model za procjenu utjecaja HS GAG-a u formiranju upalnog infiltrata i resorpciji alveolarne kosti kod ljudi s teškim oblikom parodontitisa. Uzorci gingive od ispitanika s teškim oblikom parodontitisa bojani su biljezima za HS GAG i proteine funkcijski povezane s HS GAG (imunofluorescencija). Statistički model u obliku sustava regresijskih jednadžbi konstruiran je prema kvantifikatima bojenja i ontološkoj bazi podataka za reaktome *STRING* kako bi se predvidjeli učinci promjene izražaja nativnog HS GAG-a na promjene u količini upalnog infiltrata (prikazan općim biljegom upalnih stanica CD45) i resorpcije alveolarne kosti (prikazane omjerom izražaja receptora aktivatora jezgrenog KB liganda (RANKL) i osteoprotegerina (OPG)). Prema modelu povećan izražaj nativnog HS GAG-a može stabilizirati nakupljanje upalnog infiltrata u gingivi i usporiti resorpciju alveolarne kosti, ali ne i potaknuti regeneraciju alveolarne kosti. Stoga, suplementacija nativnog HS GAG-a može imati samo ograničene koristi za liječenje teškog oblika parodontitisa kod ljudi.

2.8. CURRICULUM VITAE



Education and qualifications:

- 2020.–2023: *University of Split, University Department of Forensic Sciences*: graduate study program – Forensic Chemistry and Molecular Biology (Master of Forensics)
- 2018.–2023: *University of Split, School of Medicine*: doctoral study program – Biology of Neoplasms (Doctor of Philosophy – biomedical sciences)
- 2010.–2016: *University of Split, School of Medicine*: integrated undergraduate and graduate university study program – Dental Medicine (Doctor of Dental Medicine)

Work experience:

- 2017.–today: *University of Split, School of Medicine*: university assistant
- 2021.–today: *DR. DAVID digitalna ortodoncija d.o.o.*: dental medicine doctor
- 2018.–2021: *Stomatološka ordinacija dr. Zoran Kučinić*: dental medicine doctor
- 2017.–2017: *Dom zdravlja Osijek*: dental medicine doctor
- 2016.–2017: *Burow d.o.o.*: dental medicine doctor

Publications and other works:

- Duplancic R, Roguljic M, Bozic D, Kero D. Heparan sulfate glycosaminoglycan is predicted to stabilize inflammatory infiltrate formation and RANKL/OPG ratio in severe periodontitis in humans. *Bioengineering*. 2022;9(10):566. – **journal article**
- Duplancic R, Kero D. Histograms and 2D plot profiling for quantification of numerous immunofluorescent signals on entire panoramic photomicrographs: A new method description. 2021 6th International Conference on Smart and Sustainable Technologies (SpliTech). 2021. – **conference paper**

- Duplancic R, Kero D. Novel approach for quantification of multiple immunofluorescent signals using histograms and 2D plot profiling of whole-section panoramic images. *Scientific Reports*. 2021;11(1):8619. – **journal article**
- Duplancic R, Poklepović Peričić T, Vladislavć N D. Klinička procjena oralnog stanja i održavanje oralne higijene u posebnim skupinama. In: *Prevenција u Dentalnoj Medicini*. Zagreb, Croatia: Medicinska Naklada; 2021. p. 45–80. – **book chapter**
- Poklepović Peričić T, Duplancic R, Jerković D, Kovačić I, Pejda Repić S, Gavić L. Klinička procjena oralnog stanja i održavanje oralne higijene u posebnim skupinama. In: *Prevenција u Dentalnoj Medicini*. Zagreb, Croatia: Medicinska Naklada; 2021. p. 81–114. – **book chapter**
- Duplancic R, Roguljic M, Puhar I, Veccek N, Dragun R, Vukojevic K, et al. Syndecans and enzymes for heparan sulfate biosynthesis and modification differentially correlate with presence of inflammatory infiltrate in periodontitis. *Frontiers in Physiology*. 2019;10:1248. – **journal article**
- Duplancic R, Roguljic M, Puhar I, Veccek N, Dragun R, Kero D. Syndecan and Heparan Sulfate Enzymes in Regulation of Periodontal Disease. 48. Jahrestagung: Die SSP unter Strom: Spannungsfelder in der Parodontologie. 2019. – **conference poster**
- Kero D, Simic Bilandzija T, Duplancic R, Vukojevic K, Saraga Babic M. Analysis of Expression Patterns of Syndecans and Enzymes Involved in Heparan Sulfate Biosynthesis and Degradation in Developing Human Tooth Germs. 8th International Conference on Biotechnology and Bioengineering (8th ICBB). 2018. – **conference poster**

Awards and distinctions:

- 2022: *University of Split, School of Medicine*: award for the best research paper in the field of dental medicine
- 2020: *University of Split, School of Medicine*: award for the best research paper in the field of dental medicine
- 2017: *University of Split*: rector's award for excellence
- 2016: *University of Split, student organization Zubolina*: special recognition for exceptional contribution in establishment, financing, organizing and work support of the organization

- 2014: *University of Split, School of Medicine*: dean's award for exceptional success during the study

Projects:

- 2020.–2022: *Mobile access dental clinic (MADE) (HR-BA-ME570)*: project participant

Languages: Croatian (mother tongue) and English (C1 level)

Hobbies: Fitness, motorcycling, cycling, auto mechanics, nautics, diving, photography, watches, movies and theater

2.9. LITERATURE

1. Slots J. Periodontitis: facts, fallacies and the future. *Periodontol 2000*. 2017;75(1):7-23.
2. Kwon T, Lamster IB, Levin L. Current Concepts in the Management of Periodontitis. *Int Dent J*. 2021;71(6):462-76.
3. Silva N, Abusleme L, Bravo D, Dutzan N, Garcia-Sesnich J, Vernal R, et al. Host response mechanisms in periodontal diseases. *J Appl Oral Sci*. 2015;23(3):329-55.
4. Kassebaum NJ, Bernabe E, Dahiya M, Bhandari B, Murray CJ, Marcenes W. Global burden of severe periodontitis in 1990-2010: a systematic review and meta-regression. *J Dent Res*. 2014;93(11):1045-53.
5. Tonetti MS, Jepsen S, Jin L, Otomo-Corgel J. Impact of the global burden of periodontal diseases on health, nutrition and wellbeing of mankind: A call for global action. *J Clin Periodontol*. 2017;44(5):456-62.
6. Kumar S. Evidence-Based Update on Diagnosis and Management of Gingivitis and Periodontitis. *Dent Clin North Am*. 2019;63(1):69-81.
7. Sanz M, Herrera D, Kerschull M, Chapple I, Jepsen S, Beglundh T, et al. Treatment of stage I-III periodontitis-The EFP S3 level clinical practice guideline. *J Clin Periodontol*. 2020;47(Suppl 22):4-60.
8. Badylak SF, Park K, Peppas N, McCabe G, Yoder M. Marrow-derived cells populate scaffolds composed of xenogeneic extracellular matrix. *Exp Hematol*. 2001;29(11):1310-8.
9. Sculean A, Windisch P, Dori F, Keglevich T, Molnar B, Gera I. Emdogain in regenerative periodontal therapy. A review of the literature. *Fogorv Sz*. 2007;100(5):220-32, 211-9.
10. Sculean A, Nikolidakis D, Nikou G, Ivanovic A, Chapple IL, Stavropoulos A. Biomaterials for promoting periodontal regeneration in human intrabony defects: a systematic review. *Periodontol 2000*. 2015;68(1):182-216.
11. Lieppe T, Alliot C, Verner C, Badran Z, Soueidan A, Struillou X. Papillary Reconstruction using Hyaluronic Acid: A Review. *Oral Health Prev Dent*. 2022;20(1):421-31.
12. Mehta V, Kacani G, Moaleem MMA, Almohammadi AA, Alwafi MM, Mulla AK, et al. Hyaluronic Acid: A New Approach for the Treatment of Gingival Recession-A Systematic Review. *Int J Environ Res Public Health*. 2022;19(21):14330.

13. Ricard-Blum S, Perez S. Glycosaminoglycan interaction networks and databases. *Curr Opin Struct Biol.* 2022;74:102355.
14. Sarrazin S, Lamanna WC, Esko JD. Heparan sulfate proteoglycans. *Cold Spring Harb Perspect Biol.* 2011;3(7):a004952.
15. Teng YH, Aquino RS, Park PW. Molecular functions of syndecan-1 in disease. *Matrix Biol.* 2012;31(1):3-16.
16. Xian X, Gopal S, Couchman JR. Syndecans as receptors and organizers of the extracellular matrix. *Cell Tissue Res.* 2010;339(1):31-46.
17. Gotte M. Syndecans in inflammation. *FASEB J.* 2003;17(6):575-91.
18. Multhaupt HA, Yoneda A, Whiteford JR, Oh ES, Lee W, Couchman JR. Syndecan signaling: when, where and why? *J Physiol Pharmacol.* 2009;60(Suppl 4):31-8.
19. Zappe A, Miller RL, Struwe WB, Pagel K. State-of-the-art glycosaminoglycan characterization. *Mass Spectrom Rev.* 2022;41(6):1040-71.
20. Masola V, Bellin G, Gambaro G, Onisto M. Heparanase: A Multitasking Protein Involved in Extracellular Matrix (ECM) Remodeling and Intracellular Events. *Cells.* 2018;7(12).
21. Chanalaris A, Clarke H, Guimond SE, Vincent TL, Turnbull JE, Troeberg L. Heparan Sulfate Proteoglycan Synthesis Is Dysregulated in Human Osteoarthritic Cartilage. *Am J Pathol.* 2019;189(3):632-47.
22. Farrugia BL, Lord MS, Melrose J, Whitelock JM. The Role of Heparan Sulfate in Inflammation, and the Development of Biomimetics as Anti-Inflammatory Strategies. *J Histochem Cytochem.* 2018;66(4):321-36.
23. Lin X, Wei G, Shi Z, Dryer L, Esko JD, Wells DE, et al. Disruption of gastrulation and heparan sulfate biosynthesis in EXT1-deficient mice. *Dev Biol.* 2000;224(2):299-311.
24. Stickens D, Zak BM, Rougier N, Esko JD, Werb Z. Mice deficient in Ext2 lack heparan sulfate and develop exostoses. *Development.* 2005;132(22):5055-68.
25. Coulson-Thomas VJ. The role of heparan sulphate in development: the ectodermal story. *Int J Exp Pathol.* 2016;97(3):213-29.
26. Kharabi Masouleh B, Ten Dam GB, Wild MK, Seelige R, van der Vlag J, Rops AL, et al. Role of the heparan sulfate proteoglycan syndecan-1 (CD138) in delayed-type hypersensitivity. *J Immunol.* 2009;182(8):4985-93.

27. Floer M, Gotte M, Wild MK, Heidemann J, Gassar ES, Domschke W, et al. Enoxaparin improves the course of dextran sodium sulfate-induced colitis in syndecan-1-deficient mice. *Am J Pathol.* 2010;176(1):146-57.
28. Ishiguro K, Kadomatsu K, Kojima T, Muramatsu H, Iwase M, Yoshikai Y, et al. Syndecan-4 deficiency leads to high mortality of lipopolysaccharide-injected mice. *J Biol Chem.* 2001;276(50):47483-8.
29. Li JP, Vlodayvsky I. Heparin, heparan sulfate and heparanase in inflammatory reactions. *Thromb Haemost.* 2009;102(5):823-8.
30. Poon IK, Goodall KJ, Phipps S, Chow JD, Pagler EB, Andrews DM, et al. Mice deficient in heparanase exhibit impaired dendritic cell migration and reduced airway inflammation. *Eur J Immunol.* 2014;44(4):1016-30.
31. Li JP, Kusche-Gullberg M. Heparan Sulfate: Biosynthesis, Structure, and Function. *Int Rev Cell Mol Biol.* 2016;325:215-73.
32. Vlodayvsky I, Barash U, Nguyen HM, Yang SM, Ilan N. Biology of the Heparanase-Heparan Sulfate Axis and Its Role in Disease Pathogenesis. *Semin Thromb Hemost.* 2021;47(3):240-53.
33. Ge XN, Bastan I, Ha SG, Greenberg YG, Esko JD, Rao SP, et al. Regulation of eosinophil recruitment and allergic airway inflammation by heparan sulfate proteoglycan (HSPG) modifying enzymes. *Exp Lung Res.* 2018;44(2):98-112.
34. Talsma DT, Katta K, Ettema MAB, Kel B, Kusche-Gullberg M, Daha MR, et al. Endothelial heparan sulfate deficiency reduces inflammation and fibrosis in murine diabetic nephropathy. *Lab Invest.* 2018;98(4):427-38.
35. Collins LE, Troeberg L. Heparan sulfate as a regulator of inflammation and immunity. *J Leukoc Biol.* 2019;105(1):81-92.
36. Gopal S. Syndecans in Inflammation at a Glance. *Front Immunol.* 2020;11:227.
37. Tiwari V, Maus E, Sigar IM, Ramsey KH, Shukla D. Role of heparan sulfate in sexually transmitted infections. *Glycobiology.* 2012;22(11):1402-12.
38. Hayashida A, Amano S, Gallo RL, Linhardt RJ, Liu J, Park PW. 2-O-Sulfated Domains in Syndecan-1 Heparan Sulfate Inhibit Neutrophil Cathelicidin and Promote Staphylococcus aureus Corneal Infection. *J Biol Chem.* 2015;290(26):16157-67.

39. McCormick C, Leduc Y, Martindale D, Mattison K, Esford LE, Dyer AP, et al. The putative tumour suppressor EXT1 alters the expression of cell-surface heparan sulfate. *Nat Genet.* 1998;19(2):158-61.
40. Wuppermann FN, Hegemann JH, Jantos CA. Heparan sulfate-like glycosaminoglycan is a cellular receptor for *Chlamydia pneumoniae*. *J Infect Dis.* 2001;184(2):181-7.
41. Park PW, Pier GB, Hinkes MT, Bernfield M. Exploitation of syndecan-1 shedding by *Pseudomonas aeruginosa* enhances virulence. *Nature.* 2001;411(6833):98-102.
42. Park PW, Foster TJ, Nishi E, Duncan SJ, Klagsbrun M, Chen Y. Activation of syndecan-1 ectodomain shedding by *Staphylococcus aureus* alpha-toxin and beta-toxin. *J Biol Chem.* 2004;279(1):251-8.
43. Liang OD, Ascencio F, Fransson LA, Wadstrom T. Binding of heparan sulfate to *Staphylococcus aureus*. *Infect Immun.* 1992;60(3):899-906.
44. Aquino RS, Teng YH, Park PW. Glycobiology of syndecan-1 in bacterial infections. *Biochem Soc Trans.* 2018;46(2):371-7.
45. Aquino RS, Hayashida K, Hayashida A, Park PW. Role of HSPGs in Systemic Bacterial Infections. *Methods Mol Biol.* 2022;2303:605-25.
46. Tribble GD, Lamont RJ. Bacterial invasion of epithelial cells and spreading in periodontal tissue. *Periodontol 2000.* 2010;52(1):68-83.
47. Escartin Q, Lallam-Laroye C, Baroukh B, Morvan FO, Caruelle JP, Godeau G, et al. A new approach to treat tissue destruction in periodontitis with chemically modified dextran polymers. *FASEB J.* 2003;17(6):644-51.
48. Coyac BR, Detzen L, Doucet P, Baroukh B, Llorens A, Bonnaure-Mallet M, et al. Periodontal reconstruction by heparan sulfate mimetic-based matrix therapy in *Porphyromonas gingivalis*-infected mice. *Heliyon.* 2018;4(8):e00719.
49. Lallam-Laroye C, Escartin Q, Zlowodzki AS, Barritault D, Caruelle JP, Baroukh B, et al. Periodontitis destructions are restored by synthetic glycosaminoglycan mimetic. *J Biomed Mater Res A.* 2006;79(3):675-83.
50. Lallam-Laroye C, Baroukh B, Doucet P, Barritault D, Saffar JL, Colombier ML. ReGeneraTing agents matrix therapy regenerates a functional root attachment in hamsters with periodontitis. *Tissue Eng Part A.* 2011;17(17-18):2359-67.

51. Martinon P, Fraticelli L, Giboreau A, Dussart C, Bourgeois D, Carrouel F. Nutrition as a Key Modifiable Factor for Periodontitis and Main Chronic Diseases. *J Clin Med.* 2021;10(2):197.
52. de Vries TJ, Andreotta S, Loos BG, Nicu EA. Genes Critical for Developing Periodontitis: Lessons from Mouse Models. *Front Immunol.* 2017;8:1395.
53. Timmen M, Hidding H, Gotte M, Khassawna TE, Kronenberg D, Stange R. The heparan sulfate proteoglycan Syndecan-1 influences local bone cell communication via the RANKL/OPG axis. *Sci Rep.* 2020;10(1):20510.
54. Papapanou PN, Sanz M, Buduneli N, Dietrich T, Feres M, Fine DH, et al. Periodontitis: Consensus report of workgroup 2 of the 2017 World Workshop on the Classification of Periodontal and Peri-Implant Diseases and Conditions. *J Periodontol.* 2018;89 Suppl 1:S173-S82.
55. World Medical Association Declaration of Helsinki: ethical principles for medical research involving human subjects. *JAMA.* 2013;310(20):2191-4.
56. Kero D, Cigic L, Medvedec Mikic I, Galic T, Cubela M, Vukojevic K, et al. Involvement of IGF-2, IGF-1R, IGF-2R and PTEN in development of human tooth germ - an immunohistochemical study. *Organogenesis.* 2016;12(3):152-67.
57. Duplancic R, Kero D. Novel approach for quantification of multiple immunofluorescent signals using histograms and 2D plot profiling of whole-section panoramic images. *Sci Rep.* 2021;11(1):8619.
58. von Mering C, Huynen M, Jaeggi D, Schmidt S, Bork P, Snel B. STRING: a database of predicted functional associations between proteins. *Nucleic Acids Res.* 2003;31(1):258-61.
59. Yaddanapudi LN. The American Statistical Association statement on P-values explained. *J Anaesthesiol Clin Pharmacol.* 2016;32(4):421-3.
60. Duplancic R, Roguljic M, Puhar I, Veccek N, Dragun R, Vukojevic K, et al. Syndecans and Enzymes for Heparan Sulfate Biosynthesis and Modification Differentially Correlate With Presence of Inflammatory Infiltrate in Periodontitis. *Front Physiol.* 2019;10:1248.
61. Duplancic R, Roguljic M, Bozic D, Kero D. Heparan Sulfate Glycosaminoglycan Is Predicted to Stabilize Inflammatory Infiltrate Formation and RANKL/OPG Ratio in Severe Periodontitis in Humans. *Bioengineering (Basel).* 2022;9(10):566.
62. Jin H, Zhou S, Yang S, Cao HM. Heparanase overexpression down-regulates syndecan-1 expression in a gallbladder carcinoma cell line. *J Int Med Res.* 2017;45(2):662-72.

63. David G, Zimmermann P. Heparanase tailors syndecan for exosome production. *Mol Cell Oncol.* 2016;3(3):e1047556.
64. Yu S, Lv H, Zhang H, Jiang Y, Hong Y, Xia R, et al. Heparanase-1-induced shedding of heparan sulfate from syndecan-1 in hepatocarcinoma cell facilitates lymphatic endothelial cell proliferation via VEGF-C/ERK pathway. *Biochem Biophys Res Commun.* 2017;485(2):432-9.
65. Zhang X, Wang F, Sheng J. "Coding" and "Decoding": hypothesis for the regulatory mechanism involved in heparan sulfate biosynthesis. *Carbohydr Res.* 2016;428:1-7.
66. Presto J, Thuveson M, Carlsson P, Busse M, Wilen M, Eriksson I, et al. Heparan sulfate biosynthesis enzymes EXT1 and EXT2 affect NDST1 expression and heparan sulfate sulfation. *Proc Natl Acad Sci U S A.* 2008;105(12):4751-6.
67. Deligny A, Dierker T, Dagalv A, Lundquist A, Eriksson I, Nairn AV, et al. NDST2 (N-Deacetylase/N-Sulfotransferase-2) Enzyme Regulates Heparan Sulfate Chain Length. *J Biol Chem.* 2016;291(36):18600-7.
68. Buresh-Stiemke RA, Malinowski RL, Keil KP, Vezina CM, Oosterhof A, Van Kuppevelt TH, et al. Distinct expression patterns of *Sulf1* and *Hs6st1* spatially regulate heparan sulfate sulfation during prostate development. *Dev Dyn.* 2012;241(12):2005-13.
69. Kim HJ, Kim HS, Hong YH. Sulfatase 1 and sulfatase 2 as novel regulators of macrophage antigen presentation and phagocytosis. *Yeungnam Univ J Med.* 2021;38(4):326-36.
70. Hastbacka J, Superti-Furga A, Wilcox WR, Rimoin DL, Cohn DH, Lander ES. Atelosteogenesis type II is caused by mutations in the diastrophic dysplasia sulfate-transporter gene (*DTDST*): evidence for a phenotypic series involving three chondrodysplasias. *Am J Hum Genet.* 1996;58(2):255-62.
71. Alper SL, Sharma AK. The SLC26 gene family of anion transporters and channels. *Mol Aspects Med.* 2013;34(2-3):494-515.
72. Agere SA, Kim EY, Akhtar N, Ahmed S. Syndecans in chronic inflammatory and autoimmune diseases: Pathological insights and therapeutic opportunities. *J Cell Physiol.* 2018;233(9):6346-58.
73. Morla S. Glycosaminoglycans and Glycosaminoglycan Mimetics in Cancer and Inflammation. *Int J Mol Sci.* 2019;20(8):1963.

-
74. Misra S, Hascall VC, Markwald RR, Ghatak S. Interactions between Hyaluronan and Its Receptors (CD44, RHAMM) Regulate the Activities of Inflammation and Cancer. *Front Immunol.* 2015;6:201.
 75. Kelly T, Suva LJ, Nicks KM, MacLeod V, Sanderson RD. Tumor-derived syndecan-1 mediates distal cross-talk with bone that enhances osteoclastogenesis. *J Bone Miner Res.* 2010;25(6):1295-304.
 76. Benad-Mehner P, Thiele S, Rachner TD, Gobel A, Rauner M, Hofbauer LC. Targeting syndecan-1 in breast cancer inhibits osteoclast functions through up-regulation of osteoprotegerin. *J Bone Oncol.* 2014;3(1):18-24.
 77. Bosshardt DD, Lang NP. The junctional epithelium: from health to disease. *J Dent Res.* 2005;84(1):9-20.
 78. Pihlstrom BL, Michalowicz BS, Johnson NW. Periodontal diseases. *Lancet.* 2005;366(9499):1809-20.
 79. Oksala O, Haapasalmi K, Hakkinen L, Uitto VJ, Larjava H. Expression of heparan sulphate and small dermatan/chondroitin sulphate proteoglycans in chronically inflamed human periodontium. *J Dent Res.* 1997;76(6):1250-9.
 80. Manakil JF, Sugerman PB, Li H, Seymour GJ, Bartold PM. Cell-surface proteoglycan expression by lymphocytes from peripheral blood and gingiva in health and periodontal disease. *J Dent Res.* 2001;80(8):1704-10.
 81. Kotsovilis S, Tseleni-Balafouta S, Charonis A, Fourmoussis I, Nikolidakis D, Vrotsos JA. Syndecan-1 immunohistochemical expression in gingival tissues of chronic periodontitis patients correlated with various putative factors. *J Periodontal Res.* 2010;45(4):520-31.
 82. Bonnans C, Chou J, Werb Z. Remodelling the extracellular matrix in development and disease. *Nat Rev Mol Cell Biol.* 2014;15(12):786-801.
 83. Vanhoutte D, Schellings MW, Gotte M, Swinnen M, Herias V, Wild MK, et al. Increased expression of syndecan-1 protects against cardiac dilatation and dysfunction after myocardial infarction. *Circulation.* 2007;115(4):475-82.
 84. Li Q, Park PW, Wilson CL, Parks WC. Matrilysin shedding of syndecan-1 regulates chemokine mobilization and transepithelial efflux of neutrophils in acute lung injury. *Cell.* 2002;111(5):635-46.

85. Xu J, Park PW, Kheradmand F, Corry DB. Endogenous attenuation of allergic lung inflammation by syndecan-1. *J Immunol*. 2005;174(9):5758-65.
86. Esko JD, Selleck SB. Order out of chaos: assembly of ligand binding sites in heparan sulfate. *Annu Rev Biochem*. 2002;71:435-71.
87. Sanderson RD, Elkin M, Rapraeger AC, Ilan N, Vlodaysky I. Heparanase regulation of cancer, autophagy and inflammation: new mechanisms and targets for therapy. *FEBS J*. 2017;284(1):42-55.
88. Kero D, Bilandzija TS, Arapovic LL, Vukojevic K, Saraga-Babic M. Syndecans and Enzymes Involved in Heparan Sulfate Biosynthesis and Degradation Are Differentially Expressed During Human Odontogenesis. *Front Physiol*. 2018;9:732.
89. Zhang S, Yu N, Arce RM. Periodontal inflammation: Integrating genes and dysbiosis. *Periodontol 2000*. 2020;82(1):129-42.
90. Schubert W, Bonnekoh B, Pommer AJ, Philipsen L, Bockelmann R, Malykh Y, et al. Analyzing proteome topology and function by automated multidimensional fluorescence microscopy. *Nat Biotechnol*. 2006;24(10):1270-8.
91. Park CC, Georgescu W, Polyzos A, Pham C, Ahmed KM, Zhang H, et al. Rapid and automated multidimensional fluorescence microscopy profiling of 3D human breast cultures. *Integr Biol (Camb)*. 2013;5(4):681-91.
92. Kero D, Saraga-Babic M. Odontogenesis - a masterful orchestration of functional redundancy or what makes tooth bioengineering an intrinsically difficult concept *Journal of Stem Cell Research & Therapy*. 2016;1(3):117-23.
93. Marchesan J, Girnary MS, Jing L, Miao MZ, Zhang S, Sun L, et al. An experimental murine model to study periodontitis. *Nat Protoc*. 2018;13(10):2247-67.
94. Khocht A, Orlich M, Paster B, Bellinger D, Lenoir L, Irani C, et al. Cross-sectional comparisons of subgingival microbiome and gingival fluid inflammatory cytokines in periodontally healthy vegetarians versus non-vegetarians. *J Periodontal Res*. 2021;56(6):1079-90.
95. Moutsopoulos NM, Konkeli J, Sarmadi M, Eskin MA, Wild T, Dutzan N, et al. Defective neutrophil recruitment in leukocyte adhesion deficiency type I disease causes local IL-17-driven inflammatory bone loss. *Sci Transl Med*. 2014;6(229):229ra40.
96. Bishop JR, Schuksz M, Esko JD. Heparan sulphate proteoglycans fine-tune mammalian physiology. *Nature*. 2007;446(7139):1030-7.

97. Schubert W. Topological proteomics, toponomics, MELK-technology. *Adv Biochem Eng Biotechnol.* 2003;83:189-209.
98. Lin JR, Fallahi-Sichani M, Sorger PK. Highly multiplexed imaging of single cells using a high-throughput cyclic immunofluorescence method. *Nat Commun.* 2015;6:8390.
99. Lin JR, Fallahi-Sichani M, Chen JY, Sorger PK. Cyclic Immunofluorescence (CycIF), A Highly Multiplexed Method for Single-cell Imaging. *Curr Protoc Chem Biol.* 2016;8(4):251-64.
100. Lin JR, Chen YA, Campton D, Cooper J, Coy S, Yapp C, et al. High-plex immunofluorescence imaging and traditional histology of the same tissue section for discovering image-based biomarkers. *Nat Cancer.* 2023;4(7):1036-52.
101. Kim HJ, Fay MP, Feuer EJ, Midthune DN. Permutation tests for joinpoint regression with applications to cancer rates. *Stat Med.* 2000;19(3):335-51.

3. POOLED ARTICLES



Syndecans and Enzymes for Heparan Sulfate Biosynthesis and Modification Differentially Correlate With Presence of Inflammatory Infiltrate in Periodontitis

Roko Duplancic^{1†}, Marija Roguljic^{2†}, Ivan Puhar³, Nika Vecek¹, Ruzica Dragun¹, Katarina Vukojevic^{4,5}, Mirna Saraga-Babic^{4,5} and Darko Kero^{1,5*}

OPEN ACCESS

Edited by:

Ariane Berdal,
INSERM U1138 Centre de Recherche
des Cordeliers, France

Reviewed by:

Martin Biosse Duplan,
Université Paris Descartes, France
Javier Catón,
Complutense University of Madrid,
Spain
Silvana Papagerakis,
University of Saskatchewan College of
Medicine, Canada

*Correspondence:

Darko Kero
dkero@mefst.hr

† These authors have contributed
equally in preparation of the
manuscript

Specialty section:

This article was submitted to
Craniofacial Biology and Dental
Research,
a section of the journal
Frontiers in Physiology

Received: 10 May 2019

Accepted: 12 September 2019

Published: 25 September 2019

Citation:

Duplancic R, Roguljic M, Puhar I,
Vecek N, Dragun R, Vukojevic K,
Saraga-Babic M and Kero D (2019)
Syndecans and Enzymes for Heparan
Sulfate Biosynthesis and Modification
Differentially Correlate With Presence
of Inflammatory Infiltrate
in Periodontitis.
Front. Physiol. 10:1248.
doi: 10.3389/fphys.2019.01248

¹ Study Programme of Dental Medicine, School of Medicine, University of Split, Split, Croatia, ² Department of Oral Pathology and Periodontology, Study Programme of Dental Medicine, School of Medicine, University of Split, Split, Croatia, ³ Department of Periodontology, School of Dental Medicine, University of Zagreb, Zagreb, Croatia, ⁴ Department of Anatomy, Histology and Embryology, School of Medicine, University of Split, Split, Croatia, ⁵ Laboratory for Early Human Development, School of Medicine, University of Split, Split, Croatia

Periodontitis is a common degenerative disease initiated by the bacteria in subgingival biofilm. The exposure to bacterial biofilm triggers host inflammatory response whose dysregulation is ultimately responsible for the destruction of hard and soft periodontal tissues resulting in tooth loss. To date, significant effort has been invested in the research of the involvement of host cells and inflammatory mediators in regulation of inflammatory response in periodontitis. Syndecans (Sdcs) belong to a four-member family of heparan sulfate proteoglycans (HSPGs). Sdcs are compound molecules comprised of the core protein to which several heparan sulfate (HS) glycosaminoglycan (GAG) chains are attached. The role of Sdcs in pathogenesis of periodontitis is poorly investigated despite the numerous reports from experimental studies about the critical involvement of these factors in modulation of various aspects of inflammatory response, such as the formation of inflammatory mediators gradients, leukocyte recruitment and extracellular matrix remodeling in resolution of inflammation. Most of these functions of Sdcs are HS-related and, thus, dependent upon the structure of HS. This, in turn, is determined by the combinatorial action of enzymes for biosynthesis and modification of HS such as exostosis (EXTs), sulfotransferases (NDSTs), and heparanase 1 (HPSE1). The data presented in this study clearly indicate that some Sdcs display different expression profiles in healthy and diseased periodontal tissue. Additionally, the differences in expression profiles of HS GAG biosynthesis and modification enzymes (EXTs, NDSTs, and HPSE1) in healthy and diseased periodontal tissue imply that changes in HS GAG content and structure might also take place during periodontitis. Most notably, expression profiles of Sdcs, EXTs, NDSTs, and HPSE1 differentially correlate with the presence of inflammatory infiltrate in healthy and diseased periodontal tissue, which might imply that these factors could also be involved in modulation of inflammatory response in periodontitis.

Keywords: periodontitis, syndecans, heparan sulfate, EXTs, NDSTs, inflammatory response

INTRODUCTION

Periodontitis is a chronic disease which affects tooth supporting tissue (gingiva, alveolar bone, periodontal ligament) causing its gradual degradation to the point where masticatory function of the teeth (or their resilience to occlusal forces) is permanently lost. The etiology of periodontitis is multifactorial – susceptibility to periodontitis can be associated to various demographic factors (age, sex, social background), micro-environmental factors (chronic bacterial and endotoxin exposure from subgingival microbial biofilm), and/or constitutive host traits (both genetic and epigenetic). To a variable degree, all these factors can modulate host inflammatory response, which (if dysregulated) causes progressive destruction of periodontal tissue (Hernandez et al., 2011; Silva et al., 2015).

Syndecans (Sdcs) belong to a four-member family (Sdc1-4) of cell surface heparan sulfate proteoglycans (HSPGs). Sdcs are compound molecules comprised of a cell membrane embedded core protein (divided into cytoplasmic, transmembrane, and ectoplasmic domains) to which several heparan sulfate (HS) glycosaminoglycan (GAG) linear side chains are covalently attached (Bernfield et al., 1992; Gotte, 2003; Multhaupt et al., 2009). With regard to functional versatility of Sdcs and, consequently, their roles in regulation of inflammatory response, there are several important aspects which need to be considered, some of which are more exclusive to Sdcs, and some of which can be broadly associated to HSPGs. In adult tissues, Sdcs are widely distributed, however, the expression domains of individual Sdcs do not completely overlap – Sdc1 is predominantly expressed in stratified and simple epithelia, Sdc2 in connective tissue and endothelial cells, Sdc3 in neural tissue, whereas Sdc4 is expressed ubiquitously. The expression of Sdcs can be very responsive to changes in micro-environment, and this is especially the case in developing tissues during the early stages of organogenesis when expression patterns of Sdcs can significantly deviate from the patterns observed in adult tissues (Vukojevic et al., 2012; Filatova et al., 2014; Kero et al., 2015; Cubela et al., 2016). Studies on *Sdc1*^{-/-} and *Sdc4*^{-/-} single knockout mice have revealed that these animals develop normally, meaning that Sdc1 and Sdc4 are functionally redundant in organogenesis. However, when adult *Sdc1*^{-/-} or *Sdc4*^{-/-} knockouts are challenged by disease-instigating agents they, depending on the type of challenge, display impaired regulation of various segments of inflammatory response – from formation of chemokine/cytokine gradients and leukocyte recruitment, to ECM remodeling in resolution of inflammatory response (Floer et al., 2010; Teng et al., 2012).

Generally, biochemical properties enable HSPGs to bind various factors, and while this binding can be mediated via specific sequences in core protein domains, interactions with extracellular matrix (ECM) components, growth factors, morphogens, and mediators of disease pathogenesis are mostly HS-related (Taylor and Gallo, 2006; Roper et al., 2012; Stepp et al., 2015). Biochemical properties of HS greatly depend on HS chain length and composition (the latter is also determined by adding sulfate groups in a specific pattern). HS can even be post-biosynthetically cleaved into short fragments by enzymes such as heparanase 1 (HPSE1) whose activity

is reportedly elevated in conditions such as inflammation or malignant alteration (Li and Vlodavsky, 2009; Stoler-Barak et al., 2014; Gutter-Kapon et al., 2016). The framework for HS biosynthesis is laid down by the combinatorial action of several enzymes including exostosin-glycosyltransferases (Exts/EXTs) (chain elongation) and bi-functional sulfotransferases (Ndsts/NDSTs) (initial sulfation modifications) (Esko and Selleck, 2002; Presto et al., 2008). Although the non-redundancy of particular Exts/EXTs and/or Ndsts/NDSTs in organogenesis has been long established, recent studies on targeted endothelial ablation of various genes encoding for HS biosynthesis enzymes show that they are also critical for regulation of inflammatory response, pretty much in the same manner as previously described for Sdcs in challenged *Sdc1*^{-/-} and *Sdc4*^{-/-} knockouts (Poon et al., 2014; Ge et al., 2018; Talsma et al., 2018).

There are only few studies about the possible involvement of Sdcs in pathogenesis of periodontitis in humans (Oksala et al., 1997; Manakil et al., 2001; Kotsovilis et al., 2010). While the differential expression of several HSPGs (Sdc1, CD44, decorin, and biglycan) between healthy and diseased periodontal tissue was reported, there were no data about other functionally related factors to HSPGs, including the enzymes for biosynthesis and modification of HS. Furthermore, due to less advanced imaging techniques and methods for quantification of immunohistochemical staining, no adequate correlation of observed expression patterns with various histomorphometric parameters relevant for the subject could be done. Therefore, we sought to provide more detailed description of expression patterns of Sdcs and enzymes for biosynthesis and modification of HS in healthy and diseased human periodontal tissue, as well as to discuss our findings in light of the important roles generally attributed to HSPGs in regulation of inflammatory response.

MATERIALS AND METHODS

Participants Screening and Recruitment

40 patients were referred from their appointed general practitioners to the Department of Oral Pathology and Periodontology, University of Split Hospital Center, and the Department of Periodontology, University of Zagreb Hospital Center. Standard protocol was used to determine diagnosis including detailed medical history, radiographic examination and periodontal status. Periodontal status was assessed by two experienced and calibrated dental examiners who recorded probing depth (PD), gingival recession (RE), clinical attachment level (CAL), full-mouth plaque (FMPS), and bleeding (FMBS) scores. Clinical measurements were taken at six sites per tooth using a standard periodontal probe (PCP 15; Hu-Friedy, Chicago, IL, United States). The diagnosis was established according to new classification of periodontal and implant diseases and conditions (Papapanou et al., 2018). Participants were informed about the purpose of this study and clinical procedures related to it, and gave their written consent.

The inclusion criteria were: age of at least 18 years, good general health (no systemic diseases), healthy periodontal tissue (controls) and generalized periodontitis stage III or IV

(periodontitis group) according to guidelines for classification of periodontal and peri-implant diseases (Papapanou et al., 2018). The exclusion criteria were: presence of periodontal abscess and endo-periodontal lesions in the vicinity of the sampling area, systemic conditions affecting periodontal tissue (e.g., diabetes mellitus), long-term medication, medical history of systemic antibiotic therapy within the last 6 months, pregnancy, alcohol, or drug abuse. Participants were divided into two groups: subjects with healthy periodontal tissue (controls; $n = 20$), and subjects with untreated generalized periodontitis (stage III or IV) having at least one tooth indicated for extraction due to poor condition of periodontal tissue (periodontitis group; $n = 20$). Group demographics and clinical parameters are listed in **Table 1**.

Participants with periodontitis received initial periodontal therapy (1 visit per quadrant) in period of 7 days by two experienced periodontists. In the initial visit, a single tooth was extracted using periosteal elevator (Aesculap AG, Tuttlingen, Germany) for atraumatic extraction. The sample of diseased gingiva (from gingival margin to the edge of residual alveolar bone) was taken with a type 15C scalpel blade (Aesculap AG, Tuttlingen, Germany) on the buccal aspect of tooth extraction site (average sample dimensions 4 mm \times 2,5 mm). Extraction sites were sutured with monofilament sutures (Péters Surgical, Bobigny, France).

Participants from control group were initially referred for crown lengthening with regard to preparation for prosthetic therapy either by general practitioners or prosthodontists. Surgical crown lengthening was performed under local anesthesia and included external gingivectomy (used for the sampling of healthy gingiva), as well as osteotomy and osteoplasty. The samples of healthy gingiva (average dimensions 2,5 mm \times 1,5 mm) were taken from the buccal aspect of gingival margin down to the alveolar bone margin (before the osteotomy and osteoplasty were performed). Sampling sites were sutured with monofilament sutures (Péters Surgical, Bobigny, France). After the samples were taken, they were stored in sealed containers with paraformaldehyde and delivered to laboratory within 24 h. The follow-up of participants from

both groups adhered to established guidelines for the type of treatment they received.

Human Gingival Samples Procurement and Processing

For this study, the total of 40 samples of human gingiva (20 per group) were analyzed. Tissue procurement and processing were approved by the Ethical and Drug Committee of School of Medicine, University of Split (Class: 003-08/17-03/0001, No: 2181-198-03-04-17-0043) and Ethical and Drug Committee of School of Dental Medicine, University of Zagreb (No: 05-PA-15-6/2017) in accordance with Helsinki Declaration (Williams, 2008). Before the fixation in 4% paraformaldehyde, vestibular (labial/buccal) surfaces of gingival samples were marked by waterproof color in order to facilitate proper orientation of the samples during paraffin embedding. The samples were cut in serial 5 μ m thick sections and mounted on glass slides. Preservation of the tissue and positioning of the structures of interest were examined on orientation slides stained with hematoxylin and eosin (H/E) (every 10th slide in each sample). After that, part of the samples was stored in the archival collection of the Department of Anatomy, Histology and Embryology (School of Medicine, University of Split) and designated with unique depersonalized codes to hide the identity of sample donors, and the rest was used for immunofluorescence staining.

Immunofluorescence Staining

Deparaffinization and staining protocols were previously described (Kero et al., 2016). We slightly modified the staining protocol by introduction of protein blocking (ab64226; Abcam, United Kingdom) for 30 min before the application of primary antibodies. The following primary antibodies were used: mouse monoclonal anti-Sdc1 [B-A38] (1:100, ab34164, Abcam, United Kingdom), rabbit polyclonal anti-Sdc2 (1:200, ab191062, Abcam, United Kingdom), rabbit polyclonal anti-Sdc4 (1:100, ab24511, Abcam, United Kingdom), rabbit polyclonal anti-EXT1 (1:100, ab126305, Abcam, United Kingdom), rabbit polyclonal anti-EXT2 (1:50, ab102843, Abcam, United Kingdom), rabbit polyclonal anti-NDST1 (1:50, Abcam, United Kingdom), rabbit polyclonal anti-NDST2 (1:100, ab1511141, Abcam, United Kingdom), rabbit polyclonal anti-HPSE1 (1:200, ab85543, Abcam, United Kingdom) and mouse monoclonal anti-CD45 [MEM-28] (1:200, ab8216, Abcam, United Kingdom) as a general inflammatory cell marker (Wu et al., 2018). Secondary antibodies were used at 1:400 dilution: anti-mouse Alexa Fluor 488 (GREEN, ab150105, Abcam, United Kingdom), anti-rabbit Alexa Fluor 594 (RED, ab150092, Abcam, United Kingdom), and anti-rabbit Alexa Fluor 488 (GREEN, ab150077, Abcam, United Kingdom). To stain cell nuclei, sections were shortly incubated with 4'6'-diamidino-2-phenylindole (DAPI). Samples of oral mucosa from maxillary tuberosity were stained for positive control (total of 30 sections on 15 slides). Both single and double immunofluorescence staining was performed. For double immunofluorescence control, mouse anti-Sdc1 and anti-CD45 were stained in tandem with the rest of the primary antibodies (all rabbit polyclonal) and compared with single

TABLE 1 | Demographic and clinical parameters of participants from control and periodontitis group.

	Controls ($n = 20$)	Periodontitis ($n = 20$)
Age*** (years)	38,9 \pm 9,23	50,26 \pm 10,6
Sex (F/M)	8 F/12 M	9 F/11 M
Smokers***	No	17
FMPS* (%)	21,95 \pm 8,95	36,17 \pm 15,76
FMBS*** (%)	8,95 \pm 3,73	43 \pm 11,27
PD*** (mm)	1,47 \pm 0,22	4,53 \pm 1,19
CAL*** (mm)	1,52 \pm 0,22	6,1 \pm 1,43

FMPS, Full Mouth Plaque Score; FMBS, Full mouth bleeding score; PD, Probing depth; CAL, Clinical attachment level. Level of significance was set at $\alpha = 0,01$ (** $p < 0,01$; $F_{crit} = 7,325545$); (*border values, level of significance $\alpha = 0,05$); Statistically significant difference between the groups was found for age ($p = 0,007571$), smoking ($p = 0,000001$), FMPS ($p = 0,001056$), FMBS ($p = 0,000216$), PD ($p = 0,000579$), and CAL ($p = 0,000631$). No statistically significant difference was found for sex distribution between groups ($p = 1$).

immunofluorescence staining. Expression patterns (nuclear vs. non-nuclear) were analyzed by intensity correlation analysis of photo-micrographs at magnifications $\times 20$ and $\times 40$ in ImageJ (NIH Public Domain, Bethesda, MD, United States) according to previously described method (Kero et al., 2017). Color scatter-plots for all primary antibodies displayed non-nuclear expression pattern (data not shown).

Acquisition and Processing of H/E Panoramic Images

H/E stained slides were examined under Olympus BX40 (Olympus, Tokyo, Japan) microscope equipped with manual slide scanner (Microvisioner, Esslingen am Neckar, Germany), standard (Olympus DP27, Olympus, Japan) and area-scan high-resolution camera (Basler aceA2500-14gm, Basler, Germany). H/E panoramic images were captured at magnification $\times 20$ (camera settings – exposure time: 8 ms; ISO: 100). Panoramic images were exported and processed in Adobe Photoshop® CC (2014). Rotation of panoramic images was done using 40 customized presets (one for each sample), and high resolution background (600 dpi) was used for image size reduction in order to minimize image detail loss. Additionally, regions of epithelial tissue on each panoramic image were masked using graphic pen tablet (Wacom Intuos PRO, Wacom Co, Saitama, Japan). Total section area and areas of specific tissue compartments (epithelia, subepithelial stroma) were then measured in Adobe Photoshop® CC and expressed in pixels (px).

Acquisition and Processing of Panoramic Immunofluorescence Images

Slides stained for immunofluorescence were examined at $\times 10$ magnification using Zeiss Axio Observer (Carl Zeiss Microscopy GmbH, Jena, Germany) equipped with Zeiss Axiocam 506 color camera (Carl Zeiss Microscopy GmbH, Jena, Germany) set for full frame resolution (2752×2208 px) in original black and white and 8-bit depth (256 px values) pseudo-colorizer mode. Acquisition and merging of photo-micrographs into panoramic immunofluorescence (IF) images were done using multichannel and panorama modules in ZEN 2.5 software (Carl Zeiss Microscopy GmbH, Jena, Germany), respectively. After background calibration (0 px), exposure time in multichannel module was set at 35 ms for DAPI. For green (AF488) and red (AF594) fluorescence, exposure time was additionally calibrated after signal output equalization at 800 ms (green) and 12000 ms (red) (green and red fluorescence to Sdc1 used as reference). For the stitching of photo-micrographs (tiles) into panoramic IF images, tiles were captured sequentially by manual navigation along x/y axes guided by the on-screen live view of DAPI channel with minimal 20% overlap (x) and 10% maximal shift (y) between individual tiles. Panoramic IF images were closely inspected for quality (tiles alignment, absence of stitching artifacts) and stored in raw format (CZI – Zeiss proprietary file format) containing original data and metadata. Each file was then exported in multiple TIFF format files (original black and white, pseudo-colored and merged files). Black and white images were subsequently processed for quantification of staining. Rotation

and masking were done in a similar manner described for panoramic H/E images, although more restrictive procedure for image size reduction (300 dpi backgrounds) had to be applied in order to format files for analysis in ImageJ. For the calculation of total section area, merged IF panoramic images (factor/DAPI) were thresholded at 1 px (cut-off threshold was set at 10 px). In order to measure the area of epithelial and subepithelial tissue compartments, images were merged with customized black and white masks using “darken image” blending mode in Adobe Photoshop® CC. Thus, for each panoramic IF image, five additional images were produced (threshold area, mask, inverted mask, epithelial, stromal). All area measurements were subsequently used as reference values for the calculation of expression domain size (cumulative and fractional output) so they could be expressed in percentages (%).

Intensity Distribution – Histograms and Heatmaps

Histograms for panoramic IF images were made in ImageJ and exported as tables where for each x value (intensity in px from 0 to 255 px) a y-value (number of points with corresponding intensity) is listed. The tables were then used to calculate the size of expression domains (cumulative and fractional values expressed in%) in individual samples and as group means. Since we set the cut-off at 10 px, each table contained 245 values. Tables with cumulative and fractional values were also used for statistical analysis. The protocol for multi-color heatmaps was described previously (Kero et al., 2018). Here, we have only slightly modified the increments of intensity range in order to accommodate for four-color heatmaps as follows: blue (10–60 px), green (60–150 px), red (150–255 px), and yellow (255 px).

Densitometry – 2D Plot Profiles and 3D Surface Plots

To represent expression patterns in the form of spatial gradients, 2D plot profiles and 3D surface plots of panoramic IF images were made as described previously (Kero et al., 2018). However, we omitted the conversion of px values to optical density units. For each investigated factor, 2D plot profiles were made in oral-sulcular direction (left-right plot), as well as in marginal-apical direction (top-down plot) (Figure 4). Multiple colocalization of expression patterns of all investigated factors was done by 3D surface plots.

Statistical Analysis

The following histomorphometric parameters were analyzed for each sample: total section, epithelial and stromal compartment areas, total, epithelial, and stromal cellularity (using DAPI nuclear staining) and internuclear space, total and stromal distribution of inflammatory infiltrate (using CD45 staining), and total, epithelial and stromal areas of expression domains of investigated factors. In both groups, a group mean of the area of expression domains of each investigated factor was calculated (represented in percentages as fractional values on 10–255 px scale) for total section and tissue compartments (epithelial/stromal). Cumulative values of

histomorphometric parameters were presented by column graphs. Single factor ANOVA was used for comparison of expression domains between control and test group. Correlation of expression domains was done by multiple linear regression. In order to reduce bias of statistical analyses of histomorphometric parameters and expression patterns of investigated factors, sections from both groups were divided into two major tissue compartments – epithelial compartment and subepithelial stroma compartment. The epithelial compartment included gingival oral epithelium, sulcus epithelium and pocket epithelium (when preserved in samples from periodontitis group). Demographics and clinical parameters of study participants were also analyzed (descriptive statistics, *t*-test for continuous variables and Fisher's exact test for categorical variables). Statistical tests were performed in Microsoft Office Excel® 2016 (Microsoft Corp., Redmond, WA, United States) and GraphPad v8 (GraphPad Software, La Jolla, CA, United States). Statistical significance (α) was set at 0.01 ($p < 0.01$).

RESULTS

Histomorphometry – Tissue Morphology and Celularity

In general terms, gingiva is comprised of two major tissue compartments – epithelial tissue (stratified epithelium) and underlying connective tissue (subepithelial stroma). Using the panoramic H/E images (Figures 1A,C,D,F), the area size of epithelial and stromal compartments for each sample was calculated as a fraction of total section and subsequently expressed in percentages as group means. On average, epithelial/stromal fraction for controls was 29,27/70,87%, and for periodontitis group 24,27/75,73% ($p = 0,63899$). No statistically significant difference was found between the groups (Figure 2A) meaning the overall tissue section morphology should not be considered as a confounding factor for further statistical analyses. Total celularity of tissue samples was calculated as a fraction of area covered by DAPI nuclear staining (Figures 1B,E) from the total section area and expressed in percentages as group means. Surprisingly, there was no statistically significant difference between the groups – total nuclei/internuclear space fraction for controls was 22,55/77,45%, and for periodontitis group 28,31/71,69% ($p = 0,12603$) (Figures 2B,C). However, once the celularity was calculated separately for epithelial and stromal compartments, the differences between the groups became apparent. Namely, epithelial/stromal nuclei ratio in controls was 1:1 (49,54/50,46%), whereas in periodontitis group it was almost 1:2 in favor of stromal compartment (34,36/65,54%) ($p = 0,00371$) (Figure 2D). There are couple of possible explanations for such findings. Epithelial/stromal celularity ratio in periodontitis group could be partially attributed to the increased presence of inflammatory cells, which in some cases diffusely infiltrated subepithelial stroma (Figures 1K,L, 3N). The expression of general inflammatory cell marker CD45 was also found to be statistically significantly different between controls and periodontitis group (stromal ratio 1,76/9,47%, $p = 0.00349$)

(Figure 7D). It should be noted that in several gingival samples from periodontitis group, the inflammatory cell infiltrate was limited to narrow perivascular spaces in subepithelial stroma, and its amount was on comparable levels to those observed in controls (Figures 1J, 3E, 5B), so it is possible that changes in other cell populations might also be accounted for differences in epithelial/stromal celularity ratios between the groups.

Expression of Sdcs and HPSE 1 – IHC and Densitometry

In controls, the expression of individual Sdcs could be seen in both gingival epithelium and subepithelial stroma but did not significantly deviate from the previously established pattern – Sdc1 was predominant in epithelial compartment, Sdc2 in stromal compartment, while the expression of Sdc4 was equally balanced between the two tissue compartments but at lower levels than expression of Sdc1 and Sdc2 (Figures 3A–C). Very weak expression of HPSE1 was observed in subepithelial stroma (Figure 3D). 2D plot profiles for Sdcs reveal either decreasing mean expression intensity gradients in oral-sulcular direction, and flat gradients in marginal-apical direction (Figures 4A,G). Low mean expression intensity and flat intensity gradients could be seen for HPSE1 and CD45 in both 2D plot profiles (Figures 4E,K). In periodontitis group, the expression of Sdcs and HPSE1 maintained similar patterns in gingival epithelium as observed in controls, but they were more intensely expressed in subepithelial stroma (Figures 3J–L, 6A,B,D,E). Consequently, changes in mean intensity levels and gradients could be observed in both types of 2D plot profiles (Figures 4B,H,E,L, 6C,F) showing increasing trend toward sulcular and apical portions of subepithelial stroma where more intense expression of inflammatory marker CD45 was also observed.

Expression of EXTs and NDSTs – IHC and Densitometry

In controls, the expression of EXT1 was very weak, whereas EXT2, NDST1, and NDST2 were expressed strongly in epithelial compartment and less intensely throughout the subepithelial stroma (Figures 3F–I). 2D plot profiles reveal decreasing mean expression intensity gradients for EXT2, NDST1, and NDST2 in oral-sulcular direction, and opposing increasing intensity gradients in marginal-apical direction (Figures 4C,I). In periodontitis group, the expression of EXTs and NDSTs was increased in subepithelial stroma significantly overlapping with expression domain of CD45 (Figures 3O–R). 2D plot profiles reveal markedly elevated mean intensity gradient of EXT1 which increases in sulcular and apical direction (Figures 4D,J). In contrast to controls, the expression patterns of EXTs and NDSTs (especially EXT1 and NDST1) displayed a lot of variations in samples from periodontitis group (Figures 3O–R, 5K–N), which could be related to varying histological features of stromal compartments, especially with regard to the extent and profile of inflammatory infiltrate. However, these deviations in EXTs and NDSTs molecular profiles are visible in both gingival epithelium (Figures 6A–C) and subepithelial stroma (Figures 6D–F).

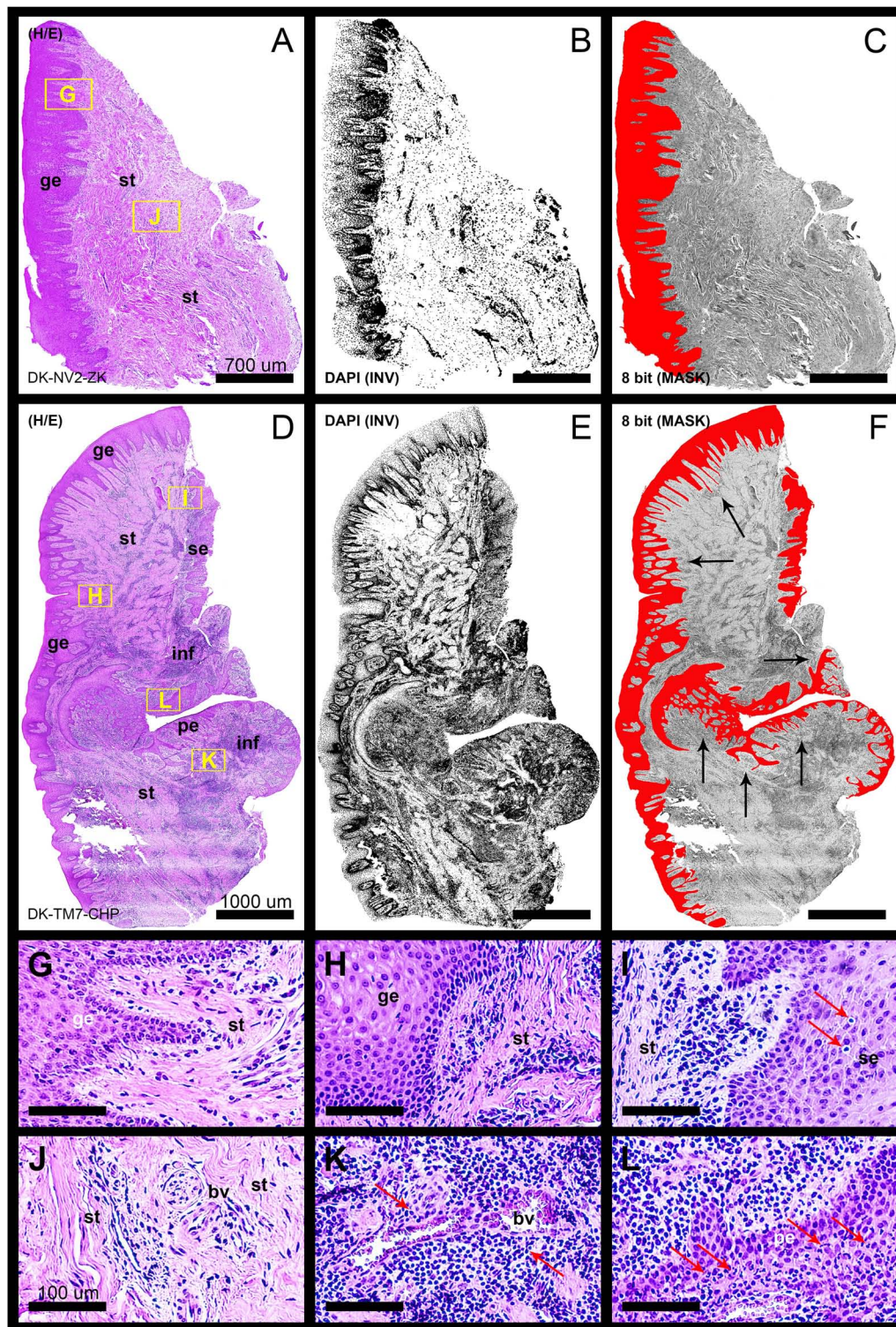
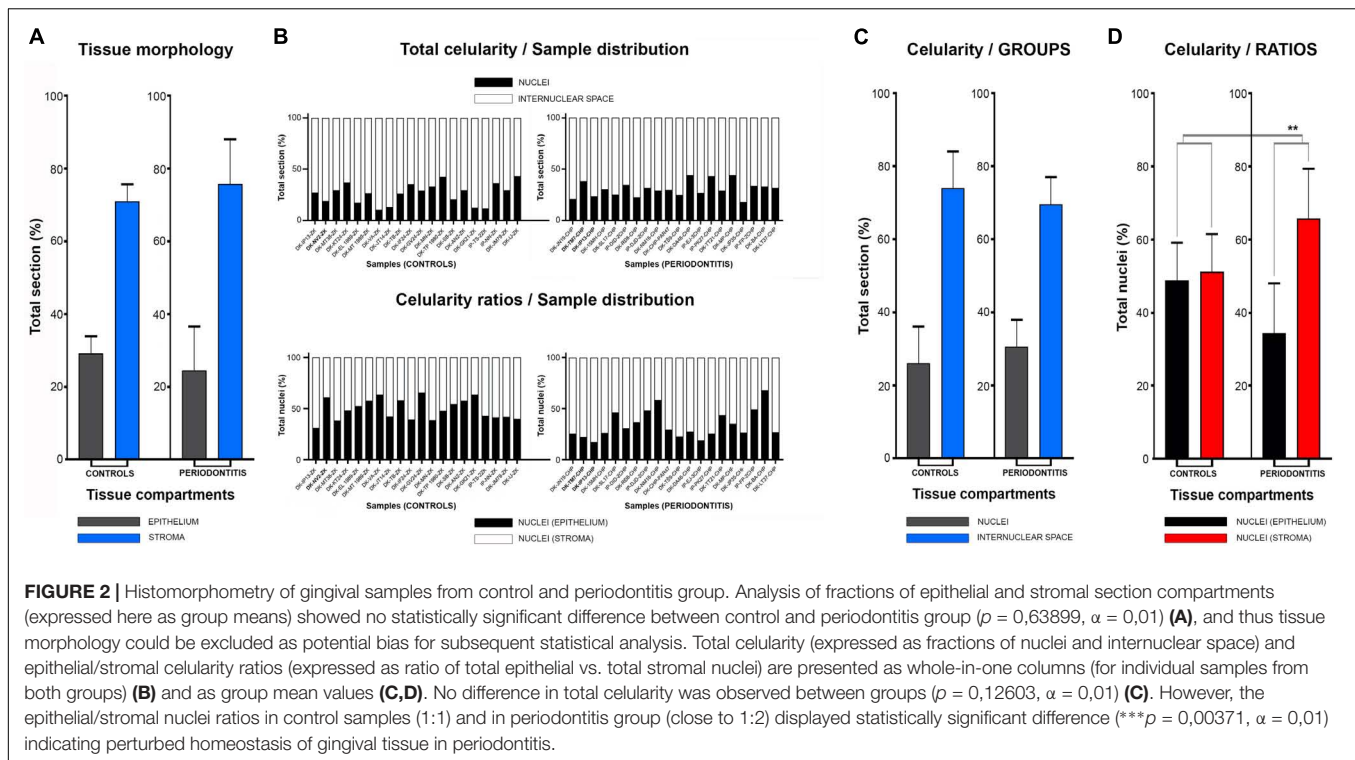


FIGURE 1 | Panoramic H/E images (A,D) of healthy (control sample DK-NV2-ZK) and diseased gingiva (periodontitis sample DK-TM7-CHP). In contrast to thickened gingival epithelium (C) and clear subepithelial stroma with scarce perivascular inflammatory infiltrate (B,G,J) of healthy gingiva, the diseased gingiva displays thinned gingival epithelium with no cytologic atypia but extended rete pegs and features of pseudoepithelial hyperplasia from the pocket epithelium (F, black arrows). The abundant inflammatory infiltrate can be seen along the perivascular spaces (K, red arrows) and diffusely toward sulcular and apical segments of the gingiva (E,I,L) comprised mostly of lymphocytes. Few lymphocytes infiltrating sulcus epithelium are visible (I, red arrows). Pocket epithelium is infiltrated by many granulocytes (L, red arrows). The difference in total cellularity levels between healthy and diseased gingiva are clearly visible on inverted DAPI panoramic images (B,E). Magnification: (A–L) $\times 20$; scale bars – (A–C) 700 μm ; (D–F) 1000 μm ; (G–L) 100 μm . Designations: gingival epithelium (ge), subepithelial stroma (st), sulcus epithelium (se), pocket epithelium (pe), inflammatory infiltrate (inf), blood vessel (bv).



Statistical Analysis of Sdcs, HPSE1, EXTs, and NDSTs Expression Domains

The initial comparison of group means for total expression domains of all investigated factors at level of significance $\alpha = 0,01$ revealed that only EXT1 is differentially regulated in periodontitis ($p = 4,5519 \times 10^{-6}$) (Table 2). Thus, the additional comparison of group means of expression domains in epithelial and stromal compartments was also performed. No significant difference of investigated factors' epithelial expression domains between controls and periodontitis group were found. However, the stromal expression domains of Sdc1 ($p = 1,1033 \times 10^{-6}$), HPSE1 ($p = 0,0023$), EXT1 ($p = 1,2849 \times 10^{-7}$), NDST1 ($p = 0,000105$), and CD45 ($p = 0,003747$) showed significant difference between controls and periodontitis group. The cumulative values of group means for total expression domains and ratios of epithelial and stromal expression domains were plotted on column graphs (Figure 7). Column graphs reveal that the total distribution of Sdcs and HPSE1 is almost equal in periodontitis group compared to controls, but the pattern of this distribution between epithelial and stromal compartments of gingival tissue (except for Sdc2) are quite different (Figure 7A). On the other hand, the distribution of EXTs and NDSTs seems to be more variable, both on the total level and between the epithelial and stromal compartments (Figures 7B,C). Additional aspects of control and periodontitis gingival tissue molecular profiling were revealed by correlating fractional values of investigated factors' stromal expression domains with that of CD45 as dependent variable (Table 3). According to our model, Sdcs differentially correlate with the presence of inflammatory infiltrate. In controls, positive

correlation was found for Sdc2, and negative correlation for Sdc4, whereas no correlation was found for Sdc1. In periodontitis group, both Sdc1 and Sdc2 were positively correlated, but no correlation was found for Sdc4. Interestingly, HPSE1, EXTs, and NDSTs displayed similar correlation pattern in control and periodontitis group – positive correlations were found for EXT1, EXT2 and NDST1. HPSE1 and NDST2 were correlated negatively with CD45.

DISCUSSION

Periodontitis is a common degenerative disease initiated by the bacteria found in subgingival biofilm, which trigger host inflammatory response whose progression is ultimately responsible for the destruction of tooth supporting alveolar bone and soft tissues (periodontal tissue) resulting in tooth loss (Bosshardt and Lang, 2005; Pihlstrom et al., 2005). To date, significant effort has been invested in the research on the involvement of host cells and inflammatory mediators in regulation of inflammatory response in periodontitis (Silva et al., 2015). However, the role of HSPGs (including Sdcs) in pathogenesis of periodontitis is still poorly investigated despite the fact that there are numerous reports, which go almost two decades back, about the critical involvement of these factors in modulation of various aspects of inflammatory response. The data presented in this study clearly indicate that Sdcs display different expression profiles in healthy and diseased periodontal tissue which is in agreement with previous reports (Oksala et al., 1997; Manakil et al., 2001; Kotsovilis et al., 2010). This is further accompanied by the

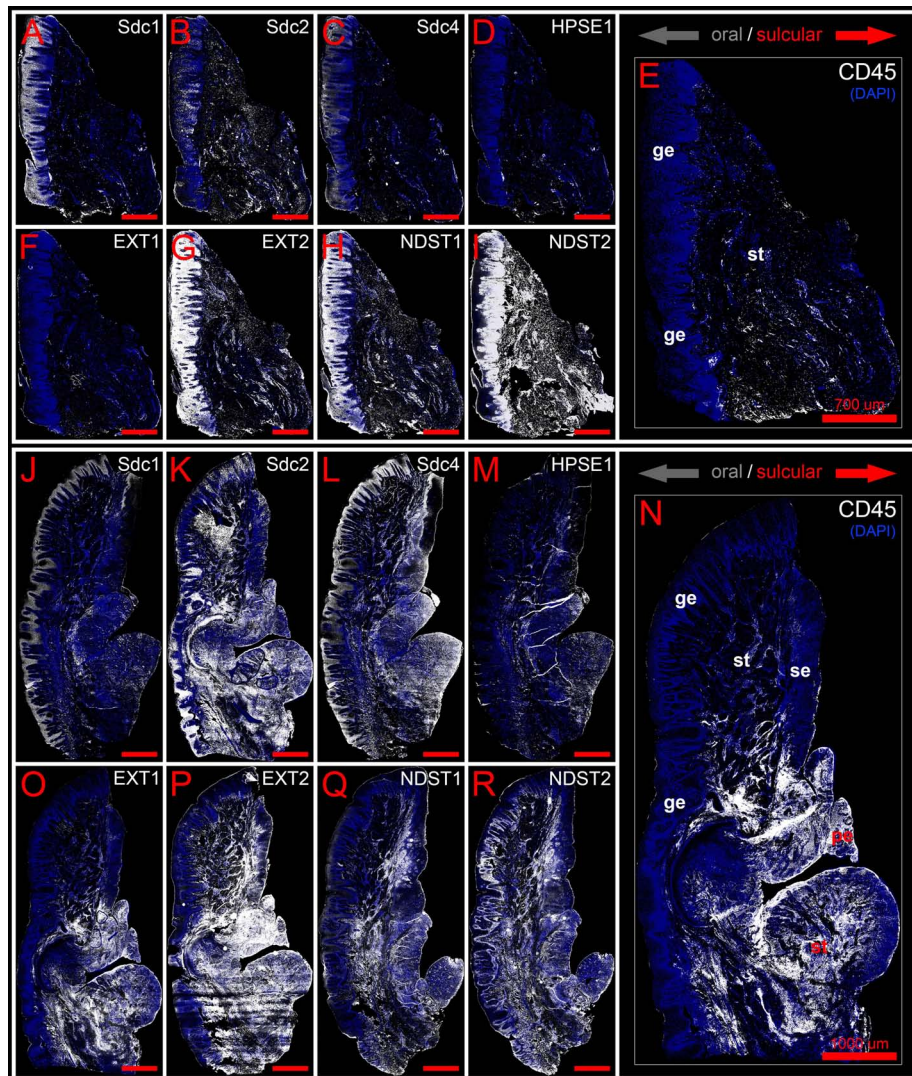


FIGURE 3 | Panoramic IF images of expression of Sdcs, EXTs, NDSTs, and HPSE1 in healthy (control sample DK-NV2-ZK) (A–I) and diseased gingiva (periodontitis sample DK-TM7-CHP) (J–R) compared with expression of inflammatory marker CD45 (E,N). Fluorescence signals are shown in white color. Panoramic IF images are merged with DAPI nuclear stain (pseudo-colored in blue). Notice how Sdcs, HPSE1, and EXT1 display altered patterns of stromal expression in healthy (A–D) and diseased gingiva (J–M), whereas EXT2 and NDSTs display altered patterns of epithelial expression (G–I,P–R). Magnification: (A–I) $\times 10$; scale bars – (A–I) 700 μm ; (J–R) 1000 μm . Designations: gingival epithelium (ge), subepithelial stroma (st), sulcus epithelium (se), pocket epithelium (pe). Oral/vestibular aspect of tissue section (gray arrows); Sulcular/pocket aspect of tissue section (red arrows).

differences in expression profiles of enzymes involved in biosynthesis and modification of HS GAG side chains (EXTs, NDSTs, and HPSE1), which are comparable to a certain degree with those described in other chronic degenerative diseases such as osteoarthritis (Chanalaris et al., 2019). And finally, Sdcs and HS biosynthesis and modifying enzymes could be involved in modulation of inflammatory response in periodontitis, since their expression profiles display different correlation patterns with the presence of inflammatory infiltrate in healthy and diseased periodontal tissue. However, in order to interpret these findings in the context of complex pathogenesis of periodontal disease, the available experimental data about how Sdcs and HS-related enzymes are actually

involved in regulation of inflammatory response, need to be presented in more detail.

Structural Changes in Tissue Microenvironment Might Affect HS GAG-Related and Inherent Properties of Sdcs to Modulate Inflammatory Response in Periodontitis

Sdcs can interact with a wide variety of mediators of inflammation and through these interactions they affect different segments of inflammatory response such as chemokine/cytokine gradient formation, leukocyte recruitment, microbial attachment

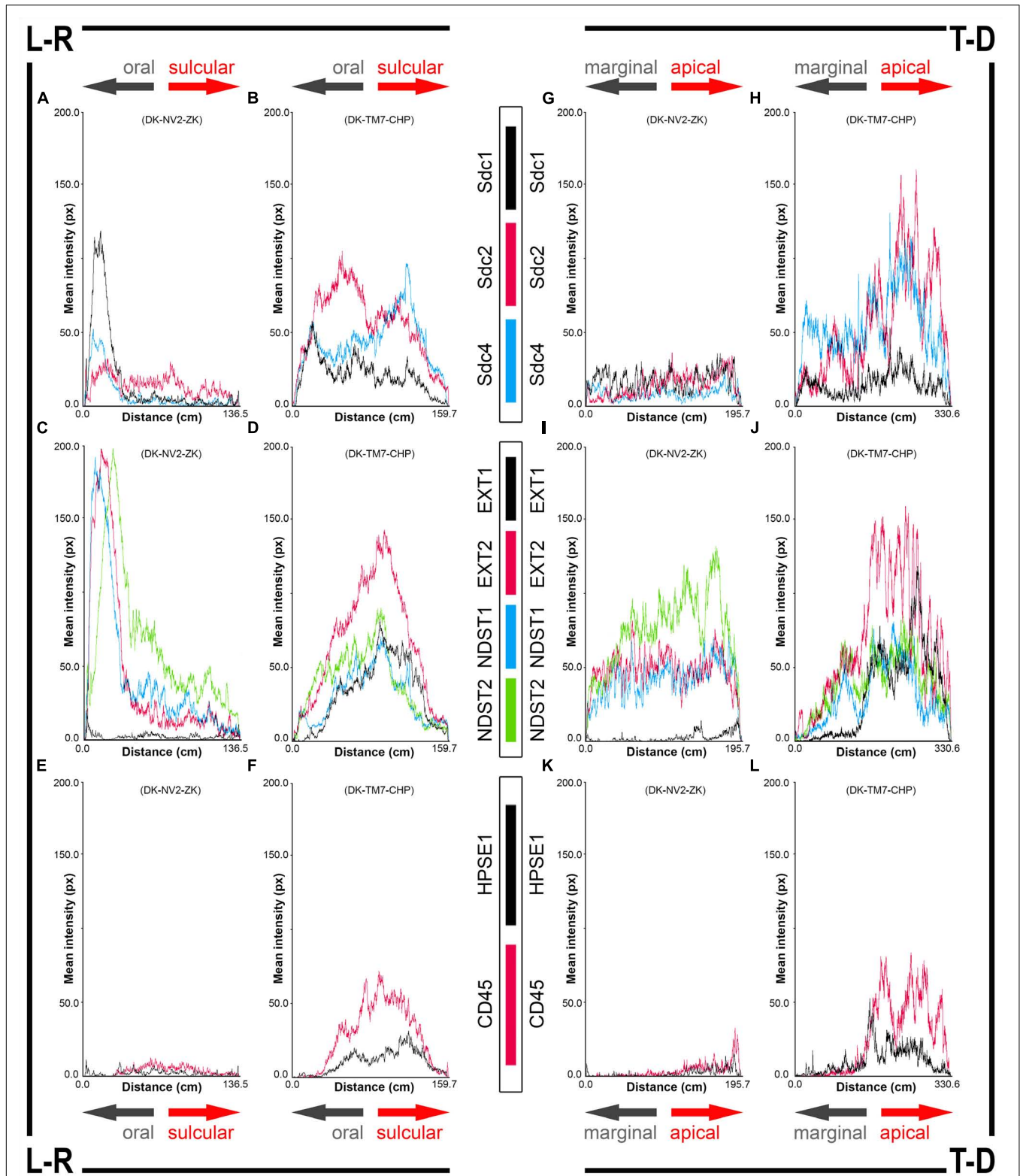


FIGURE 4 | 2D plot profiles of investigated factors in healthy (A,C,E,G,I,K) (sample DK-NV2-ZK) and diseased gingiva (B,D,F,H,J,L) (sample DK-TM7-CHP). Fluorescence signals from panoramic IF images are plotted as curves depicting mean expression intensity from oral toward sulcular aspect (L-R plots) (A–F) and from marginal toward apical aspect (T-D plots) (G–L) of tissue sections. Note that mean expression intensities of most investigated factors in diseased gingiva display positive trend in sulcular and apical direction. (x-axis – scanning distance in cm; y-axis – mean intensity in px; arrows point toward specific aspect of tissue section).

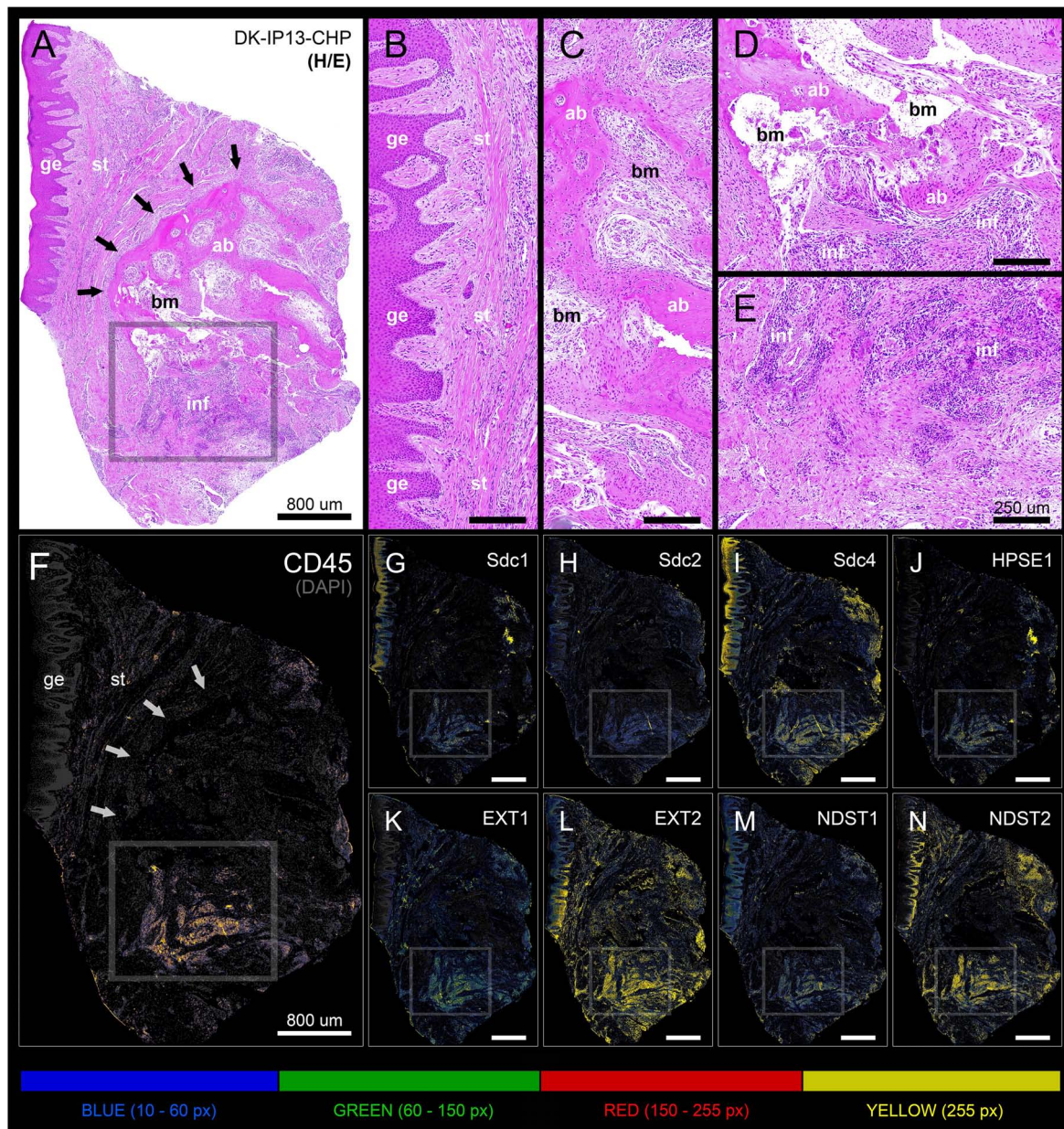


FIGURE 5 | Panoramic H/E image (A) and panoramic multi-color heatmaps (F–N) of diseased gingiva (periodontitis sample DK-IP13-CHP) of expression domains of Sdcs (G–I), HPSE1 (J), EXTs (K,L), NDSTs (M,N) and inflammatory marker CD45 (F) merged with DAPI nuclear staining (dark gray). Inflammatory infiltrate degrading alveolar bone is visible (framed areas) (D,E). Subepithelial stroma between the gingival epithelium and intact lamellae of alveolar bone is mostly devoid of inflammatory infiltrate (B). Bone marrow contains portions of fibrotic tissue (C). All investigated factors are expressed in the area of inflammatory infiltrate (G–N) with variable intensity. Magnification: (A–N) $\times 10$; scale bars – (A,F–N) 800 μm ; (B–E) 250 μm . Designations: gingival epithelium (ge), subepithelial stroma (st), alveolar bone (ab), bone marrow (bm), inflammatory infiltrate (inf). Interface of subepithelial stroma and alveolar bone (black and white thick arrows). Intensity range increments: BLUE (10–60 px), GREEN (60–150 px), RED (150–255 px), YELLOW (255 px).

and entry, as well as the protease balance and activity in matrix remodeling during the resolution of inflammation and tissue healing (Teng et al., 2012; Bonnans et al., 2014). However, their roles in regulation of inflammatory response cannot simply be considered as either pro-inflammatory or anti-inflammatory, because there is ample evidence from experimental studies that individual Sdcs can play both roles depending on the type of

disease-instigating agents and the tissues in which the noxious challenge is exerted. For example, according to experimental models of dermatitis, colitis and myocardial infarction, Sdc1 could be considered as a negative regulator of leukocyte recruitment because *Sdc1*^{-/-} knockout mice exhibit increased neutrophil adhesion and transendothelial migration, despite the fact that Sdcs are closely related to leukocyte recruitment because

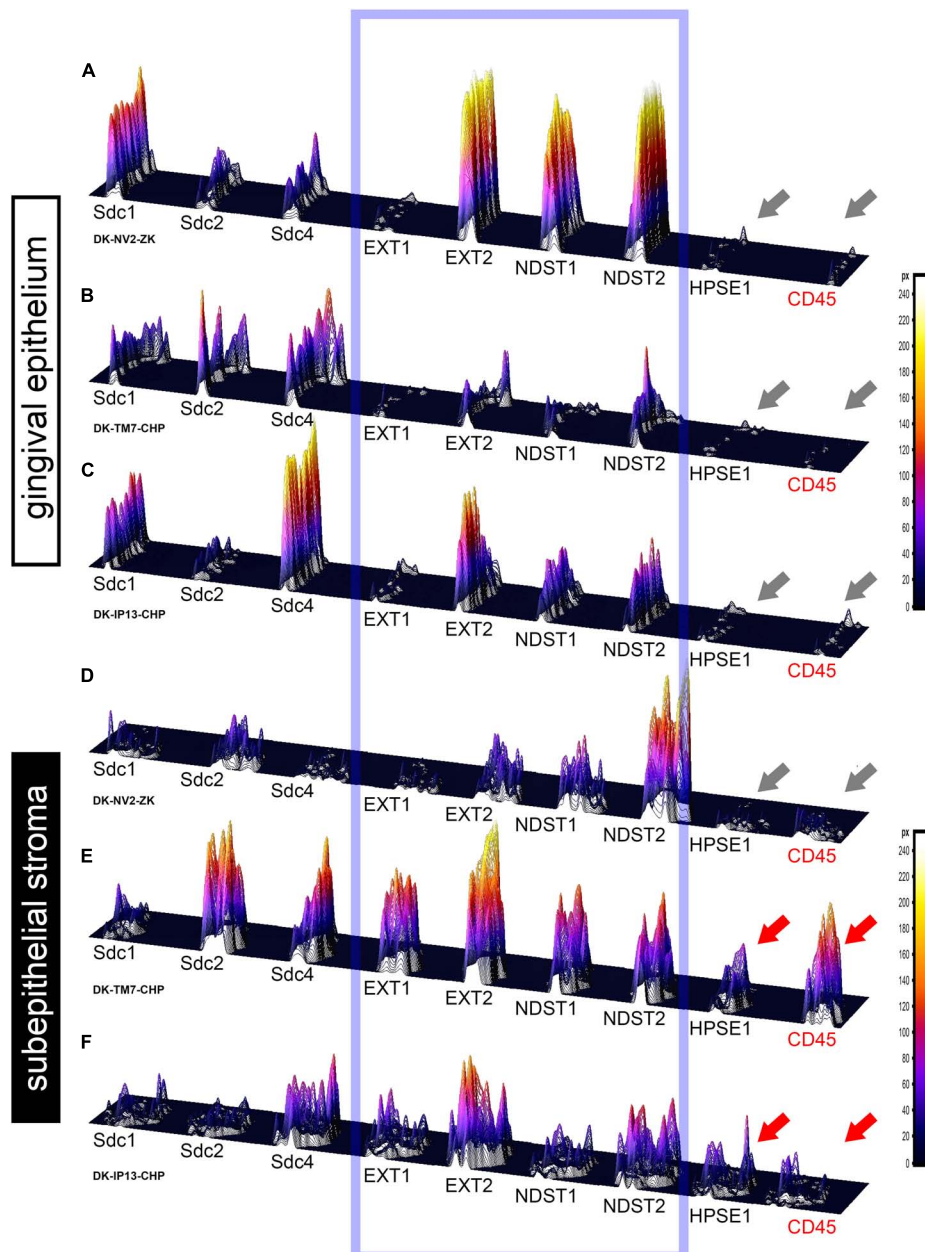


FIGURE 6 | 3D surface plots for multiple co-localization of expression of investigated factors in gingival epithelium (**A–C**) and subepithelial stroma (**D–F**) of healthy (**A, D**) (sample DK-NV2-ZK) and diseased gingiva (**B, C, E, F**) (samples DK-TM7-CHP, DK-IP13-CHP). The variable patterns of combinatorial expression of EXTs and NDSTs (framed area) might imply differences in HS composition between epithelial and stromal compartments within and between samples of healthy and diseased gingiva. Combinatorial expression of HPSE1 and CD45 (gray and red arrows) varies in healthy and diseased gingiva, as well as in diseased gingiva samples with diffuse (**E**) and localized (**F**) inflammatory infiltrate, corresponding to the severity of inflammation. (Far right – color-graded intensity scales in px values).

of their ability to bind chemokines and form chemokine gradients on endothelial surface of blood vessels (for that matter, the most well-studied connections are those between endothelial Sdc1, Sdc2, and CXC chemokine IL-8) (Mahtouk et al., 2007; Vanhoutte et al., 2007; Beauvais et al., 2009; Floer et al., 2010; Jung et al., 2016). Furthermore, the presence of Sdcs as intact cell surface HSPGs or soluble ECM effectors due to shedding of Sdcs core protein ectodomains can diversely affect

the formation of gradients of inflammatory mediators, and thus the confinement, progression or attenuation of inflammatory response as nicely demonstrated on experimental knockout mouse models of allergic lung disease, bleomycin-induced acute lung injury and Gram-positive toxic shock (Li et al., 2002; Xu et al., 2005; Hayashida et al., 2009). Cell surface or shed Sdcs can also promote the pathogenesis of infectious diseases on multiple levels from facilitating microbial attachment and entry

TABLE 2 | ANOVA analysis of total, epithelial, and stromal expression domains of investigated factors in control and periodontitis group.

Factor	Tissue compartment	F-value	P-value
Sdc1	TOTAL	2,931137	0,087518
	EPITHELIUM	0,002173	0,962838
	STROMA***	24,348604	1,103 × 10⁻⁶
Sdc2	TOTAL	0,813112	0,367644
	EPITHELIUM	0,183157	0,668861
	STROMA	0,000684	0,979139
Sdc4	TOTAL	0,148252	0,700377
	EPITHELIUM	0,493848	0,482549
	STROMA	2,705549	0,100640
HPSE1	TOTAL	1,049814	0,306055
	EPITHELIUM*	4,965093	0,026316
	STROMA***	9,320604	0,002389
EXT1	TOTAL***	21,496702	4,551 × 10⁻⁶
	EPITHELIUM	2,476544	0,116201
	STROMA***	28,727777	1,284 × 10⁻⁷
EXT2	TOTAL	0,098317	0,753991
	EPITHELIUM	0,284528	0,593990
	STROMA	2,461318	0,117326
NDST1	TOTAL	1,031306	0,310353
	EPITHELIUM	0,315713	0,574451
	STROMA***	15,285767	0,000105
NDST2	TOTAL	0,247242	0,619246
	EPITHELIUM	1,896305	0,169121
	STROMA	1,445718	0,229796
CD45	TOTAL*	4,461122	0,035180
	STROMA***	8,483681	0,003747

Level of significance was set at $\alpha = 0,01$ (** $p < 0,01$; $F_{crit} = 6,686878$); (*border values, level of significance $\alpha = 0,05$).

into host cells (cell surface Sdcs) to disruption of host immune response (shed Sdcs) as reported in studies on *Herpes simplex virus* or *Pseudomonas aeruginosa* infections, respectively (Bucior et al., 2010; Bacsa et al., 2011). While most of the described roles of Sdcs in regulation of inflammatory response can be strictly associated with their ability to carry HS GAG chains, it is possible that, to a certain degree, those roles might also be related to specific properties of individual Sdcs core proteins. Namely, the underlying molecular mechanisms of functional redundancy between Sdc1 and Sdc4 during prenatal development are unclear. Single *Sdc1*^{-/-} or *Sdc4*^{-/-} knockout animals develop normally, but as adults display similar phenotypes of impaired host immune response when challenged in inflammatory or wound-healing models (Stepp et al., 2015; Kero et al., 2018). Expression of Sdcs is reported to be very responsive to structural changes of tissue. However, it seems that during the inflammatory response these changes do not only affect the expression of Sdcs, but might also serve to unlock otherwise hidden inherent properties of individual Sdcs. The similar effect of tissue dynamics turning structural proteins into effective mediators of inflammatory response in chronic diseases has been described for many HSPGs and other ECM-related proteins (Rozario and DeSimone, 2010; Afratis et al., 2017). Accordingly, different

expression profiles of Sdcs in healthy and diseased periodontal tissue reported here and in previous studies, might imply that perturbations in natural HS GAG-carrier capacity (and bio-availability of HS GAGS) does not need to be the only mechanism how Sdcs could modulate inflammatory response in periodontitis.

Differential Expression of HS Biosynthesis and Degradation Enzymes Could Modulate the Inflammatory Response in Healthy and Diseased Periodontal Tissue

Since most of the roles of Sdcs in inflammation can be related to their ability to carry HS GAG chains which determine the HSPGs affinity for various ligands, it is reasonable to conclude that the course of inflammatory response should greatly depend on the biochemical properties of HS. This is corroborated by several studies on experimental animal models of allergic lung disease and diabetic nephropathy where the targeted endothelial ablation of genes encoding enzymes involved in HS biosynthesis resulted in both attenuation or severe disruption of inflammatory response (Ge et al., 2018; Talsma et al., 2018). HS is a linear polysaccharide chain comprised of repeating disaccharide units of glucosamine (GlcNAc) and glucuronic acid (GlcA) modified in a step-wise manner by addition of sulfate groups (NDSTs, sulfotransferases) during its biosynthesis, or post-biosynthetically by removal of sulfate groups at specific residues (desulfatases) and cleavage on small oligosaccharide fragments (HPSE1) (Zhang et al., 2016). While the total capacity of HS for ligands may depend upon its chain length (determined by EXTs polymerases), the affinity of HS is greatly influenced by the pattern and sequence of initial sulfation modifications (NDSTs). According to several reports, the roles of EXTs and NDSTs in the initial steps of HS biosynthesis are so intricately related that the variations in both HS chain length and structure must be viewed through prism of combinatorial actions of both EXTs and NDSTs (Esko and Selleck, 2002; Presto et al., 2008; Dagalv et al., 2015; Deligny et al., 2016). For example, altered activity of individual EXTs can also affect the pattern of HS sulfation modifications, whereas the altered activity of individual NDSTs can in turn affect the chain length and quantity of HS. Based on the data presented here, it is not possible to draw any definitive conclusions about the changes of quantity or composition of HS in healthy and diseased periodontal tissue. However, the differential expression profiles of EXT1, NDST1 and HPSE1 do imply that certain perturbations in stromal HS content and composition might occur in periodontitis and might be responsible for dysregulation of inflammatory response. Similar correlation profiles of EXTs and NDSTs with the presence of inflammatory infiltrate in healthy and diseased periodontal tissues are also intriguing, but more data about expression of other enzymes related to HS biosynthesis and modification are still needed in order to fully assess the potential significance of this finding. In spite of the statistically significant difference of expression of HPSE1 between healthy and diseased gingiva, negative correlation of expression of HPSE1 with the presence of inflammatory infiltrate

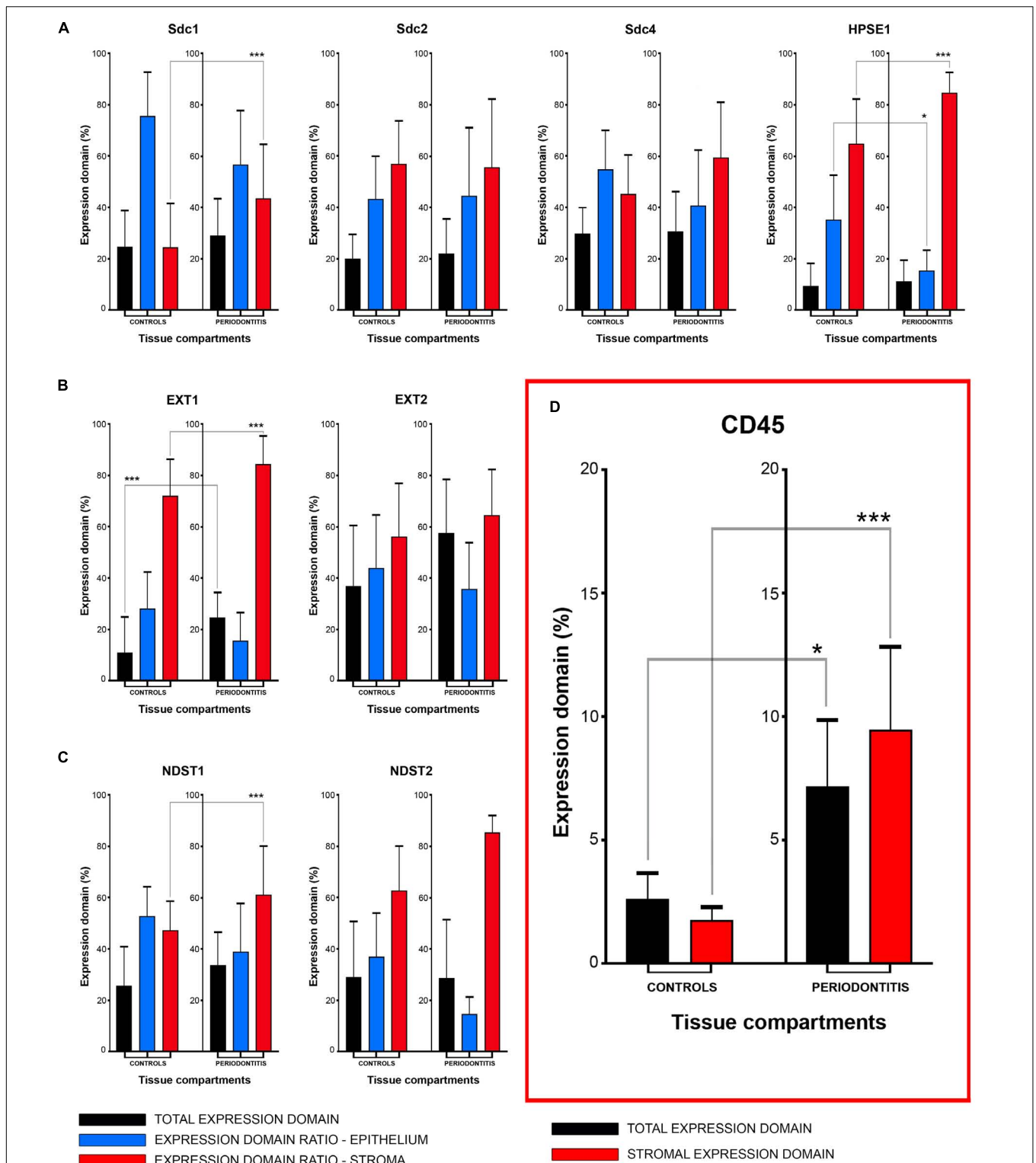


FIGURE 7 | Mean group values of total expression domains (expressed in percentages as fractions of total section area) compared with epithelial and stromal expression domain ratios (expressed in percentages fractions of total expression domain) of investigated factors in control and periodontitis group (A–C). The total availability of Sdcs and HPSE1 seems to be on comparable levels in controls and periodontitis, but their distribution (apart from Sdc2) in epithelial and stromal compartments of gingival tissue differs between two groups (A). EXTs and NDST1 display similar pattern of changes in epithelial/stromal expression domain ratios in favor of stromal compartment (B,C), which corresponds with increased presence of inflammatory infiltrate in periodontitis group (***p* = 0,003747) (D). Level of significance was set at $\alpha = 0,01$ (***p* < 0,01; *border values $\alpha = 0,05$).

TABLE 3 | Correlation of stromal expression of investigated factors with the stromal expression of inflammatory marker CD45 (dependent variable) in control and periodontitis group by multiple linear regression.

Controls		Adj. R Square = 0,999970		Significance ($\alpha = 0,01$)	
Factor	Coefficients	Std. Error	P-value	Correlation	Factor
CD45	0,001153	3,4873E-05	8,69889 × 10⁻⁹¹	y-intercept	CD45
Sdc1	0,001101	0,000648	0,090655	/	Sdc1
Sdc2	0,055181	0,011347	2,10704 × 10⁻⁶	+	Sdc2
Sdc4	-0,034054	0,009169	0,000254	-	Sdc4
HPSE1*	-0,017389	0,00798	0,03030448*	-	HPSE1
EXT1	0,040905	0,004848	3,24401 × 10⁻¹⁵	+	EXT1
EXT2	0,088969	0,004871	4,18827 × 10⁻⁴⁷	+	EXT2
NDST1	0,072287	0,006357	3,38384 × 10⁻²⁴	+	NDST1
NDST2	-0,124233	0,008917	1,25435 × 10⁻³²	-	NDST2

Periodontitis		Adj. R Square = 0,999842		Significance ($\alpha = 0,01$)	
Factor	Coefficients	Std. Error	P-value	Correlation	Factor
CD45	0,007491	0,000401	2,03439 × 10⁻⁴⁸	y-intercept	CD45
Sdc1	0,223765	0,050875	1,64866 × 10⁻⁵	+	Sdc1
Sdc2	0,038956	0,014481	0,007649	+	Sdc2
Sdc4	-0,304709	0,196676	0,122646	/	Sdc4
HPSE1*	-0,546769	0,267466	0,042033*	-	HPSE1*
EXT1*	0,081325	0,035296	0,022084*	+	EXT1*
EXT2	0,301984	0,017352	2,94539 × 10⁻⁴⁴	+	EXT2
NDST1	0,295806	0,116812	0,011977	+	NDST1*
NDST2	-0,319424	0,082515	0,000140	-	NDST2

Level of significance was set at $\alpha = 0,01$ (***) ($p < 0,01$); (+ positive correlation, - negative correlation, / no correlation); (*border values, level of significance $\alpha = 0,05$).

in gingiva from both test and periodontitis group was a bit surprising. The increased activity of HPSE1 is considered as a hallmark of inflammatory sites in various tissues designating HPSE1 as a pro-inflammatory marker (Li and Vlodaysky, 2009). However, there are reports from studies on experimental animals that HPSE1 might also act as an anti-inflammatory agent in certain settings (Sanderson et al., 2017). Additionally, changes in expression of HPSE1 should not be definitively associated with the changes in HPSE1 enzymatic activity, because the commercial antibodies against HPSE1 do not differentiate between the inactive and active forms of HPSE1 (Kero et al., 2018). With regard to that, IHC profiling of gingival tissue with antibodies against specific epitopes of HS GAG side chains might prove useful.

Another difficulty about the analysis of expression profiles of HSPGs and HS-related enzymes is that these proteins are ubiquitously expressed in various tissues and as such require whole tissue section visualization, which fortunately today can be performed at high resolution. However, in order to fully utilize that, the quantification of IHC staining must also be performed at whole tissue section level, but in such a manner that the very shapes of tissue sections do not pose serious bias for subsequent statistical analysis. Here, this was achieved with regard to two attributes of IHC staining – the total area covered by staining (expression domain) and the distribution of intensity on a fixed ordinal scale (px values). The quantification of IHC staining

gradients (i.e., the quantification of spatial distribution of staining) on a whole tissue section level still needs to be improved in order to obtain more detailed description of microenvironment in which the various cellular processes take place. This is of paramount importance, because the regulation of inflammatory response in periodontitis might also be driven by structural changes of microenvironment, whose molecular features are still insufficiently explored. Additional reason for continuing this line of research is provided by the experimental studies on application of HS-mimetics as potential therapeutic agents for regenerative treatment of periodontitis (Lallam-Laroye et al., 2006; Barritault et al., 2017).

CONCLUSION

Of all investigated factors, the expression domains of Sdc1, HPSE1, EXT1, and NDST1 in gingival tissue displayed statistically significant differences between control and periodontitis group. The expressions of Sdcs in gingival tissue correlated differentially with the presence of inflammatory infiltrate in control and periodontitis group – in control group, no correlation was found for Sdc1, whereas Sdc2 correlated positively and Sdc4 correlated negatively; in periodontitis group both Sdc1 and Sdc2 correlated positively with the presence of inflammatory infiltrate, and no correlation was

found for Sdc4. The expressions of HS biosynthesis (EXT1, EXT2, NDST1, and NDST2) and degradation enzymes (HPSE1) display similar correlation patterns with the presence of inflammatory infiltrate in gingival tissue from control and periodontitis group – EXT1, EXT2, and NDST1 correlate positively, whereas negative correlation was found for NDST2 and HPSE1. The analyzed histomorphometric parameters of gingival tissues were mostly found to be well-balanced between the control and periodontitis group with the exception of epithelial-stromal cellularity ratio. Therefore, it might be suggested that the homeostasis in diseased gingival tissue is maintained to a significant degree, but the underlying compensatory mechanisms differ from those in healthy gingiva and could be related to the variable presence of inflammatory infiltrate and changes in expression profiles of Sdcs and HS biosynthesis and degradation enzymes. The findings presented here might also be viewed with regard to demographic risk factors for periodontitis such as age and smoking (Calsina et al., 2002; Helal et al., 2019). Namely, participants from the periodontitis group had higher mean age and were predominantly smokers in contrast to the participants from the control group (Table 1). Aging and smoking can affect immunity on multiple levels, but how these risk factors are exactly related to changes of HSPGs and HSPG-related factors' molecular profiles during the inflammatory response in periodontitis still needs to be determined and, due to type of data and methods of analysis applied here, goes beyond the scope of this study.

DATA AVAILABILITY STATEMENT

All datasets generated for this study are included in the manuscript/supplementary files.

ETHICS STATEMENT

Tissue procurement and processing were approved by the Ethical and Drug Committee of School of Medicine (University of Split) (Class: 003-08/17-03/0001, No: 2181-198-03-04-17-0043) and Ethical and Drug Committee of School of Dental Medicine (University of Zagreb) (No: 05-PA-15-6/2017) in accordance with Helsinki Declaration (Williams, 2008).

AUTHOR CONTRIBUTIONS

RDu assisted DK in the study design, performed IF staining, H/E and panoramic IF image acquisition and statistical

analysis of the data, reviewed literature and wrote sections of the manuscript with MR (Introduction, Materials and Methods, Results, and Discussion), proofread the manuscript. MR assisted DK in the study design, devised protocol for patient screening and recruitment, collected tissue samples, participated in samples processing, interpreted data (clinical parameters and H/E staining), reviewed literature, wrote sections of the manuscript with RDu (Introduction, Materials and Methods, Results, and Discussion), proofread the manuscript. IP collected tissue samples, interpreted data (clinical parameters), wrote parts of the manuscript (Introduction, Materials and Methods, and Discussion), reviewed the literature, proofread the manuscript. NV participated in patient screening and recruitment, assisted in IF staining, reviewed part of the literature and proofread the manuscript. RDr participated in patient screening and recruitment, assisted in IF staining, reviewed part of the literature, and proofread the manuscript. KV supervised H/E and IF staining, reviewed part of the literature, interpreted data (H/E and IF staining), and proofread the manuscript. MS-B interpreted data (H/E and IF staining) and proofread the manuscript. DK designed the study, devised methods for image acquisition (H/E and IF panoramic images) and statistical analysis, performed selection of primary antibodies, provided theoretical background, interpreted data, reviewed literature, wrote and revised the manuscript.

FUNDING

This work was supported by the Ministry of Science, Education, and Sports of the Republic of Croatia.

ACKNOWLEDGMENTS

The authors wish to thank Prof. Katarina Vilovic Ph.D., Marina Degoricija Ph.D., and Benjamin Benzon Ph.D. for valuable insights and advice with regard to patho-histological profiling of tissue samples and statistical analysis of data. Special thanks to Branka Bernard Ph.D. and team from Mediterranean Institute for Life Sciences for kindly introducing us to brand new Zeiss microscope. The authors also wish to thank Mrs. Marica Maretic and Mrs. Asja Miletic for expert technical assistance with preparation of tissue samples and optimization of protocols for immunofluorescence staining.

REFERENCES

- Afratis, N. A., Nikitovic, D., Mulhaupt, H. A., Theocharis, A. D., Couchman, J. R., and Karamanos, N. K. (2017). Syndecans - key regulators of cell signaling and biological functions. *FEBS J.* 284, 27–41. doi: 10.1111/febs.13940
- Bacsa, S., Karasneh, G., Dosa, S., Liu, J., Valyi-Nagy, T., and Shukla, D. (2011). Syndecan-1 and syndecan-2 play key roles in herpes simplex virus type-1 infection. *J. Gen. Virol.* 92, 733–743. doi: 10.1099/vir.0.027052-0
- Barritault, D., Gilbert-Sirieix, M., Rice, K. L., Sineriz, F., Papy-Garcia, D., Baudouin, C., et al. (2017). RGTA((R)) or ReGeneraTing Agents mimic heparan sulfate in regenerative medicine: from concept to curing patients. *Glycoconj J.* 34, 325–338. doi: 10.1007/s10719-016-9744-5
- Beauvais, D. M., Ell, B. J., Mcwhorter, A. R., and Rapraeger, A. C. (2009). Syndecan-1 regulates alphavbeta3 and alphavbeta5 integrin activation during angiogenesis and is blocked by synstatin, a novel peptide inhibitor. *J. Exp. Med.* 206, 691–705. doi: 10.1084/jem.20081278

- Bernfield, M., Kokenyesi, R., Kato, M., Hinkes, M. T., Spring, J., Gallo, R. L., et al. (1992). Biology of the syndecans: a family of transmembrane heparan sulfate proteoglycans. *Annu. Rev. Cell Biol.* 8, 365–393. doi: 10.1146/annurev.cellbio.8.1.365
- Bonnans, C., Chou, J., and Werb, Z. (2014). Remodelling the extracellular matrix in development and disease. *Nat. Rev. Mol. Cell Biol.* 15, 786–801. doi: 10.1038/nrm3904
- Bosshardt, D. D., and Lang, N. P. (2005). The junctional epithelium: from health to disease. *J. Dent. Res.* 84, 9–20. doi: 10.1177/154405910508400102
- Bucior, I., Mostov, K., and Engel, J. N. (2010). *Pseudomonas aeruginosa*-mediated damage requires distinct receptors at the apical and basolateral surfaces of the polarized epithelium. *Infect. Immun.* 78, 939–953. doi: 10.1128/IAI.01215-09
- Calsina, G., Ramon, J. M., and Echeverria, J. J. (2002). Effects of smoking on periodontal tissues. *J. Clin. Periodontol.* 29, 771–776. doi: 10.1034/j.1600-051x.2002.290815.x
- Chanalaris, A., Clarke, H., Guimond, S. E., Vincent, T. L., Turnbull, J. E., and Troeberg, L. (2019). Heparan sulfate proteoglycan synthesis is dysregulated in human osteoarthritic cartilage. *Am. J. Pathol.* 189, 632–647. doi: 10.1016/j.ajpath.2018.11.011
- Cubela, M., Soljic, V., Kero, D., Vukojevic, K., Govorko, D. K., and Saraga-Babic, M. (2016). Comparison of proliferation, apoptosis and expression of syndecan-1 and alpha-SMA in edentulous ridge oral mucosa of successful and early failed submerged dental implants—An immunohistochemical study. *Arch. Oral Biol.* 66, 155–164. doi: 10.1016/j.archoralbio.2016.02.017
- Dagalv, A., Lundequist, A., Filipek-Gorniok, B., Dierker, T., Eriksson, I., and Kjellen, L. (2015). Heparan sulfate structure: methods to study N-sulfation and NDST action. *Methods Mol. Biol.* 1229, 189–200. doi: 10.1007/978-1-4939-1714-3_17
- Deligny, A., Dierker, T., Dagalv, A., Lundequist, A., Eriksson, I., Nairn, A. V., et al. (2016). NDST2 (N-Deacetylase/N-Sulfotransferase-2) enzyme regulates heparan sulfate chain length. *J. Biol. Chem.* 291, 18600–18607. doi: 10.1074/jbc.M116.744433
- Esko, J. D., and Selleck, S. B. (2002). Order out of chaos: assembly of ligand binding sites in heparan sulfate. *Annu. Rev. Biochem.* 71, 435–471. doi: 10.1146/annurev.biochem.71.110601.135458
- Filatova, A., Pagella, P., and Mitsiadis, T. A. (2014). Distribution of syndecan-1 protein in developing mouse teeth. *Front. Physiol.* 5:518. doi: 10.3389/fphys.2014.00518
- Floer, M., Gotte, M., Wild, M. K., Heidemann, J., Gassar, E. S., Domschke, W., et al. (2010). Enoxaparin improves the course of dextran sodium sulfate-induced colitis in syndecan-1-deficient mice. *Am. J. Pathol.* 176, 146–157. doi: 10.2353/ajpath.2010.080639
- Ge, X. N., Bastan, I., Ha, S. G., Greenberg, Y. G., Esko, J. D., Rao, S. P., et al. (2018). Regulation of eosinophil recruitment and allergic airway inflammation by heparan sulfate proteoglycan (HSPG) modifying enzymes. *Exp. Lung Res.* 44, 98–112. doi: 10.1080/01902148.2018.1451574
- Gotte, M. (2003). Syndecans in inflammation. *FASEB J.* 17, 575–591. doi: 10.1096/fj.02-0739rev
- Gutter-Kapon, L., Alishekevitz, D., Shaked, Y., Li, J. P., Aronheim, A., Ilan, N., et al. (2016). Heparanase is required for activation and function of macrophages. *Proc. Natl. Acad. Sci. U.S.A.* 113, E7808–E7817.
- Hayashida, A., Bartlett, A. H., Foster, T. J., and Park, P. W. (2009). Staphylococcus aureus beta-toxin induces lung injury through syndecan-1. *Am. J. Pathol.* 174, 509–518. doi: 10.2353/ajpath.2009.080394
- Helal, O., Gostemeyer, G., Krois, J., Fawzy El Sayed, K., Graetz, C., and Schwendicke, F. (2019). Predictors for tooth loss in periodontitis patients: systematic review and meta-analysis. *J. Clin. Periodontol.* 46, 699–712. doi: 10.1111/jcpe.13118
- Hernandez, M., Dutzan, N., Garcia-Sesnich, J., Abusleme, L., Dezerega, A., Silva, N., et al. (2011). Host-pathogen interactions in progressive chronic periodontitis. *J. Dent. Res.* 90, 1164–1170. doi: 10.1177/0022034511401405
- Jung, O., Trapp-Stamborski, V., Purushothaman, A., Jin, H., Wang, H., Sanderson, R. D., et al. (2016). Heparanase-induced shedding of syndecan-1/CD138 in myeloma and endothelial cells activates VEGFR2 and an invasive phenotype: prevention by novel synstatins. *Oncogenesis* 5:e202. doi: 10.1038/oncsis.2016.5
- Kero, D., Bilandzija, T. S., Arapovic, L. L., Vukojevic, K., and Saraga-Babic, M. (2018). Syndecans and enzymes involved in heparan sulfate biosynthesis and degradation are differentially expressed during human odontogenesis. *Front. Physiol.* 9:732. doi: 10.3389/fphys.2018.00732
- Kero, D., Cigic, L., Medvedec Mikic, I., Galic, T., Cubela, M., Vukojevic, K., et al. (2016). Involvement of IGF-2, IGF-1R, IGF-2R and PTEN in development of human tooth germ - an immunohistochemical study. *Organogenesis* 12, 152–167. doi: 10.1080/15476278.2016.1197460
- Kero, D., Kalibovic Govorko, D., Medvedec Mikic, I., Vukojevic, K., Cigic, L., and Saraga-Babic, M. (2015). Analysis of expression patterns of IGF-1, caspase-3 and HSP-70 in developing human tooth germs. *Arch. Oral Biol.* 60, 1533–1544. doi: 10.1016/j.archoralbio.2015.07.004
- Kero, D., Vukojevic, K., Stazic, P., Sundov, D., Mardesic Brakus, S., and Saraga-Babic, M. (2017). Regulation of proliferation in developing human tooth germs by MSX homeodomain proteins and cyclin-dependent kinase inhibitor p19(INK4d). *Organogenesis* 13, 141–155. doi: 10.1080/15476278.2017.1358337
- Kotsovilis, S., Tseleni-Balafouta, S., Charonis, A., Fourmousis, I., Nikolidakis, D., and Vrotsos, J. A. (2010). Syndecan-1 immunohistochemical expression in gingival tissues of chronic periodontitis patients correlated with various putative factors. *J. Periodontol. Res.* 45, 520–531. doi: 10.1111/j.1600-0765.2009.01267.x
- Lallam-Laroye, C., Escartin, Q., Zlowodzki, A. S., Barrault, D., Caruelle, J. P., Baroukh, B., et al. (2006). Periodontitis destructions are restored by synthetic glycosaminoglycan mimetic. *J. Biomed. Mater. Res. A* 79, 675–683. doi: 10.1002/jbm.a.30880
- Li, J. P., and Vlodavsky, I. (2009). Heparin, heparan sulfate and heparanase in inflammatory reactions. *Thromb. Haemost.* 102, 823–828. doi: 10.1160/TH09-02-0091
- Li, Q., Park, P. W., Wilson, C. L., and Parks, W. C. (2002). Matrilysin shedding of syndecan-1 regulates chemokine mobilization and transepithelial efflux of neutrophils in acute lung injury. *Cell* 111, 635–646. doi: 10.1016/s0092-8674(02)01079-6
- Mahtouk, K., Hose, D., Raynaud, P., Hundemer, M., Jourdan, M., Jourdan, E., et al. (2007). Heparanase influences expression and shedding of syndecan-1, and its expression by the bone marrow environment is a bad prognostic factor in multiple myeloma. *Blood* 109, 4914–4923. doi: 10.1182/blood-2006-08-043232
- Manakil, J. F., Sugerman, P. B., Li, H., Seymour, G. J., and Bartold, P. M. (2001). Cell-surface proteoglycan expression by lymphocytes from peripheral blood and gingiva in health and periodontal disease. *J. Dent. Res.* 80, 1704–1710. doi: 10.1177/00220345010800080501
- Mulhaupt, H. A., Yoneda, A., Whiteford, J. R., Oh, E. S., Lee, W., and Couchman, J. R. (2009). Syndecan signaling: when, where and why? *J. Physiol. Pharmacol.* 60(Suppl. 4), 31–38.
- Oksala, O., Haapasalmi, K., Hakkinen, L., Uitto, V. J., and Larjava, H. (1997). Expression of heparan sulphate and small dermatan/chondroitin sulphate proteoglycans in chronically inflamed human periodontium. *J. Dent. Res.* 76, 1250–1259. doi: 10.1177/00220345970760060401
- Papapanou, P. N., Sanz, M., Buduneli, N., Dietrich, T., Feres, M., Fine, D. H., et al. (2018). Periodontitis: consensus report of workgroup 2 of the 2017 world workshop on the classification of periodontal and peri-implant diseases and conditions. *J. Periodontol.* 89(Suppl. 1), S173–S182.
- Pihlstrom, B. L., Michalowicz, B. S., and Johnson, N. W. (2005). Periodontal diseases. *Lancet* 366, 1809–1820.
- Poon, I. K., Goodall, K. J., Phipps, S., Chow, J. D., Pagler, E. B., Andrews, D. M., et al. (2014). Mice deficient in heparanase exhibit impaired dendritic cell migration and reduced airway inflammation. *Eur. J. Immunol.* 44, 1016–1030. doi: 10.1002/eji.201343645
- Presto, J., Thuveson, M., Carlsson, P., Busse, M., Wilen, M., Eriksson, I., et al. (2008). Heparan sulfate biosynthesis enzymes EXT1 and EXT2 affect NDST1 expression and heparan sulfate sulfation. *Proc. Natl. Acad. Sci. U.S.A.* 105, 4751–4756. doi: 10.1073/pnas.0705807105
- Roper, J. A., Williamson, R. C., and Bass, M. D. (2012). Syndecan and integrin interactomes: large complexes in small spaces. *Curr. Opin. Struct. Biol.* 22, 583–590. doi: 10.1016/j.sbi.2012.07.003
- Rozario, T., and DeSimone, D. W. (2010). The extracellular matrix in development and morphogenesis: a dynamic view. *Dev. Biol.* 341, 126–140. doi: 10.1016/j.ydbio.2009.10.026
- Sanderson, R. D., Elkin, M., Rapraeger, A. C., Ilan, N., and Vlodavsky, I. (2017). Heparanase regulation of cancer, autophagy and inflammation: new

- mechanisms and targets for therapy. *FEBS J.* 284, 42–55. doi: 10.1111/febs.13932
- Silva, N., Abusleme, L., Bravo, D., Dutzan, N., Garcia-Sesnich, J., Vernal, R., et al. (2015). Host response mechanisms in periodontal diseases. *J. Appl. Oral Sci.* 23, 329–355. doi: 10.1590/1678-775720140259
- Stapp, M. A., Pal-Ghosh, S., Tadvalkar, G., and Pajooesh-Ganji, A. (2015). Syndecan-1 and its expanding list of contacts. *Adv. Wound Care* 4, 235–249. doi: 10.1089/wound.2014.0555
- Stoler-Barak, L., Mousson, C., Shezen, E., Hatzav, M., Sixt, M., and Alon, R. (2014). Blood vessels pattern heparan sulfate gradients between their apical and basolateral aspects. *PLoS One* 9:e85699. doi: 10.1371/journal.pone.0085699
- Talsma, D. T., Katta, K., Ettema, M. A. B., Kel, B., Kusche-Gullberg, M., Daha, M. R., et al. (2018). Endothelial heparan sulfate deficiency reduces inflammation and fibrosis in murine diabetic nephropathy. *Lab Invest.* 98, 427–438. doi: 10.1038/s41374-017-0015-2
- Taylor, K. R., and Gallo, R. L. (2006). Glycosaminoglycans and their proteoglycans: host-associated molecular patterns for initiation and modulation of inflammation. *FASEB J.* 20, 9–22. doi: 10.1096/fj.05-4682rev
- Teng, Y. H., Aquino, R. S., and Park, P. W. (2012). Molecular functions of syndecan-1 in disease. *Matrix Biol.* 31, 3–16. doi: 10.1016/j.matbio.2011.10.001
- Vanhoutte, D., Schellings, M. W., Gotte, M., Swinnen, M., Herias, V., Wild, M. K., et al. (2007). Increased expression of syndecan-1 protects against cardiac dilatation and dysfunction after myocardial infarction. *Circulation* 115, 475–482. doi: 10.1161/circulationaha.106.644609
- Vukojevic, K., Kero, D., Novakovic, J., Kalibovic Govorko, D., and Saraga-Babic, M. (2012). Cell proliferation and apoptosis in the fusion of human primary and secondary palates. *Eur. J. Oral Sci.* 120, 283–291. doi: 10.1111/j.1600-0722.2012.00967.x
- Williams, J. R. (2008). The declaration of helsinki and public health. *Bull. World Health Organ.* 86, 650–652.
- Wu, Y. H., Kuraji, R., Taya, Y., Ito, H., and Numabe, Y. (2018). Effects of theaflavins on tissue inflammation and bone resorption on experimental periodontitis in rats. *J. Periodontol. Res.* 53, 1009–1019. doi: 10.1111/jre.12600
- Xu, J., Park, P. W., Kheradmand, F., and Corry, D. B. (2005). Endogenous attenuation of allergic lung inflammation by syndecan-1. *J. Immunol.* 174, 5758–5765. doi: 10.4049/jimmunol.174.9.5758
- Zhang, X., Wang, F., and Sheng, J. (2016). “Coding” and “Decoding”: hypothesis for the regulatory mechanism involved in heparan sulfate biosynthesis. *Carbohydr. Res.* 428, 1–7. doi: 10.1016/j.carres.2016.04.002
- Conflict of Interest:** The authors declare that the research was conducted in the absence of any commercial or financial relationships that could be construed as a potential conflict of interest.
- Copyright © 2019 Duplancic, Roguljic, Puhar, Vecek, Dragun, Vukojevic, Saraga-Babic and Kero. This is an open-access article distributed under the terms of the Creative Commons Attribution License (CC BY). The use, distribution or reproduction in other forums is permitted, provided the original author(s) and the copyright owner(s) are credited and that the original publication in this journal is cited, in accordance with accepted academic practice. No use, distribution or reproduction is permitted which does not comply with these terms.



OPEN

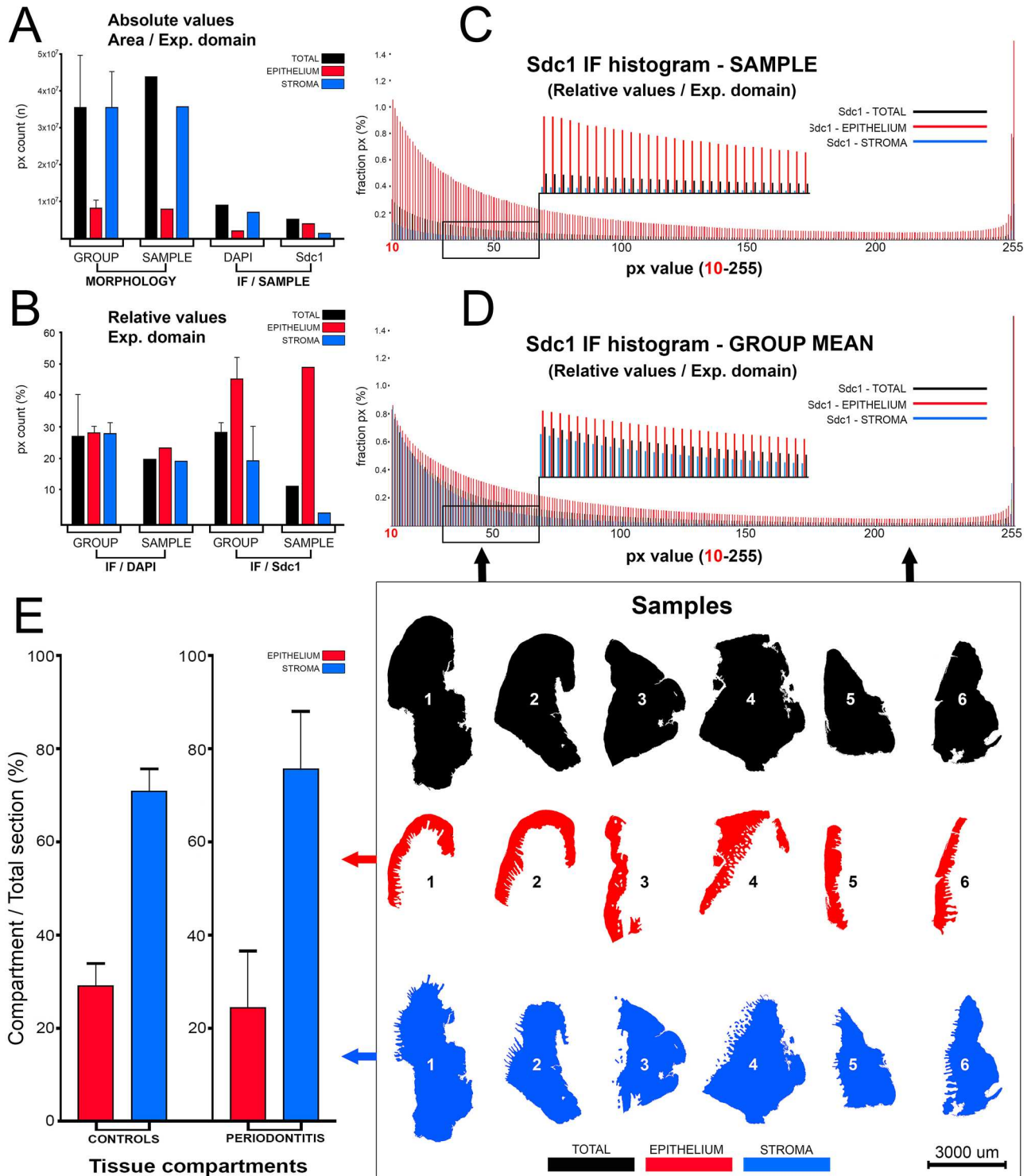
Novel approach for quantification of multiple immunofluorescent signals using histograms and 2D plot profiling of whole-section panoramic images

Roko Duplancic¹ & Darko Kero^{1,2}✉

We describe a novel approach for quantification and colocalization of immunofluorescence (IF) signals of multiple markers on high-resolution panoramic images of serial histological sections utilizing standard staining techniques and readily available software for image processing and analysis. Human gingiva samples stained with primary antibodies against the common leukocyte antigen CD45 and factors related to heparan sulfate glycosaminoglycans (HS GAG) were used. Expression domains and spatial gradients of IF signals were quantified by histograms and 2D plot profiles, respectively. The importance of histomorphometric profiling of tissue samples and IF signal thresholding is elaborated. This approach to quantification of IF staining utilizes pixel (px) counts and comparison of px grey value (GV) or luminance. No cell counting is applied either to determine the cellular content of a given histological section nor the number of cells positive to the primary antibody of interest. There is no selection of multiple Regions-Of-Interest (ROIs) since the entire histological section is quantified. Although the standard IF staining protocol is applied, the data output enables colocalization of multiple markers (up to 30) from a given histological sample. This can serve as an alternative for colocalization of IF staining of multiple primary antibodies based on repeating cycles of staining of the same histological section since those techniques require non standard staining protocols and sophisticated equipment that can be out of reach for small laboratories in academic settings. Combined with the data from ontological bases, this approach to quantification of IF enables creation of *in silico* virtual disease models.

The immunofluorescence (IF) (and immunohistochemistry (IHC) in general) has long been recognized as one of the fundamental methods for biomedical research. Following the advent of antibodies targeted against specific proteins (and to a certain degree other classes of molecules such as glycans), IF is being regularly applied as a complementary method for the molecular profiling of tissue samples, which in turn is useful for the diagnostic purposes (subtyping of diseases such as tumors, inflammatory diseases, autoimmune disorders), and for the evaluation of outcomes of different experimental procedures performed in basic biomedical research. However, the ever increasing knowledge about the complexity of molecular regulatory networks derived from numerous experiments on knockout animals, functional and high throughput studies based on tissue homogenates (genome and proteome sequencing) puts additional demands on IF/IHC-based research of human tissue samples¹. To understand how a certain protein might be relevant to any given cellular or tissue process, it is not sufficient to simply observe if the signal (or staining) of that protein is present or absent in the sample of interest, but must also be disclosed in quantifiable parameters 'How much?' and 'Where in the cell/tissue?' the staining is present. While the molecular function of a protein is determined by its biochemical properties, the protein's cellular/tissue function is influenced by its spatial relation to other proteins present in the same cellular/tissue compartment, which comprise either a well-defined functional group and/or participate in the inter-connected regulatory pathways².

¹Study Program of Dental Medicine, School of Medicine, University of Split, Soltanska 2, 21000 Split, Croatia. ²Department of Anatomy, Histology and Embryology, Laboratory for Early Human Development, School of Medicine, University of Split, Soltanska 2, 21000 Split, Croatia. ✉email: dkero@mefst.hr



◀**Figure 1.** Formatting of histogram data from panoramic IF images of Sdc1 and DAPI IF signals (sample: DK-JN19-CHP; whole-section area—12.89 mm²; epithelial fraction area—18.42%; stromal fraction area—81.58%) for statistical analysis of histomorphometry and expression domains; (Scale bar: 3000 μm). The numerical values of expression domains are presented cumulatively as absolute (A) and relative px counts (B,E), or fractionally (C,D) where the proportion of pxs is calculated for each px GV on 10–255 scale (x-axis) either for the whole section or particular tissue compartment. The advantage of this approach is that not only the total numerical value of expression domains can be calculated, but also the intensity of expression with regard to variations in px GV. Since the histogram output is congruent (total of 246 values), histograms with relative values can be used for calculation of investigated factors' expression domains as group means (D, thick black arrows) and compared between different groups of samples. In contrast to absolute values, the use of relative values (proportions/percentages) is necessary due to variations in size between sections from different samples (in frame 1–6). Accordingly, certain histomorphometric parameters might also be of importance in subsequent statistical analysis of IF signals' expression domains—these parameters are related to cellularity (presented here as cumulative values of DAPI expression domains (A,B)) and the overall tissue structure (epithelial and stromal compartment area fractions). On a between-group level, gingival samples from control and test (periodontitis) group have similar structure (E) with regard to the fraction areas of epithelial (29.13% vs. 24.27%) and stromal tissue compartments (70.91% vs. 75.72%) (*t*-test: $P=0.3075$; $P>0.1$ ($\alpha=0.1$)). Thus, the statistical comparison of mean of IF signals' expression domains between the two groups is not confounded by the potential over-estimation of the expression domains of factors with predominant expression in particular tissue compartment. (Image created in Adobe Photoshop CC 2014, ver. 6.3; <https://www.adobe.com/products/photoshop.html>).

IF signal have three main properties. The first one is the expression pattern which can be nuclear or non-nuclear (cytoplasmic, cell surface). The second one is its expression domain, i.e. the area occupied by IF signal. The third property of IF signal relates to its spatial gradient, i.e. how the IF signal is distributed within the cell/tissue based on the variations of its overall intensity. At present, there are software tools for quantification of all three of these properties, but while the conventional computer-assisted scoring systems for quantification of staining are able to turn the expression patterns and expression domains into quantifiable parameters, they still fall short on quantification of IF signals' spatial gradients³. This does not pose much of a problem for quantification of protein-markers expressed in the well-defined cell compartments (cell nuclei), or when their expression is localized to specific tissue structures and thus able to be analyzed within smaller Regions-Of-Interest (ROIs) determined by investigator⁴. However, the quantification of IF signals from ubiquitously expressed markers with non-nuclear expression patterns requires different approach. This is not only due to their generally large expression domains (which in conventional approach would necessitate the selection of increasing number of ROIs), but also because their spatial gradients are extremely important indicator of biological function^{5,6}.

Here we describe a novel approach for quantification of expression domains and spatial gradients of multiple IF signals. To demonstrate the mechanics of the approach, we used human gingiva samples stained with primary antibodies against cell surface heparan sulfate proteoglycan (HSPG) syndecan 1 (Sdc1), heparan sulfate glycosaminoglycan (HS GAG), HS GAG-biosynthesis proteins and common leukocyte antigen CD45 (inflammatory cell marker). IF signals were quantified on the high-resolution whole-section panoramic images. In this approach, we utilize the readily available software for digital image editing and digital image analysis. This approach to quantification of IF staining utilizes pixel (px) counts and comparison of px grey value (GV) or luminance for the analysis of aforementioned properties of IF staining. No cell counting is applied either to determine the cellular content of a given histological section nor the number of cells positive to the primary antibody of interest. There is also no need for selection of multiple ROIs since the entire area of histological section is quantified. Although the standard IF staining protocol is applied, the data output enables colocalization of multiple markers (up to 30) from a given histological sample. This can serve as an alternative for colocalization of IF staining of multiple markers based on repeating cycles of staining of the same histological section since those techniques require non standard staining protocols and sophisticated equipment that can be out of reach for small laboratories in academic settings.

Results

Histomorphometry—whole-section area, fraction areas, cellularity. The analysis of expression domains of IF signals between groups of samples based on panoramic images with no selection of particular ROIs can be confounded by differences in histomorphometric profiles of the samples (Fig. 1A,B,E). The first confounding factor is size—histological sections vary in size (even if they come from the same sample). Thus, instead of quantifying parameters in absolute values, relative values such as percentages or proportions should be used (Fig. 1A,B). The second confounding factor is related to the basic histological structure of the investigated tissue, which in this case is gingiva. Gingiva is comprised of two tissue compartments—epithelial compartment (gingival epithelium, sulcus epithelium and, in diseased samples, pocket epithelium) which encloses the connective tissue of stromal compartment. The substantial difference of group mean values of fraction areas of tissue compartments (or their ratios) presents a significant bias for statistical analysis of expression domains of IF signals between groups of samples if they, for instance, belong to a marker whose expression is more restricted to a particular tissue compartment—a good example is Sdc1, which is mainly expressed by epithelial cells and usually referred to as the epithelial HSPG (Heparan Sulfate ProteoGlycan)⁷. Basic histomorphometry was performed on both panoramic H/E images and panoramic IF images of histological sections from 40 samples of human gingiva (20 from healthy donors and 20 from patients with advanced generalized periodontitis). The following parameters were measured and analyzed by descriptive statistics and *t*-test: whole-section areas, fraction

areas of tissue compartments (epithelium/stroma). The mean whole-section area of control gingiva samples was 9.29 mm^2 (SD = $\pm 4.63 \text{ mm}^2$) compared with 12.21 mm^2 (SD = $\pm 3.21 \text{ mm}^2$) mean whole-section area of diseased gingiva samples. Fraction areas and group means of fraction areas were expressed as relative values in percentages. The mean epithelial and stromal fraction areas of control gingiva samples were 29.13% (SD = $\pm 12.95\%$) (epithelium) and 70.91% (SD = $\pm 14.91\%$) (stroma), whereas in diseased gingiva samples were 24.27% (SD = $\pm 12.34\%$) (epithelium) and 75.72% (SD = 12.34%) (stroma). There were no statistically significant difference of mean epithelial and stromal fraction areas between groups (*t*-test: $P = 0.3075$; $P > 0.1$ ($\alpha = 0.1$)). The measurement of cellularity in each sample was based on adding up relative values of fractional px counts sorted on a 10–255 px grey value scale from histograms of whole section and tissue compartment panoramic IF images of DAPI staining (Figs. 1, 2A,B). Thus, the expression domain of DAPI can be used to present the cellular content of histological sections—as a proportion of the whole-section or tissue compartment area covered by cell nuclei. The mean group value of the whole-section cellularity of control and diseased gingiva samples was 26.08% (SD = $\pm 10.07\%$) and 30.47% (SD = $\pm 7.51\%$), respectively. No statistically significant difference in tissue cellularity was found between groups (*t*-test: $P = 0.1989$; $P > 0.01$ ($\alpha = 0.01$)). Also, no statistically significant difference between groups was found when fractional cellularity of epithelial tissue compartments was compared (12.53% vs. 10.51% in epithelium; *t*-test: $P = 1.833$; $P > 0.01$ ($\alpha = 0.01$)). However, the fractional cellularity of stromal compartments was significantly different (13.55% vs. 19.95%; *t*-test: $P = 0.002$; $P < 0.01$ ($\alpha = 0.01$)).

Quantification of expression domains of IF signals. Mean group values of expression domains of IF signals for whole-section, epithelial and stromal tissue compartments were analysed from histograms of panoramic IF images. The comparison of expression domain of Sdc1 between healthy and diseased gingiva samples is provided as an example. In order to compensate for differences in size between different samples, fractional px counts were recalculated as percentages from the whole-section area and tissue compartment areas (epithelial, stromal) (Fig. 1C–E). The mean whole-section Sdc1 expression domain in healthy gingiva was 20.66% (SD = $\pm 3.08\%$) and in diseased gingiva 29.04% (SD $\pm 4.97\%$). The mean epithelial expression domains were 46.64% (SD = $\pm 2.76\%$) in healthy gingiva and 46.14% (SD = $\pm 3.01\%$) in diseased gingiva, whereas the mean stromal expression domains were 7.85% (SD = $\pm 2.54\%$) in healthy gingiva and 20.13% (SD = $\pm 3.11\%$) in diseased gingiva. When compared between groups of samples, no statistically significant difference was found for the whole-section (ANOVA: $P = 0.08751$; $P > 0.01$ ($\alpha = 0.01$)) and epithelial (ANOVA: $P = 0.96283$; $P > 0.01$ ($\alpha = 0.01$)) expression domains, however there was statistically significant difference between the stromal expression domains (ANOVA: $P = 1.1 \times 10^{-6}$; $P < 0.01$ ($\alpha = 0.01$)). The mean expression domain of inflammatory cell marker CD45 in diseased gingiva was found to be significantly increased compared with healthy gingiva (fourfold increase) (ANOVA: $P = 2.7 \times 10^{-8}$; $P < 0.01$ ($\alpha = 0.01$)).

When using ANOVA to compare the expression of investigated marker between samples or group of samples represented as histograms of IF staining, two parameters need to deviate in order to detect statistically significant difference—firstly, the total value of px counts (either absolute or relative) from histograms need to be different (corresponding to differences in size of expression domain); and secondly, the distribution of px counts on a 10–255 px GV scale (corresponding to the overall intensity of staining) should display difference in variance. Since the information of the actual size of expression domain and the overall intensity of staining is included in histograms, there is no need for transformation of data into expression indices. Furthermore, the number of data points from histograms (total of 246 with the px GV threshold set at 10) is sufficient to enable the use of parametric tests for statistical analysis with higher level of confidence.

Quantification and colocalization of spatial gradients of multiple IF signals. 2D plot profiling was used for quantification of spatial gradients of IF signals (Fig. 3). In this case, spatial gradients of IF signals from seven different factors (HS 3G10, HS 10E4, EXT1, EXT2, NDST1, NDST2 and CD45) detected by staining of a single sample of diseased gingiva were co-localized by plotting data from their individual T-D (top-down) 2D plots on the same graph (Fig. 4). Six simple linear regression models (each containing 8800 data points from T-D plots) were created with CD45 as dependent variable (y-axis), and other factors as independent variables (x-axis). The purpose of these models was to disclose the spatial overlap of the expression of investigated factors with the presence of stromal inflammatory infiltrate (CD45 IF signals). The correlation (*R*) and determination coefficients (R^2) vary depending on the amount of spatial overlap or colocalization of IF signals. Since most of the investigated factors are ubiquitously expressed in gingiva and not only in the areas with inflammatory infiltrate, *R* and R^2 values were closer to zero than 1 being the lowest for EXT2 ($R = 0.0219$; $R^2 = 0.0004$; $P < 1 \times 10^{-8}$ ($\alpha = 1 \times 10^{-8}$)) and highest for NDST2 ($R = 0.5502$; $R^2 = 0.3027$; $P < 1 \times 10^{-8}$ ($\alpha = 1 \times 10^{-8}$)) (Fig. 4D). Ultimately, a multiple linear regression model with CD45 as dependent variable and investigated factors as six independent variables was created. This was done in order to predict how the investigated factors affect the presence of inflammatory infiltrate—HS GAGs and related enzymes are known regulators of many cellular processes including the inflammatory response in which they can have both pro- and anti-inflammatory roles^{8–13}. The model shows high correlation and statistical significance ($R = 0.96883$; $R^2 = 0.93844$; $P < 1 \times 10^{-8}$ ($\alpha = 1 \times 10^{-8}$)) (Fig. 4B–D). For calculation of the effect, a consecutive virtual knockout (VKO) was performed. In VKO, all values in T-D plot profiles of independent variable of interest are replaced with zeros having the mean px GV from the T-D profile of dependent variable re-calculated and compared with baseline value. According to VKO, some factors were predicted to exert pro-inflammatory effect (most pronounced being that of EXT1 with 2.5-fold decrease in mean CD45 grey value after virtual knockout), whereas others were anti-inflammatory (e.g. 1.5-fold increase in total CD45 grey value after virtual knockout of EXT2). The predictions from this model are far from being conclusive because the model is based on data from a single sample. However, it serves well to demonstrate how 2D plot profiling can be used in creation of models for prediction of behavior of biological systems. The

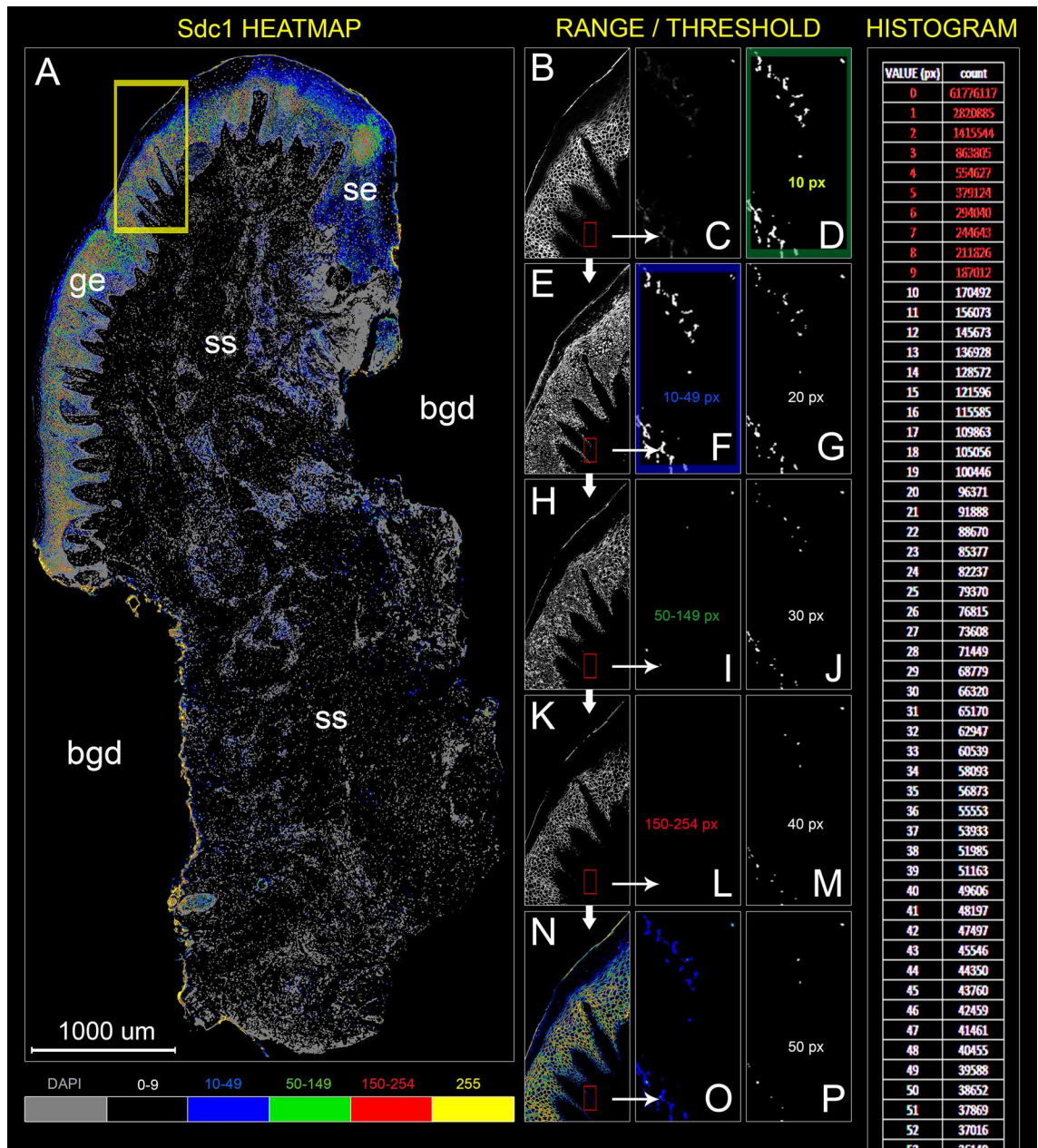


Figure 2. Panoramic four-color heatmap for visualization of IF signal dynamic range (A) and px GV threshold setting (B–P) of IF signals from anti-Sdc1 primary antibody staining of gingiva from patient with advanced generalized periodontitis (sample: DK-JN19-CHP). Designations: *bgd* background, *ge* gingival epithelium, *se* gingival sulcus epithelium, *ss* subepithelial stroma. (Heatmap intensity range: black (0–9 px), blue (10–49 px), green (50–149 px), red (150–254 px) and yellow (255 px); grey—DAPI); (Magnification: $\times 10$ (A–P); scale bar: 1000 μm). To determine the minimal value of IF signal dynamic range (px GV threshold), a series of 8-bit binary threshold images from the original panoramic IF image is made (starting from 1 px GV and higher at 1 px increments). The first 8-bit threshold image with background at 0 px GV is selected. In this case this is at px GV of 10. Subsequently, another series of 8-bit threshold images is made (threshold range) (thick white arrows; E,H,K) and matched (thin arrows) with regions on the original IF image (B, corresponding to yellow frame) containing strong (N) and weak IF signals (small red frames; C,O). Once the 8-bit threshold range image (F,I,L) which best fits the spatial distribution of weak signals is determined (F, blue frame), the third series of 8-bit threshold images is made (D,G,J,M,P). Spatial correlation between the several within-range px GV threshold areas and weak IF signals is then determined by linear regression using 2D plot profile values (THRLD₁₀ $R^2 = 0.79$, $P = 4.64 \times 10^{-61}$; THRLD₂₀ $R^2 = 0.68$, $P = 3.49 \times 10^{-45}$; THRLD₃₀ $R^2 = 0.46$, $P = 8.77 \times 10^{-26}$; THRLD₄₀ $R^2 = 0.41$, $P = 9.3 \times 10^{-22}$; THRLD₅₀ $R^2 = 0.3$, $P = 1.45 \times 10^{-15}$). The 8-bit threshold image with the highest coefficient of determination (R^2) (D, green frame) is used to set the IF signal threshold, in this case at px GV of 10. This is a cut-off for panoramic IF image histograms (far right). Counts of px corresponding to each GV below the threshold are excluded from the calculation. (Image created in Adobe Photoshop CC 2014, ver. 6.3; <https://www.adobe.com/products/photoshop.html>).

Figure 3. 2D plot profiling of spatial gradient of anti-HS 3G10 IF signals (B–F) in panoramic IF image (dimensions: 5949 × 8800 px) of histological section of gingiva from patient with advanced generalized periodontitis (A) (sample: IP-DJD-2CHP; whole section area—9.38 mm²; epithelial fraction area—37.79%; stromal fraction area—62.21%). Designations: *bgd* background, *ge* gingival epithelium, *ss* subepithelial stroma, *inf* inflammatory infiltrate; thin arrows point to pseudo-epithelial hyperplasia with rete pegs extended throughout the subepithelial stroma as a feature of active inflammation. (Magnification: × 10 (B,C) and × 20 (A); scale bar: 1000 μm). To quantify the spatial gradient of a particular IF signal, the panoramic IF image (B) and corresponding whole-section panoramic image (C) need to be profiled (thick black arrows) using ImageJ 2D plot profiler option. 2D plot profiler calculates the mean px GV (on a 0–255 scale) for each px-wide row (two-way red arrows) (D, magnified detail from the framed region on B with px grid), from top to the bottom of the panoramic IF image (T-D plot; green arrow) which corresponds to scanning direction (from marginal toward apical portion of gingiva sample). The mean px GV for each row is calculated from a number of GVs of individual pxs (corresponding to the panoramic IF image width) producing the number of mean px GV data points (corresponding to the panoramic image height) plotted on T-D plots (E, F). The x-axis is calibrated to fit the μm scale – at 10 × magnification (scan resolution is 0.53937 μm/px; total scanning distance of 4745.9 μm). To exclude the background pxs with 0 GV from the calculation, the IF signal mean px GVs (E) need to be recalculated as relative px GVs expressed in proportions/percentages from the maximal mean px GV (F, G). The binary whole-section area image is used as a reference since it displays pxs with two GVs – 0 (background) and 255 (IF signals within the histological section area (C)). Thus, the influence of all pxs located outside of the histological section on the T-D plot profile output is removed. (Image created in Adobe Photoshop CC 2014, ver. 6.3; <https://www.adobe.com/products/photoshop.html>).

underlying assumption is that the biological functions of molecular components of tissue are closely related to their spatial distribution.

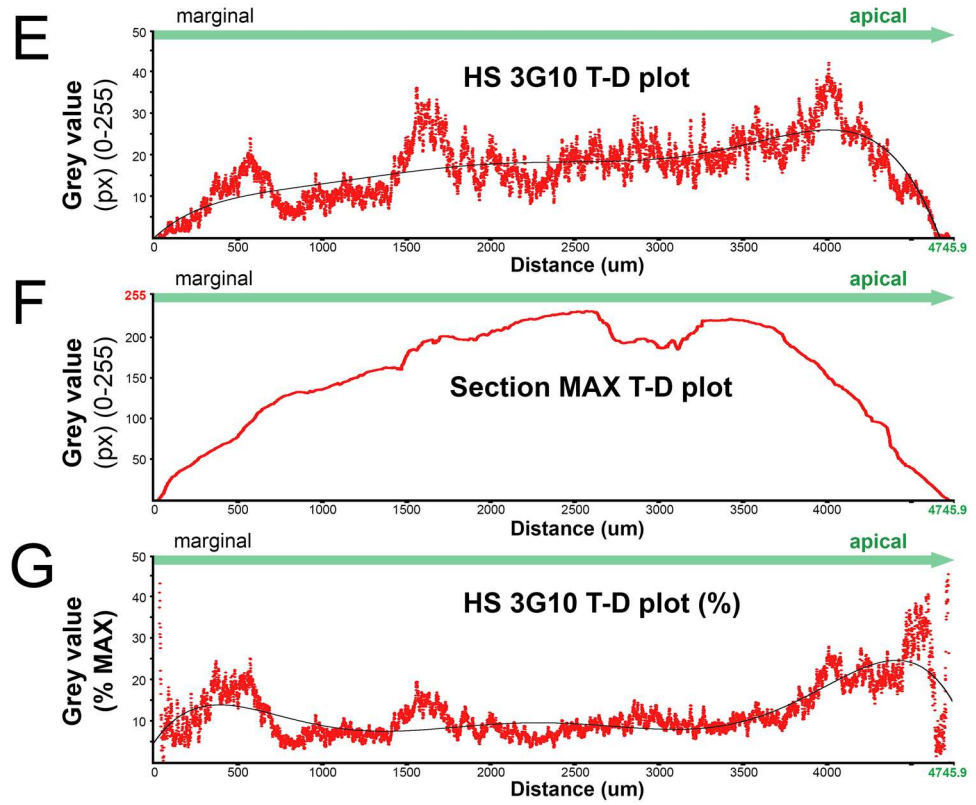
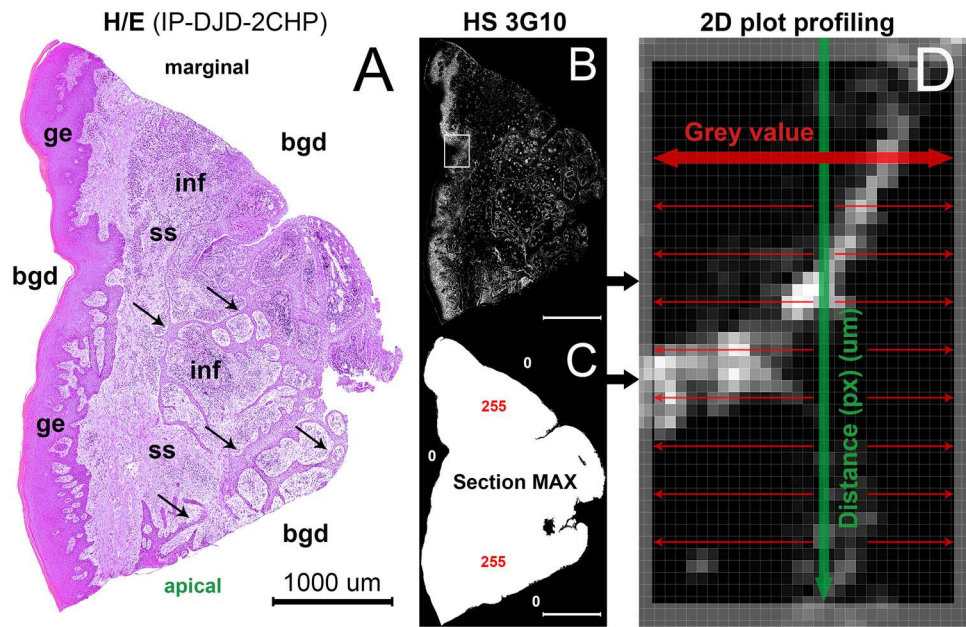
The precision of colocalization of multiple factors and statistical models based on 2D plot profiling can be confounded by the differences in shape and cellular content of serial sections within sample. Thus, the number of sections compatible for multiple colocalization analysis was assessed by correlating spatial gradients of DAPI staining (Table 1). DAPI staining is visible in all serial sections because it is routinely performed as the background IF staining. Ideally, the spatial gradients of particular staining performed consecutively on serial sections from the same sample should display perfect linear correlation if the sections have identical shape and cell content. According to the analysis of DAPI staining, near perfect correlation can be observed for up to 30 serial sections from individual gingiva samples ($R = 0.9996$; $R^2 = 0.9993$; $P \sim 0$). This also means that if each of those serial sections is successfully stained with different primary antibody, spatial gradients of up to 30 different factors could be colocalized by 2D plot profiling without the introduction of significant sampling error.

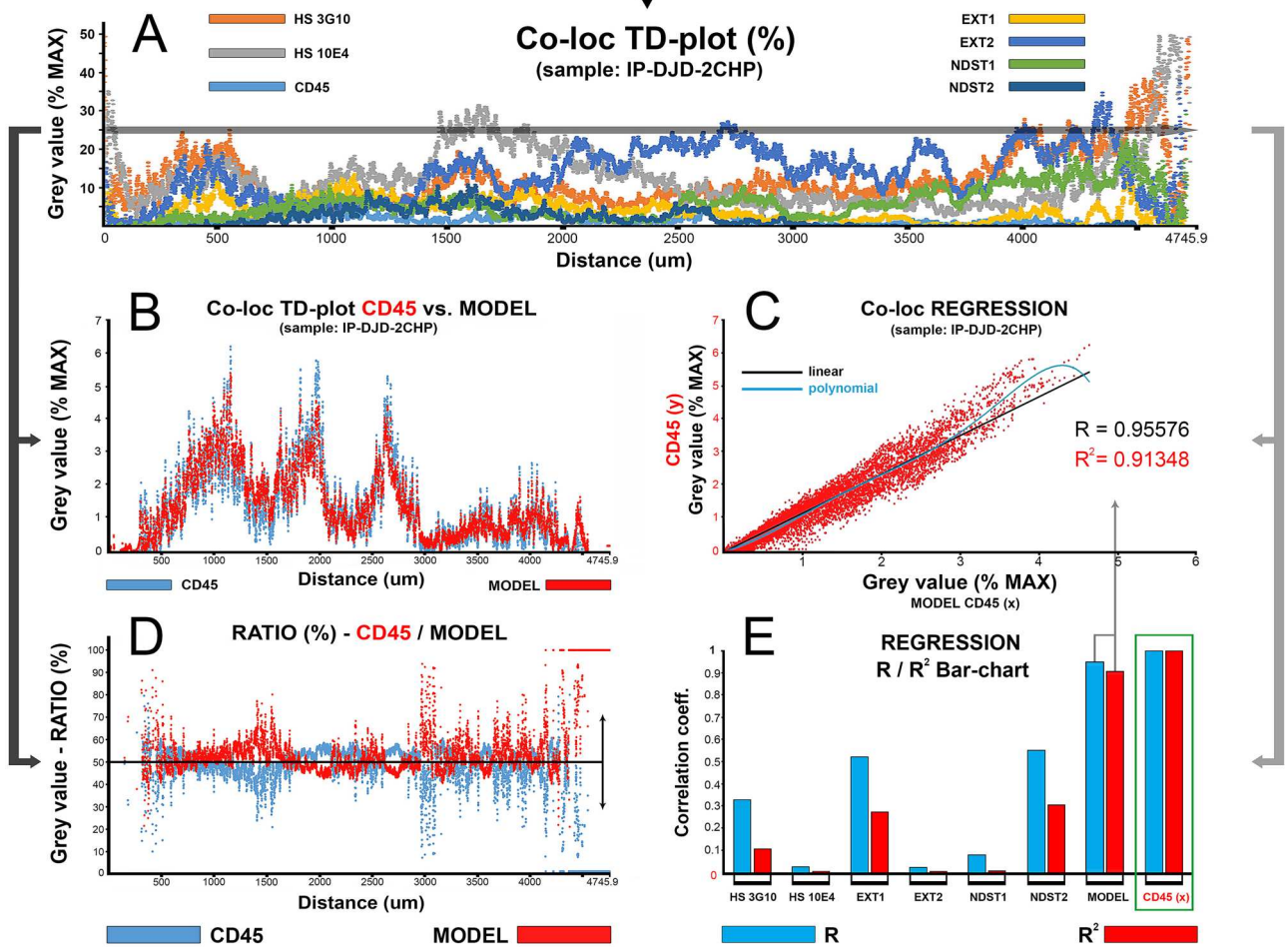
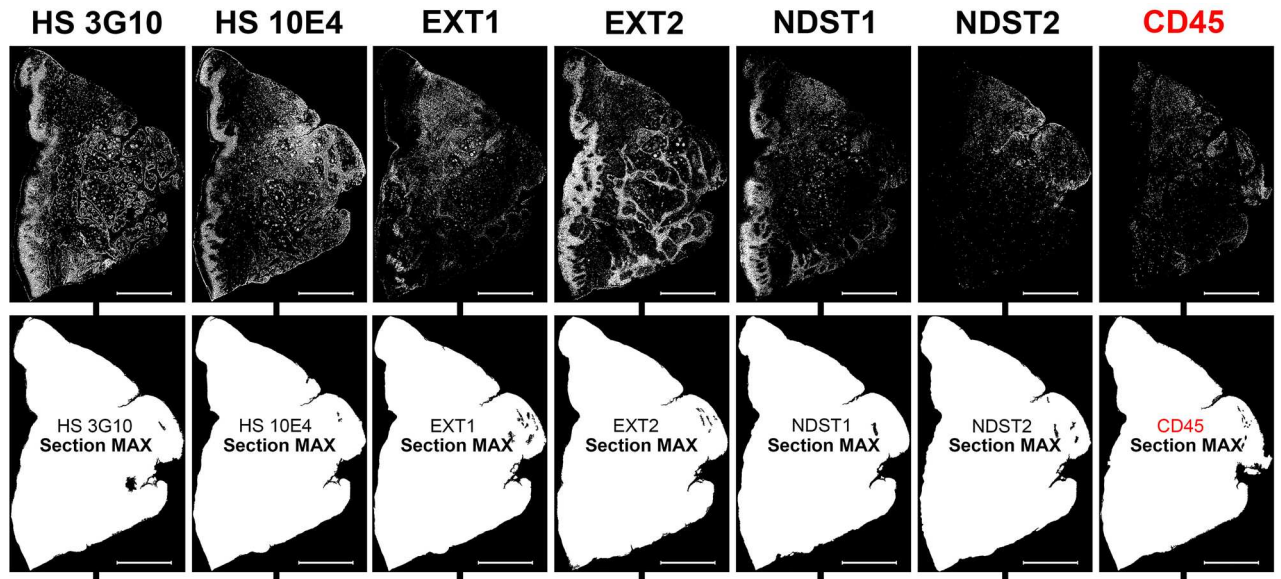
Discussion

In this paper we described a novel approach for quantification of colocalization of IF signals of multiple markers on high-resolution panoramic images. For the presentation purposes, human gingiva samples were stained with several primary antibodies against specific extracellular matrix (ECM) components and common leukocyte marker CD45. Attributes of IF signal, such as the expression domain (i.e., proportion of the whole-section or tissue compartment areas covered by IF signal) and spatial gradients (variation of IF signal intensity, or mean px GV, in entire histological section), were quantified by histograms and 2D plot profiles of panoramic IF images, respectively. The data output from histograms and 2D plot profiles is suitable for parametric statistical tests even if a small number of samples is analyzed. ANOVA was used for analysis of expression domains to disclose if the overall expression of investigated factors significantly changes when compared between groups of samples. Simple and multiple linear regression were used for the analysis of spatial gradients with assumption of true linear relationship between the two or multiple investigated factors if their expressions perfectly overlap in space. Additionally, regression models were created to predict how the changes of expression of a set of investigated factors (as independent variables) affect the overall expression of the outcome marker (in this case CD45). For this type of analysis, a computational colocalization of multiple factors needs to be done where a sample 2D plot profile is used as a template (Fig. 4).

This approach to quantification of IF signals is entirely based on simple algorithms for px count and measurement of px luminance (px GV). It can also serve as an alternative to cell counting tools even though significant improvements of these tools have been recently introduced (including the new „Mastodon“ plugin for ImageJ)¹⁴. The rationale behind this statement is that when IF signals (or IHC staining) get recorded on a digital image, they assume digital properties and can be perceived as a number of pixels with specific GV and location. As demonstrated here, the cellular content of histological sections can be calculated in the form of the expression domain of IF signals of DAPI nuclei marker.

In this approach, there is no need for selection of multiple ROIs because panoramic images are analyzed entirely. The selection of ROIs prior to actual quantification of IF signals of IHC staining is the usual procedure in many semi-quantitative and quantitative scoring systems^{15–19}. While this may be sufficient when analyzing particular structures or expression of highly specific markers, it may not be adequate for quantification of ubiquitously expressed markers whose expression domains cannot be covered by several ROIs on high magnification (Fig. 5). However, the downside of IF signal quantification from the entire panoramic image is that significant effort must be invested in histo-morphometric profiling of histological sections (Fig. 1). This is mostly related to variations in tissue structure and (to some degree) to the choice of markers whose IF signals need to be analyzed. Either way, the histo-morphometric parameters need to be quantified in detail, as these may provide a source of confounders for subsequent statistical analysis of IF. Another confounder is related to the thresholding of IF





◀**Figure 4.** 2D plot profiling for quantification and correlation of spatial gradients of IF signals from primary antibodies against HS GAG, HS GAG biosynthesis enzymes and common leukocyte antigen (CD45) in histological sections of gingiva from patient with advanced generalized periodontitis (sample: IP-DJD-2CHP). (Magnification: $\times 10$; scale bar: 1000 μm). Spatial gradients of IF signals are plotted simultaneously on a single T-D plot (A) to devise the regression model. The purpose of the model is to disclose to how the presence of inflammatory cell infiltrate correlates with the expression of HS GAG and HS GAG biosynthesis enzymes. The spatial gradient for CD45 IF signal is set as dependent variable (y), whereas the spatial gradients for IF signals from HS 3G10, HS 10E4, EXT1, EXT2, NDST1 and NDST2 are designated as independent variables (x). Based on the regression function, a predicted CD45 spatial gradient is calculated (MODEL CD45) and plotted with the actual values of CD45 spatial gradient on several different plots (B–D) to check for the goodness of fit. The model is statistically significant ($\alpha = 1 \times 10^{-8}$, $P < 1 \times 10^{-8}$) and reveals that the presence of inflammatory infiltrate can be well correlated with the expression of HS GAG and HS GAG biosynthesis enzymes (linear model: $R = 0.95576$; $R^2 = 0.91348$; polynomial curve fitting: $R = 0.96883$; $R^2 = 0.93844$). As visualized on the bar-chart of correlation coefficients (E), the deviation of the model (C,D) can be attributed to the low individual correlation of particular independent variables such as HS 3G10 ($R = 0.32808$; $R^2 = 0.10763$), HS 10E4 ($R = 0.02445$; $R^2 = 0.00059$), EXT2 ($R = 0.02191$; $R^2 = 0.00048$) and NDST1 ($R = 0.07752$; $R^2 = 0.00601$). IF signals of HS 3G10, HS 10E4, EXT2 and NSDT1 have larger expression domains and display different patterns than those of EXT1 and NDST2 (more confined to stromal compartment with CD45) (top row). Thus, the spatial gradients of EXT1, NDST2 display stronger correlation (EXT1– $R = 0.52064$; $R^2 = 0.27107$) (NDST2– $R = 0.55022$; $R^2 = 0.30275$) with CD45. (Image created in Adobe Photoshop CC 2014, ver. 6.3; <https://www.adobe.com/products/photoshop.html>).

Simple linear regression – DAPI staining T–D plots							
Sections	R ²	Std. Error†	Coefficient	CI‡		Significance [§]	
Sequence*				Lower	Upper	F value	P
REF (x)/(y)	1	1.9553×10^{-14}	1	1	1	2.6303×10^{34}	0
5th (x)	0.9989	1.0879	1.0022	1.0007	1.0038	8.4859×10^6	0
10th (x)	0.9980	1.4998	1.0082	1.0062	1.0103	4.4611×10^6	0
15th (x)	0.9943	2.5441	0.9883	0.9848	0.9919	1.5447×10^6	0
20th (x)	0.9940	2.6178	1.0091	1.0053	1.0127	1.4584×10^6	0
25th (x)	0.9846	4.1924	1.0086	1.0027	1.0146	5.6328×10^5	0
30th (x)	0.98141	4.6084	1.0317	1.0251	1.0384	4.6466×10^5	0

Table 1. Compatibility of serial sections for in silico colocalization and regression analysis of multiple IF signals based on correlation of spatial gradients of DAPI staining in whole-section panoramic images (sample: IP-DJD-2CHP). *Serial number of histological section stained with DAPI—the first section was used as reference (REF) (dependent variable—y) for auto-correlation (reference model); DAPI staining of every fifth consecutive section up to 30th section (independent variables—x) was correlated with the DAPI staining of the referent section. †Standard error and coefficients (slopes) are expressed in px grey values. ‡Confidence interval for coefficients is set at 99%. §Statistical significance is set at $\alpha = 1 \times 10^{-8}$ ($P < 1 \times 10^{-8}$).

signals or separating IF signals from non-specific staining (auto-fluorescence). Therein reside the advantages of IF compared to chromogens in IHC—fluorochromes provide signals with higher dynamic range which is of utmost importance for determination of IF signal threshold. Equalization of images, i.e. the increase of dynamic range, is recognized as an important step in digital image post-processing for the purpose of signal thresholding in IF and IHC²⁰. In this approach, the equalization of panoramic IF images is done simultaneously with image acquisition and not in the post-processing. Apart from the improvement of the workflow, this generally reduces the exposure of sections to excitation light, which in turn reduces the possibility of photo-bleaching of IF signals. While this is not an issue when only a few IF images need to be captured, in acquisition of panoramic IF images this is useful since the exposure of histological sections to excitation light is prolonged.

In quantification and analysis of spatial gradients of IF signals, the influence of the very shape of histological sections must not be neglected. Since the quantification of IF signals is done on serial histological sections, a certain margin of sampling error might be introduced because no two sections from the same sample are completely identical. The simplest way to check if the difference in section shape within a sample can confound the subsequent statistical analysis of spatial gradients is by correlating 2D plot profiles of DAPI IF signals from consecutive histological sections. From tissue samples analyzed here, up to 30 consecutive sections with DAPI IF signals display almost perfect shape ad cell content correlation in single and multiple linear regression models (Table 1). This provides us with the estimate of the total number of different factors whose IF signals' spatial gradients can be quantified, co-localized and correlated using 2D plot profiling if successfully stained on consecutive sections. It should also be noted that when using 2D plot profiles for quantification of spatial gradients of IF signals, the formatting and precise alignment of panoramic IF images is of paramount importance (Figs. 3, 4). In this approach, image alignment was done semi-automatically by action presets customized exclusively for

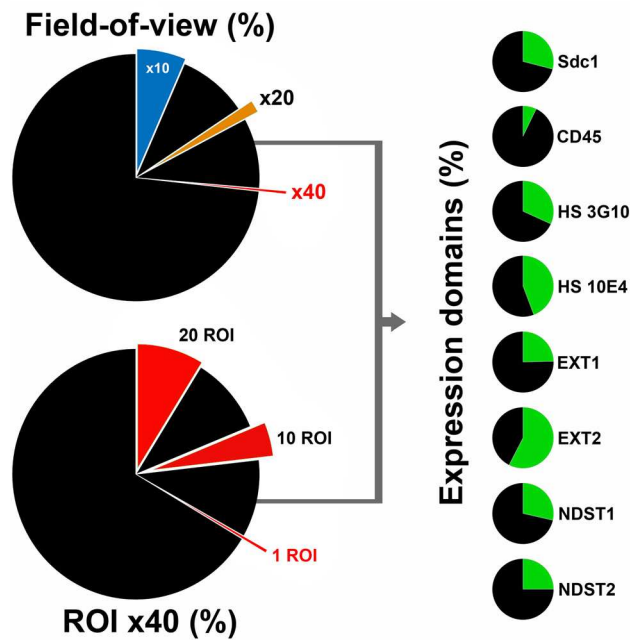


Figure 5. Pie-chart comparison of expression domains of investigated factors with field-of-view (magnifications $\times 10$, $\times 20$ and $\times 40$) and ROIs ($\times 40$) expressed as fraction areas (%) from the whole-section area of samples of human gingiva. Whole-section areas absent of IF signals outside of field-of-view or excluded from ROIs are presented in black color. HSPGs, enzymes for biosynthesis of HS GAGs and HS GAGs (as much as the other ECM components) are ubiquitously expressed in various tissues and have large expression domains. Thus, the traditional approach for analysis and quantification of IHC staining or IF signals in which several ROIs are selected under high magnification ($\times 40$) might introduce bias by excluding from the analysis significant portions of the tissue. The expression domains are presented as cumulative values which does not account for the actual spatial distribution of IF signals. Another issue is related to the size of the analyzed samples. Histological sections of human gingiva analyzed here are relatively small (between 9 mm^2 and 12 mm^2)—a single ROI at magnification $\times 40$, covers only 0.44% of the whole-section area, meaning that selection of 10 ROIs (4.4%; 95.6% of whole-section area excluded from analysis) or 20 ROIs (8.8%; 91.2% of whole-section area excluded from analysis) cannot cover the entire expression domain of investigated factors. In bigger tissue samples, as the whole-section area increases, the fraction areas from field-of-view and selected ROIs proportionally decrease. (Image created in Adobe Photoshop CC 2014, ver. 6.3; <https://www.adobe.com/products/photoshop.html>).

each sample in Adobe Photoshop CC 2014 ver. 6.3 (Adobe, San Jose, CA, USA), although there is a variety of pattern recognition software currently available that might be used to improve the workflow²¹.

In the past the technology was developed as a way to simultaneously co-localize and identify unique combinations of multiple markers on a cellular or tissue level—multi-epitope ligand cartography (MELC) is based on direct IF immunolabeling and consecutive imaging of tens to hundred of proteins in the same field-of-view^{22,23}. In MELC, the IF immunolabeling of multiple markers is performed on the same histological section by repeating cycles of IF staining. Image acquisition and photo-bleaching of captured IF signals in situ are performed before the immunolabeling of another marker takes place. Along with the unified coding system in which the IF signals from multiple markers are detected as spatial signal maps and presented as binary vectors, the main advantage of MELC is that by using a relatively small number of samples it can identify hierarchical organization of complex protein networks with great precision. Additionally, by application of MELC, even the histomorphometric parameters of tissues can be analyzed as is nicely demonstrated in studies on effects of cancer heterogeneity on effectiveness of various cancer therapeutics²⁴. On the downside, the protocol for MELC is fully automated and requires the use of sophisticated equipment which may be out-of-reach for small laboratories in academia settings.

The spatial distribution of proteins and other classes of molecules is important determinant of their biological function in tissues. In interpretation of data from IHC-based methods every effort is made to connect those two. With no disregard to well-known limitations of IHC, the validity of such interpretation is significantly related to the ability of researchers who use IHC to precisely quantify expression of investigated markers^{5,25}. Another issue is the traditionally small amount of markers that can be simultaneously co-localized and visualized and there is every need to go beyond the confinements of double immunolabeling. The approach presented here is not the first one to improve that, but it does attempt to do so based on the standard staining protocols. It also aims to improve on the co-occurrence/correlation bias which is recognized in standard px-based approaches

to colocalization of IF and counteracted by application of various tests such as Costes' randomization test^{33–35}. Namely, the co-occurrence/correlation bias, as recognized by the standard px-based approaches to colocalization of IF which utilize histograms, is effectively eliminated when using 2D plot profiles for colocalization of IF from multiple markers as described here. 2D plot profiles contain more information than histograms, and when integrated in regression matrices, correlation analysis reflects both the overlap and variation of intensity of IF signals in space. Thus, more robust statistical models on functional importance of colocalization of multiple markers can be created. The number of factors that can be included in these models is sufficient to completely or partially reconstruct the signaling pathways or elements of regulatory networks in silico using data from ontologic bases as the template. Then, the ultimate test of the validity of this approach to quantification of IF can be conducted—by seeing if the predictions from statistical models can be replicated in actual live experiments.

Methods

For this study we used samples of human gingiva from the archival collection of histological slides at the Department of Anatomy, Histology and Embryology (School of Medicine, University of Split). Gingiva samples were obtained from patients diagnosed with general destructive periodontitis. Patient screening and recruitment were done in accordance with the guidelines for classification of periodontal and peri-implant diseases as described previously^{26,27}. The sampled tissue was free gingiva which is a part of masticatory gingiva that spans from the gingival margin to the ridge of the alveolar bone. Procurement and processing of tissue samples were approved by the Ethical and Drug Committee of School of Medicine, University of Split (Class: 003-08/17-03/0001, No: 2181-198-03-04-17-0043) in accordance with Helsinki Declaration²⁸. To facilitate the proper tissue orientation during the paraffin embedding, vestibular (labial/buccal) aspects of gingiva samples were marked by waterproof color immediately prior to sampling. Fixation in 4% paraformaldehyde took between 24 to 48 h. The samples were then cut in serial 5 µm thick sections and mounted on glass slides (three sections per slide). Every 10th slide was stained with hematoxylin/eosin (H/E) to confirm the presence and preservation of the structures of interest (gingival epithelium, gingival sulcus epithelium and subepithelial stroma).

Immunofluorescence (IF) staining. Deparaffinization and IF staining were performed following the standard protocol in our laboratory^{29,30}. Background blocking was done using Abcam Protein Block (ab64226; Abcam, UK) for 25 min after the antigen retrieval. The primary antibodies used for IF staining were: mouse-monoclonal anti-Sdc1 (syndecan 1) (1:100; ab34164; Abcam, UK), rabbit polyclonal anti-EXT1 (exostosin 1) (1:100; ab126305; Abcam, UK), rabbit polyclonal anti-EXT2 (exostosin 2) (1:50; ab102843; Abcam, UK), rabbit polyclonal anti-NDST1 (bifunctional heparan sulfate N-deacetylase/N-sulfotransferase (1) (1:50; ab129248; Abcam, UK), rabbit polyclonal anti-NDST2 (bifunctional heparan sulfate N-deacetylase/N-sulfotransferase (2) (1:100; ab151141; Abcam, UK), mouse monoclonal anti CD45 (common leukocyte antigen/inflammatory cell marker) (1:200; ab8216; Abcam, UK), mouse monoclonal anti-HS 3G10 (heparan sulfate glycosaminoglycan, 3G10 epitope) (1:100; 370260-1; Seikagaku Corp., Japan) and mouse monoclonal anti-HS 10E4 (heparan sulfate glycosaminoglycan, 10E4 epitope) (1:100; 370255-1; Seikagaku Corp., Japan). Sections were incubated with primary antibodies for 24 h at 4 °C. For application of anti-HS 3G10, sections had to be pre-treated with Heparinase III enzyme (0.02 IU/50 µl) (Seikagaku Corp, Japan) at 37 °C for 2 h. Secondary antibodies were used at dilution 1:400: anti-mouse Alexa Fluor 488 (GREEN; ab150105; Abcam, UK) and anti-rabbit Alexa Fluor 488 (GREEN; ab150077; Abcam, UK). Cell nuclei were stained with diamidino-2-phenylindole (DAPI). Staining of samples of oral mucosa from maxillary tuberosity was performed as positive control. Expression patterns (nuclear/non nuclear) of IF signals were examined by the intensity correlation analysis (ImageJ Coloc Finder plugin) as previously described^{31,32}. IF signals of all primary antibodies displayed non-nuclear expression patterns (data not shown).

Image acquisition and processing—H/E panoramic images. Orientation slides stained with H/E were examined under Olympus BX40 light microscope equipped with standard digital camera (Olympus DP27, Olympus, Tokyo Japan), and area-scan high-resolution digital camera (Basler aceA2500-14gm, Basler, Germany) for manual slide scanner (Microvisioneer, Esslingen am Neckar, Germany). H/E panoramic images were captured at magnification ×20 (exposure time: 8 ms; ISO: 100), exported as JPEG files and post-processed in Adobe Photoshop CC 2014 ver 6.3 (Adobe, San Jose, CA, USA). Orientational alignment was done by the action presets customized for every sample individually because sections from different samples vary in size and shape. The presets contain 4 basic operations for orientational alignment („Transform“, „Rotate“, „Crop“ and „Merge“) and enable execution of these operations by a single click. The overall size of H/E panoramic images (600 MB on average) was reduced by converting them from TIFF to JPEG format on a high-resolution background (600 dpi) in order to minimize image detail loss and to preserve data storage space since these images were only used for preliminary histomorphometry. Epithelial tissue compartment (gingival epithelium, gingival sulcus epithelium) and stromal tissue compartment were masked using graphic pen tablet (Wacom Intuos PRO, Wacom Co., Saitama, Japan). Whole-section area and areas of tissue compartments were measured by Magic Wand Tool/Histogram to be expressed as absolute values in px (number of px) (whole-section area), and as relative values (proportion of the whole-section area) expressed in percentages (%) (areas of tissue compartments). These measurements were subsequently used to calculate the group averages of whole-section areas and tissue compartment (epithelial, stromal) fraction areas. The same procedure was performed on panoramic IF images.

Image acquisition—panoramic IF images. IF stained slides were examined under Zeiss Axio Observer inverted epifluorescence microscope (Carl Zeiss Microscopy GmbH; Jena, Germany) equipped with Zeiss Axio-cam 506 digital color camera (Carl Zeiss Microscopy GmbH, Jena, Germany) set for full frame resolution

(2752 × 2208 px) which enables the acquisition of photomicrographs in original black & white (8-bit depth, TIFF), as well as in color format (Pseudo-colorizer module, sRGB color mode). Acquisition and stitching of photomicrographs into panoramic IF images were done simultaneously using Multi-channel and Panorama modules in ZEN 2.5 software (Carl Zeiss Microscopy GmbH; Jena, Germany), respectively. The settings for image histogram equalization (background subtraction and contrast adjustment) were saved as the main calibration preset executed automatically during the entire procedure of photomicrograph acquisition. Therefore, the panoramic IF images were rendered to display full dynamic range of px GV on a scale from 0 (pure black) to 255 (pure white). Depending on the fluorescence channel, this also allowed us to make 2- to 5-fold reduction of the overall exposure time for photo-micrograph acquisition and consequently avoid the risk of photo-bleaching of IF signals. The exposure time in Multi-channel module for blue channel (DAPI IF signals) was set at 35 ms, whereas for the green channel (IF signals of primary antibodies) was set at 800 ms. For the stitching of photomicrographs (tiles) into panoramic IF images, tiles were captured sequentially by manual navigation along x/y axes guided by the on-screen live view of DAPI channel with minimal 20% overlap (x-axis) and 10% maximal shift (y-axis) between individual tiles. Panoramic IF images were closely inspected for quality (tiles alignment, stitching artefacts) and stored in raw format as CZI files (Zeiss proprietary file format) that contains original data and metadata. CZI files of each panoramic IF image were then exported in multiple TIFF format files—original black & white 8-bit, pseudo-colored 8-bit and merged 16-bit). Only the original black & white 8-bit panoramic IF images were post-processed and used for further analysis. Namely, the pseudo-colorization reduces the overall dynamic range of IF signals making the adjustment of cut-off signal threshold (i.e. discrimination between the true IF signals and autofluorescence) and consequently the quantification of IF signals less precise. The reduction of dynamic range occurs because every software for image editing and/or image analysis „perceives“ colors as different shades of grey and by default converts color images to black & white images. How application of different software and even different image modes can affect the measurement of signal intensity (as output of px GV) is shown on a color step-tablet (Fig. 6). In order to confirm that IF signals display full dynamic range, four-color heatmaps of panoramic IF images were made, where each color represents a range of px GV as follows: BLUE (10–49; weak intensity), GREEN (50–149; moderate intensity), RED (150–254; strong intensity), YELLOW (255; very strong intensity). The protocol for the making of heatmaps was previously described³¹.

Post-processing of panoramic IF images. Post-processing of panoramic IF images was performed entirely in Adobe Photoshop CC ver. 6.3 (Adobe, San Jose, CA, USA). Orientational alignment of panoramic IF images was done in a similar way described for panoramic H/E images. Since the panoramic IF images were taken at ×10 magnification at full-frame resolution (and thus were comprised of less individual photo-micrographs), there was no need for significant size reduction compared with panoramic H/E images. However, some formatting was still needed since ImageJ cannot load images which exceed certain dimensions limit (~120 000 000 px²) irrespective of the file format. For the creation of whole-section area panoramic images, IF signal and corresponding DAPI panoramic IF images were merged („Lighten“ blending mode) and then thresholded at the lowest px GV of 1 rendering them as binary images with only two px GV values (0 and 255). The remaining black gaps at the interface between the background and tissue section on the newly produced merged images were traced with „Brush“ tool in order to enable the selection of the whole section by „Magic Wand“ tool. Then, „Total fill“ option was applied to fill the whole section area with pure white color. Blending masks for tissue compartments (epithelial/stromal) were made by tracing the interface between the epithelial and stromal tissue with „Brush“ tool. In this case, DAPI panoramic images were used as templates. IF signal panoramic images and whole-section area panoramic images were each blended with masks in „Darken“ blending mode. „Darken“ blending mode compares the px GV (luminance) of each pixel from the background and foreground blending layer and renders visible either the background or foreground blending layer px depending on which one is darker. In case the two px are of equal GV, the background px remains visible after blending. Mathematical function for „Darken“ blending mode is: $R = \min\{F, B\}$ (R – resultant pixel; F —blending foreground pixel; B = background pixel). For each pair of IF signal and DAPI panoramic images, nine additional panoramic images were created—epithelial and stromal IF signal, epithelial and stromal DAPI and binary 8-bit images of the whole section area, two blending masks, epithelial and stromal compartment area (Fig. 7).

IF signal thresholding, histograms and 2D plot profiling. For the IF signal thresholding, we first made the measurement of the total background px GV at low GV thresholds (1–10) using „Threshold“ option in Adobe Photoshop CC 2014 ver 6.3 (Adobe, San Jose, CA, USA). After that, a ROI on panoramic image which contains weak IF signals is selected (Fig. 2C) and inspected for a range of px GV (10–50) (Fig. 2O), cropped and further processed in at least five 8-bit threshold images at specific threshold values (for example at 10, 20, 30, 40 and 50). 2D plot profiles of the original ROI and threshold ROIs were made in ImageJ and used for correlation analysis—the IF signal threshold cut-off value equals to the threshold value of the threshold ROI which best correlates with the original ROI. Because we used 2D plots of threshold binary images containing px with GV of either 0 or 255, the correlation is strictly proportional to the amount of spatial overlap (or location) of the patterns on threshold images (Fig. 2D,G,J,M,P) with IF signals on the original ROI (Fig. 2C; Supplementary material: Dataset 3). Once the histograms of panoramic IF signal images are created („Histogram“ option in ImageJ), px counts for GVs below the threshold cut-off can be discarded (Fig. 2). The histograms have the uniform output of 256 values irrespective of the type or size of the image. This enables the presentation of expression domains of IF signals in the form of fractional px counts for each px GV. It also makes more sense because expression domain is generally comprised of signals with a range of intensities—if the expression domain is simply presented as a single cumulative value, a lot of information is lost. Once the IF signal thresholding was complete, the original panoramic IF images were further edited in order to „physically“ exclude px with GV below the

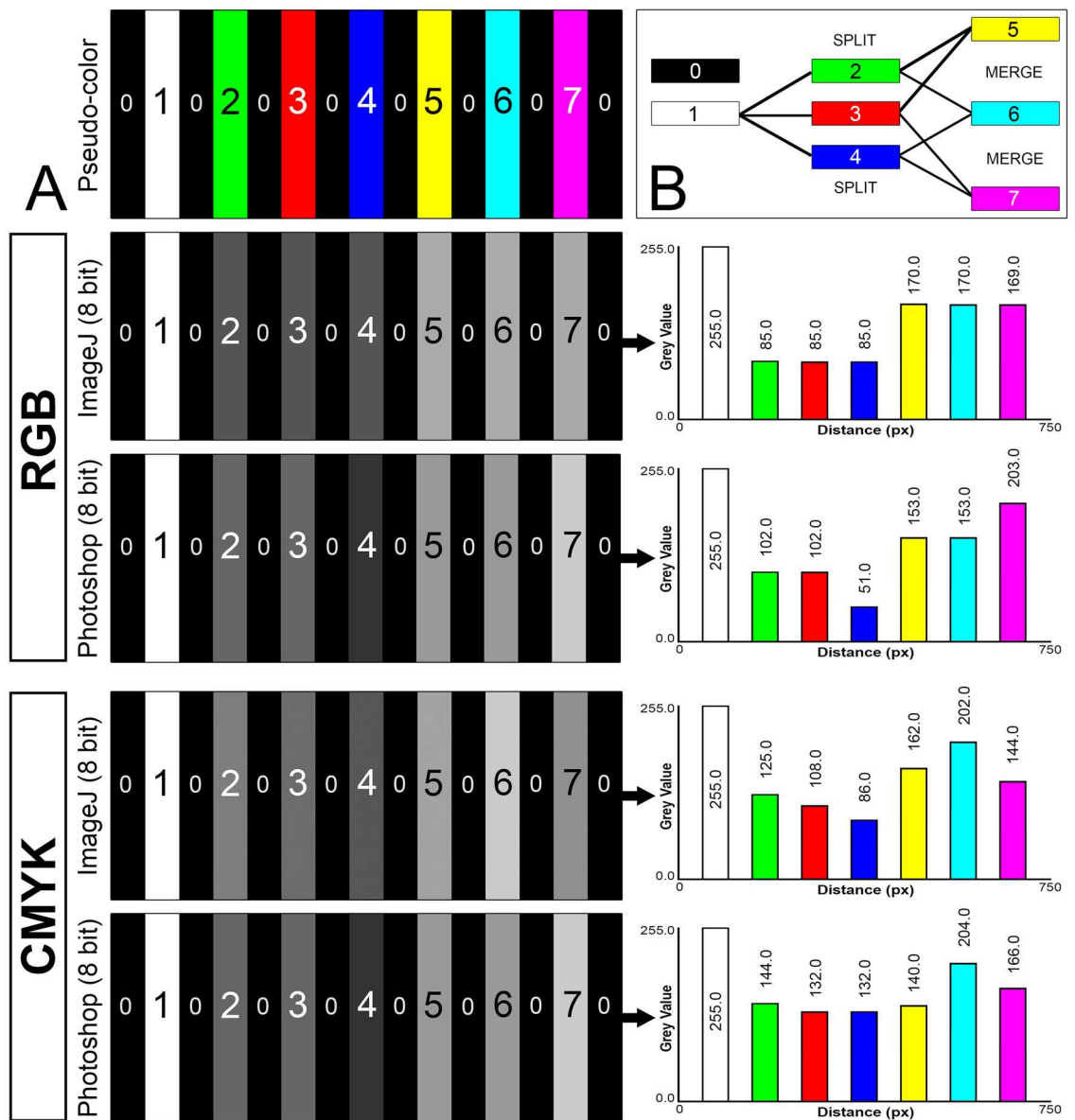


Figure 6. 750 × 150 pixel (px) color step-tablet (A) comprised of seven panels separated by black spaces (0). White panel (1) is pseudo-colored in green (2), red (3) and blue (4) with three different merge combinations: yellow (green/red merge) (5), cyan (green/blue merge) (6) and magenta (red/blue merge) (7) as shown on scheme (B). Thick arrows point to 2D plot profiles of average px grey values (GVs) measured in left–right direction for each desaturated (converted to black & white) step-tablet. The average px GV is calculated from a 0 to 255 scale of all pxs in a 1 px-wide columns. Each panel from step-tablets contains the total number of 50 1 px-wide columns, and each column contains 150 pxs. Thus, for white panel (1), the average px GV is consistently 255.0 since all pxs belonging to white panel have GV of 255. Conversely, the average GV of black spaces is 0.0 since all black pxs have GV of 0. It should be noted that the average grey values for all pseudo-colored panels are lower than the GV of the white panel. That is because the image analysis software discriminates colors in different shades of grey and prior to the analysis of colorized (or pseudo-colored) image, desaturation (i.e. conversion to 8-bit black & white image) must be performed. The output average GV measurements of pseudo-colored panels can also be affected by the inherent differences of algorithms for color desaturation applied in different software (see step-tablets for comparison between different software) and by different color modes such as Red–Green–Blue (RGB) and Cyan–Magenta–Yellow–Key (CMYK). These points should be considered for quantification IF signals based on measurements made on color images, especially with regard to double IF. (Image created in Adobe Photoshop CC 2014, ver. 6.3; <https://www.adobe.com/products/photoshop.html>).

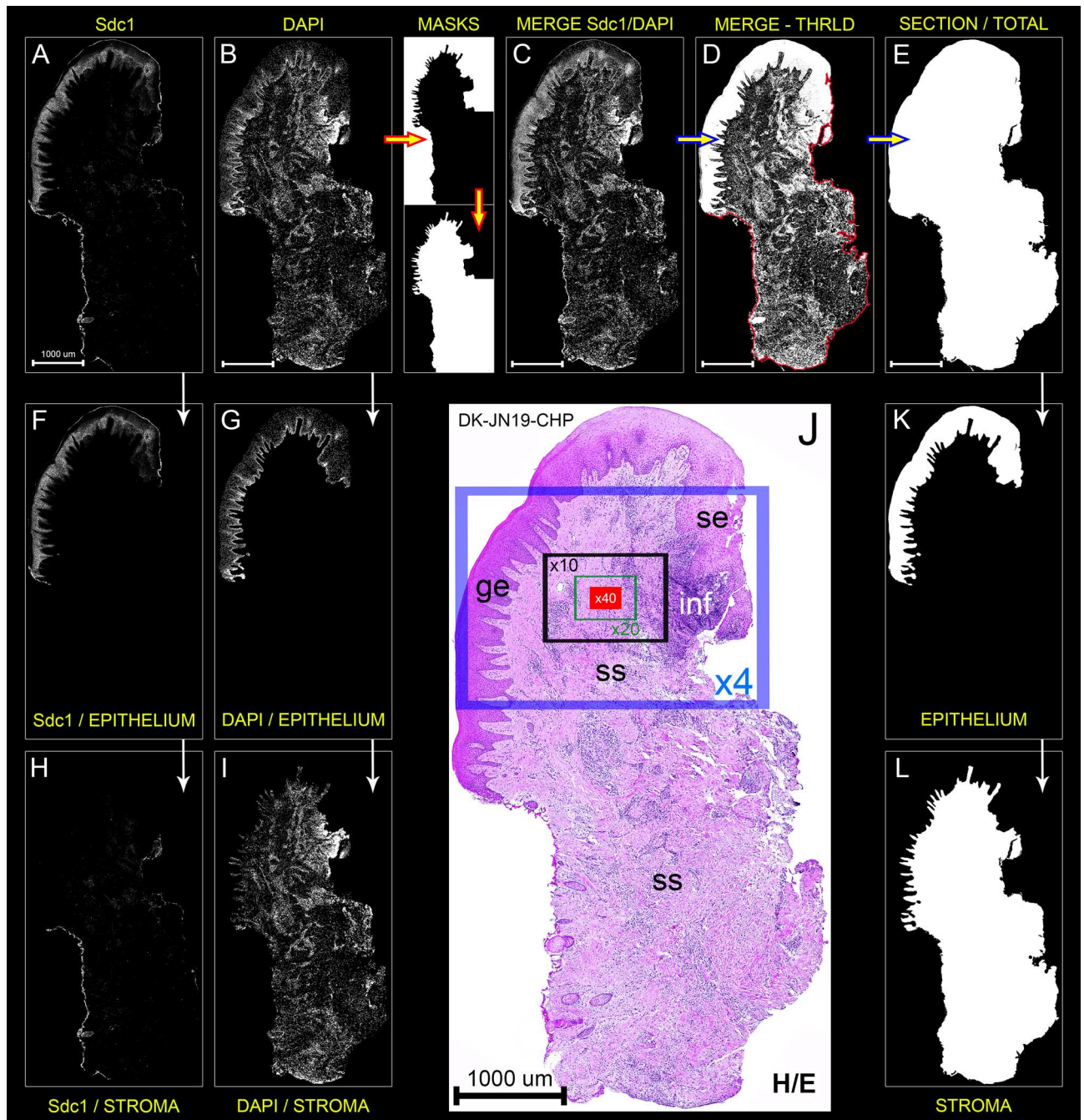


Figure 7. Processing protocol for 8-bit (black & white) high-resolution panoramic IF images (dimensions: $6250 \times 12,000$ px) of histological section of gingiva from patient with advanced generalized periodontitis (sample: DK-JN19-CHP) containing anti-Sdc1 IF staining (A) and DAPI nuclear staining (B). Designations: *ge* gingival epithelium, *se* gingival sulcus epithelium, *ss* subepithelial stroma, *inf* inflammatory infiltrate, *H/E* hematoxylin/eosin staining. (Magnification: $\times 10$ (A–I, K, L) and $\times 20$ (J); scale bar: $1000 \mu\text{m}$). By tracing DAPI image as a template (background image), blending masks are made (thick yellow/red arrows) which will be applied for separation of epithelial compartment (includes both *ge* and *se*) and stromal compartment (thin white arrows) on Sdc1, DAPI and whole section area panoramic IF images. Merging is done in Adobe Photoshop CC 2014 ver 6.3 (Adobe, San Jose, CA, USA) using „DARKEN“ blending which enables visibility only of those parts of background under the white area of blending mask (thin white arrows; F–I, K–L). To produce a whole-section area panoramic image (E), Sdc1 and DAPI panoramic IF images are merged (C), and then set to the lowest possible threshold (1 px GV) (D) in order to partially fill in-section areas which contain no staining. The remaining gaps on the outer edges of newly produced whole-section area panoramic image (around *ss* where the overall texture of tissue is loose) are closed with „BRUSH“ tool (D, red color). This enables the precise selection of the total section area using „MAGIC WAND“ tool and subsequent filling of the whole-section area with pure white by „FILL“ option (E, thick yellow/blue arrows). Thus, the panoramic IF images are processed for quantification of histomorphometric parameters (surface size, cellularity, tissue compartment areas) and IF signals of investigated factors (expression domain, spatial gradient) in the whole-section scale or in particular tissue compartments. In contrast to standard procedures for quantification of IHC and IF signals, there is no need for selection of multiple ROIs on high magnification ($\times 40$). (J; field-of-view at magnifications $\times 4$ (blue frame), $\times 10$ (black frame), $\times 20$ (green frame), $\times 40$ (red frame)). (Image created in Adobe Photoshop CC 2014, ver. 6.3; <https://www.adobe.com/products/photoshop.html>).

threshold cut-off. Each original panoramic IF signal images was merged with counterpart inverted threshold cut-off panoramic IF image using „Darken“ blending mode. As such, the original panoramic IF signal images are fully processed for the analysis of spatial gradients of IF signals. Again, the spreadsheet table of top-down (vertical) 2D plot profile of the panoramic IF image is extracted in ImageJ and calibrated to fit the μm scale (at $\times 10$ magnification 1 px = 0.53937 μm) (Fig. 3A–D). 2D plot profiles basically list the average px GV's per 1 px-wide rows. In contrast to histograms, this means that the total number of output values depends on image dimensions. For the panoramic IF images of gingival samples taken at magnification $\times 10$, the average 2D plot profile output is between 8000–12000 values. 2D plot profiles are then used for *in silico* colocalization of multiple IF signals and correlation analysis of their spatial gradients.

Statistical analysis. The attributes of IF signals were fully quantified and presented as continuous variables. Therefore, only parametric tests were used for the statistical analysis. Histomorphometric parameters of gingiva samples (whole section area, fraction areas of tissue compartments, cellularity) were analyzed by descriptive statistics and *t*-test. The level of significance for basic histomorphometric profiling of samples was set at $\alpha = 0.1$ ($P < 0.1$) since these parameters were mostly presented as cumulative (single) values. For the analysis of expression domains of IF signals, single factor ANOVA was used with the level of significance set at $\alpha = 0.01$ ($P < 0.01$). Correlation of spatial gradients of IF signals was analyzed by simple and multiple linear regression with the level of significance set at $\alpha = 1 \times 10^{-8}$ ($P < 1 \times 10^{-8}$). Based on multiple linear regression, a model was created in order to assess what kind of effect might each investigated factor (HS GAG, EXTs, NDSTs) exert on the presence of inflammatory infiltrate (CD45 set as main dependent variable) by means of VKO, i.e. replacing all values in top-down 2D plots (T-D plots) of individual factors with 0. For T-D plots image is scanned in direction from the top to the bottom (along image height). The reason for choosing linear regression model was following: when the values from T-D plots of IF signals from two different factors are plotted on the x/y axis graph in the same sequence as they appear on the T-D plot, but in a way that T-D plot values from factor 1 go on x-axis (independent variable), and those of factor 2 on y-axis (dependent variable), they would conform to a linear function if they perfectly co-localize in space. Conversely, the more scatter appears on the x/y axis graph, the less two factors co-localize in space. The refinement of multiple linear regression model was done by non-linear polynomial regression (6th order). Statistical tests and calculations were performed in Microsoft Office Excel 2016 (Microsoft Corp., Redmond, WA, USA). Datasets used for statistical analysis are publicly available (Supplementary material).

Ethical approval. Procurement and processing of tissue samples used in this study were approved by the Ethical and Drug Committee of School of Medicine, University of Split (Class: Class: 003-08/17-03/0001, No: 2181-198-03-04-17-0043).

Received: 11 August 2020; Accepted: 8 April 2021

Published online: 21 April 2021

References

- Huss, R. & Coupland, S. E. Software-assisted decision support in digital histopathology. *J. Pathol.* <https://doi.org/10.1002/path.5388> (2020).
- Tummers, M. & Thesleff, I. The importance of signal pathway modulation in all aspects of tooth development. *J. Exp. Zool. Part B Mol. Dev. Evol.* **312B**, 309–319. <https://doi.org/10.1002/jez.b.21280> (2009).
- Taylor, C. R. & Levenson, R. M. Quantification of immunohistochemistry—issues concerning methods, utility and semiquantitative assessment II. *Histopathology* **49**, 411–424. <https://doi.org/10.1111/j.1365-2559.2006.02513.x> (2006).
- Riber-Hansen, R., Vainer, B. & Steiniche, T. Digital image analysis: A review of reproducibility, stability and basic requirements for optimal results. *APMIS Acta Pathol. Microbiol. Immunol. Scand.* **120**, 276–289. <https://doi.org/10.1111/j.1600-0463.2011.02854.x> (2012).
- Roper, J. A., Williamson, R. C. & Bass, M. D. Syndecan and integrin interactomes: Large complexes in small spaces. *Curr. Opin. Struct. Biol.* **22**, 583–590. <https://doi.org/10.1016/j.sbi.2012.07.003> (2012).
- Rozario, T. & DeSimone, D. W. The extracellular matrix in development and morphogenesis: A dynamic view. *Dev. Biol.* **341**, 126–140. <https://doi.org/10.1016/j.ydbio.2009.10.026> (2010).
- Bernfield, M. *et al.* Biology of the syndecans: A family of transmembrane heparan sulfate proteoglycans. *Annu. Rev. Cell Biol.* **8**, 365–393. <https://doi.org/10.1146/annurev.cb.08.110192.002053> (1992).
- Čavar, I. & Kero, D. Correlation of the expression of hyaluronan and CD44 with the presence of gingival inflammatory infiltrate in advanced generalized periodontitis. *ST-OPEN* **1**, 16. <https://doi.org/10.48188/so.1.11> (2020).
- Barritault, D. *et al.* RGTA((R)) or ReGeneraTing agents mimic heparan sulfate in regenerative medicine: from concept to curing patients. *Glycoconj. J.* **34**, 325–338. <https://doi.org/10.1007/s10719-016-9744-5> (2017).
- Esko, J. D. & Selleck, S. B. Order out of chaos: Assembly of ligand binding sites in heparan sulfate. *Annu. Rev. Biochem.* **71**, 435–471. <https://doi.org/10.1146/annurev.biochem.71.110601.135458> (2002).
- Presto, J. *et al.* Heparan sulfate biosynthesis enzymes EXT1 and EXT2 affect NDST1 expression and heparan sulfate sulfation. *Proc. Natl. Acad. Sci. U.S.A.* **105**, 4751–4756. <https://doi.org/10.1073/pnas.0705807105> (2008).
- Talsma, D. T. *et al.* Endothelial heparan sulfate deficiency reduces inflammation and fibrosis in murine diabetic nephropathy. *Lab. Invest.* **98**, 427–438. <https://doi.org/10.1038/s41374-017-0015-2> (2018).
- Zhang, X., Wang, F. & Sheng, J. “Coding” and “Decoding”: Hypothesis for the regulatory mechanism involved in heparan sulfate biosynthesis. *Carbohydr. Res.* **428**, 1–7. <https://doi.org/10.1016/j.carres.2016.04.002> (2016).
- Xie, Y. *et al.* Deep voting: A robust approach toward nucleus localization in microscopy images. *Med. Image Comput. Comput. Assist. Interv.* **9351**, 374–382. https://doi.org/10.1007/978-3-319-24574-4_45 (2015).
- Boric, K. *et al.* Expression of apoptotic and proliferation factors in gastric mucosa of patients with systemic sclerosis correlates with form of the disease. *Sci. Rep.* **9**, 18461. <https://doi.org/10.1038/s41598-019-54988-0> (2019).

16. Kero, D. *et al.* Expression of cytokeratin 8, vimentin, syndecan-1 and Ki-67 during human tooth development. *J. Mol. Histol.* **45**, 627–640. <https://doi.org/10.1007/s10735-014-9592-1> (2014).
17. Kotsovilis, S. *et al.* Syndecan-1 immunohistochemical expression in gingival tissues of chronic periodontitis patients correlated with various putative factors. *J. Periodontol Res.* **45**, 520–531. <https://doi.org/10.1111/j.1600-0765.2009.01267.x> (2010).
18. Matos, L. L. *et al.* Immunohistochemistry quantification by a digital computer-assisted method compared to semiquantitative analysis. *Clinics* **61**, 417–424. <https://doi.org/10.1590/s1807-59322006000500008> (2006).
19. Sanchez-Romero, C., Bologna-Molina, R., Mosqueda-Taylor, A. & Paes de Almeida, O. Immunohistochemical expression of GLUT-1 and HIF-1 α in tooth germ, ameloblastoma, and ameloblastic carcinoma. *Int. J. Surg. Pathol.* **24**, 410–418. <https://doi.org/10.1177/1066896916640359> (2016).
20. Waisberg, J. *et al.* Immunohistochemical expression of heparanase isoforms and syndecan-1 proteins in colorectal adenomas. *Eur. J. Histochem. EJH* **60**, 2590. <https://doi.org/10.4081/ejh.2016.2590> (2016).
21. Parfitt, G. J. *et al.* A novel immunofluorescent computed tomography (ICT) method to localise and quantify multiple antigens in large tissue volumes at high resolution. *PLoS ONE* **7**, e53245. <https://doi.org/10.1371/journal.pone.0053245> (2012).
22. Schubert, W. Topological proteomics, toponomics, MELK-technology. *Adv. Biochem. Eng. Biotechnol.* **83**, 189–209. https://doi.org/10.1007/3-540-36459-5_8 (2003).
23. Schubert, W. *et al.* Analyzing proteome topology and function by automated multidimensional fluorescence microscopy. *Nat. Biotechnol.* **24**, 1270–1278. <https://doi.org/10.1038/nbt1250> (2006).
24. Park, C. C. *et al.* Rapid and automated multidimensional fluorescence microscopy profiling of 3D human breast cultures. *Integr. Biol. Quant. Biosci. Nano Macro* **5**, 681–691. <https://doi.org/10.1039/c3ib20275e> (2013).
25. Kero, D. & Saraga-Babic, M. Odontogenesis—a masterful orchestration of functional redundancy or what makes tooth bioengineering an intrinsically difficult concept. *J. Stem Cell Res. Therap.* **1**, 7. <https://doi.org/10.15406/jsrt.2016.01.00022> (2016).
26. Duplancic, R. *et al.* Syndecans and enzymes for heparan sulfate biosynthesis and modification differentially correlate with presence of inflammatory infiltrate in periodontitis. *Front. Physiol.* **10**, 1248. <https://doi.org/10.3389/fphys.2019.01248> (2019).
27. Papananou, P. N. *et al.* Periodontitis: Consensus report of workgroup 2 of the 2017 world workshop on the classification of periodontal and peri-implant diseases and conditions. *J. Clin. Periodontol.* **45**(Suppl 20), S162–S170. <https://doi.org/10.1111/jcpe.12946> (2018).
28. Williams, J. R. The declaration of Helsinki and public health. *Bull. World Health Organ.* **86**, 650–652. <https://doi.org/10.2471/blt.08.050955> (2008).
29. Kero, D. *et al.* Involvement of IGF-2, IGF-1R, IGF-2R and PTEN in development of human tooth germ—an immunohistochemical study. *Organogenesis* **12**, 152–167. <https://doi.org/10.1080/15476278.2016.1197460> (2016).
30. Kero, D. *et al.* Analysis of expression patterns of IGF-1, caspase-3 and HSP-70 in developing human tooth germs. *Arch. Oral Biol.* **60**, 1533–1544. <https://doi.org/10.1016/j.archoralbio.2015.07.004> (2015).
31. Kero, D., Bilandzija, T. S., Arapovic, L. L., Vukojevic, K. & Saraga-Babic, M. Syndecans and enzymes involved in heparan sulfate biosynthesis and degradation are differentially expressed during human odontogenesis. *Front. Physiol.* **9**, 732. <https://doi.org/10.3389/fphys.2018.00732> (2018).
32. Kero, D. *et al.* Regulation of proliferation in developing human tooth germs by MSX homeodomain proteins and cyclin-dependent kinase inhibitor p19(INK4d). *Organogenesis* **13**, 141–155. <https://doi.org/10.1080/15476278.2017.1358337> (2017).
33. Costes, S. V. *et al.* Automatic and quantitative measurement of protein-protein colocalization in live cells. *Biophys. J.* **86**, 3993–4003. <https://doi.org/10.1529/biophysj.103.038422> (2004).
34. Aaron, J. S., Taylor, A. B. & Chew, T. L. Image co-localization—co-occurrence versus correlation. *J. Cell Sci.* <https://doi.org/10.1242/jcs.211847> (2018).
35. Dunn, K. W., Kamocka, M. M. & McDonald, J. H. A practical guide to evaluating colocalization in biological microscopy. *Am. J. Physiol. Cell Physiol.* **300**, C723–742. <https://doi.org/10.1152/ajpcell.00462.2010> (2011).

Acknowledgements

The authors wish to thank engineers from Zeiss, IT specialists from Adobe and Microsoft, as well as IT aficionados involved in development of ImageJ for their efforts in providing us with such wonderful tools for biomedical research. Special thanks to Domagoj Kljakovic-Gaspic BSC for additional language editing of the manuscript.

Author contributions

R.D. performed immunolabeling, devised protocol for image acquisition, performed image post-processing and data analysis, reviewed literature, written manuscript draft; D.K. conceptualized the study, devised protocols for image post-processing, quantification of immunolabeling and statistical analysis of data, reviewed literature, written and edited manuscript draft.

Funding

The authors disclose receipt of the following financial support for the research, authorship, and /or publication of this article: Darko Kero was supported by the annual grant for researchers awarded by the University of Split.

Competing interests

The authors declare no competing interests.

Additional information

Supplementary Information The online version contains supplementary material available at <https://doi.org/10.1038/s41598-021-88101-1>.

Correspondence and requests for materials should be addressed to D.K.

Reprints and permissions information is available at www.nature.com/reprints.

Publisher's note Springer Nature remains neutral with regard to jurisdictional claims in published maps and institutional affiliations.





Open Access This article is licensed under a Creative Commons Attribution 4.0 International License, which permits use, sharing, adaptation, distribution and reproduction in any medium or format, as long as you give appropriate credit to the original author(s) and the source, provide a link to the Creative Commons licence, and indicate if changes were made. The images or other third party material in this article are included in the article's Creative Commons licence, unless indicated otherwise in a credit line to the material. If material is not included in the article's Creative Commons licence and your intended use is not permitted by statutory regulation or exceeds the permitted use, you will need to obtain permission directly from the copyright holder. To view a copy of this licence, visit <http://creativecommons.org/licenses/by/4.0/>.

© The Author(s) 2021

Article

Heparan Sulfate Glycosaminoglycan Is Predicted to Stabilize Inflammatory Infiltrate Formation and RANKL/OPG Ratio in Severe Periodontitis in Humans

Roko Duplancic ¹, Marija Roguljic ², Darko Bozic ³ and Darko Kero ^{4,*}¹ Study Program of Dental Medicine, University of Split School of Medicine, 21000 Split, Croatia² Department of Oral Pathology and Periodontology, Study Program of Dental Medicine, University of Split School of Medicine, 21000 Split, Croatia³ Department of Periodontology, School of Dental Medicine, University of Zagreb, 10000 Zagreb, Croatia⁴ Laboratory for Early Human Development, University of Split School of Medicine, 21000 Split, Croatia

* Correspondence: dkero@mefst.hr

Abstract: Since chronically inflamed periodontal tissue exhibits extracellular matrix (ECM) degradation, the possible alternative to standard periodontitis treatment is to restore ECM by supplementing its components, including heparan sulfate glycosaminoglycan (HS GAG). Supplementation of the degraded ECM with synthetic derivatives of HS GAGs has been shown to be effective for periodontal tissue regeneration in experimental animal models of periodontitis. However, the potential of HS GAG supplementation for the treatment of periodontal disease in humans is still unknown. Here, we used a statistical model to investigate the role of HS GAG on inflammatory infiltrate formation and alveolar bone resorption in humans with severe periodontitis. The model was based on data from immunofluorescence staining (IF) of human gingiva samples, and reconstruction of a subset of HS GAG-related proteins from STRING reactome database. According to predictions, increased expression of native HS GAG might stabilize the accumulation of gingival inflammatory infiltrate (represented by the general inflammatory cell marker CD45) and alveolar bone resorption (represented by Receptor Activator of Nuclear KB ligand (RANKL) and osteoprotegerin (OPG) ratio) but could not restore them to healthy tissue levels. Therefore, supplementation of native HS GAG may be of limited benefits for the treatment of severe periodontitis in humans.

Keywords: heparan sulfate glycosaminoglycan; immunofluorescence; inflammation; periodontitis; statistical modeling



Citation: Duplancic, R.; Roguljic, M.; Bozic, D.; Kero, D. Heparan Sulfate Glycosaminoglycan Is Predicted to Stabilize Inflammatory Infiltrate Formation and RANKL/OPG Ratio in Severe Periodontitis in Humans. *Bioengineering* **2022**, *9*, 566. <https://doi.org/10.3390/bioengineering9100566>

Academic Editors: Apostolos I. Tsolakis and Chengfei Zhang

Received: 27 September 2022

Accepted: 13 October 2022

Published: 18 October 2022

Publisher's Note: MDPI stays neutral with regard to jurisdictional claims in published maps and institutional affiliations.



Copyright: © 2022 by the authors. Licensee MDPI, Basel, Switzerland. This article is an open access article distributed under the terms and conditions of the Creative Commons Attribution (CC BY) license (<https://creativecommons.org/licenses/by/4.0/>).

1. Introduction

Periodontitis is one of the most common chronic inflammatory diseases. Worldwide, almost 11% of the population is affected by severe forms of the disease [1]. While many environmental and intrinsic factors play a role in the pathogenesis of periodontitis, it is well known that the inadequate host immune response to the presence of microbial biofilm on the tooth surface perpetuates the vicious cycle of inflammation and periodontal tissue breakdown. Severe forms of periodontitis are characterized by extensive degradation of periodontal tissue, which ultimately leads to the loss of the affected teeth [2,3].

Extracellular matrix (ECM) components such as heparan sulfate glycosaminoglycans (HS GAGs) and their corresponding cell surface receptors such as HS proteoglycans (HSPGs) of the syndecan (Sdc) family have long been shown to play important roles in tissue homeostasis [4–6]. Studies on Sdcs knockout mice (KO) have shown that the absence of individual Sdcs in tissues can promote inflammation, disrupt wound healing, and increase resistance to microbial infection [7,8]. In addition, overexpression of Sdcs has been reported in various pathological conditions [9,10]. Therefore, Sdcs may be characterized as modulators of cellular processes. Many of these effects are in turn mediated by HS GAGs,

which are the major ligands of Sdcs. HS GAGs can sequester and release a variety of important regulators of cell behavior (growth factors, morphogens, inflammatory mediators). In addition, the turnover of HS GAGs is highly responsive to changes in the local microenvironment and is influenced by several enzymes that regulate the biosynthesis, modification, and degradation of HS GAGs. Total and/or conditional KO of genes encoding these enzymes (such as EXTs, NDSTs, and HPSE1) may also influence the course of inflammation and susceptibility to microbial infection in various tissues in multiple ways [11–14].

The gold standard in the treatment of periodontitis is nonsurgical subgingival instrumentation of the affected root surfaces to remove biofilm formation, and in some cases, antimicrobials with antiseptic and antibiotic agents are used [15]. However, other approaches that might influence the host response to the bacterial load have not been adequately explored. Because chronically inflamed periodontal tissues exhibit persistent degradation of the ECM, the alternative to standard treatment is to rebuild the ECM using synthetic derivatives of ECM components. In a series of *in vivo* studies in rodent models of periodontitis, a synthetic HS GAG based on dextran polymers was administered to diseased animals by multiple subcutaneous injections [16]. In addition to the resolution of gingival tissue inflammation, regeneration of alveolar bone, periodontal ligament, and cementum was also reported. These results are significant for two reasons: (i) periodontal disease in the animals was induced by mono- or polymicrobial infection with periodontopathogenic bacteria, which more closely mimics the onset of periodontitis in humans compared with ligature-based models; (ii) resolution of inflammation and regeneration of periodontal tissue occurred without any attempt to control the microbial component by mechanical debridement of the affected teeth. Therefore, these results suggest that drugs based on derivatives of ECM components (such as HS GAG) may be sufficient for the complete treatment of periodontitis.

While synthetic HS GAGs have been shown to be effective in experimental animal models of periodontitis, their potential for treating periodontal disease in humans is still unknown. Using a statistical model, we aimed to predict whether changes in the bioavailability and/or structure of native HS GAG have the potential to resolve inflammation and promote alveolar bone regeneration in humans with severe forms of periodontitis. The statistical model was based on *in silico* co-localization of several markers from immunofluorescence staining (IF) of human gingival samples and reconstruction of the reactome of a subset of HS GAG-related proteins using the Protein Ontology database.

2. Materials and Methods

2.1. Samples Procurement

This study is based on data obtained from human gingival samples preserved as histological slides in the archival collection of the Department of Anatomy, Histology and Embryology, School of Medicine, University of Split. The samples were obtained from 40 participants, who were divided into two equally sized groups: healthy controls and periodontitis affected. The periodontitis group consisted of patients diagnosed with generalized periodontitis at stage III or IV according to the latest classification [17]. Detailed inclusion and exclusion criteria have been described previously [18]. In short, the inclusion criteria were age of at least 18 years, good general health, healthy periodontal tissue (controls) and severe periodontitis stage III and IV (periodontitis group). The exclusion criteria were the presence of systemic diseases and conditions (e.g., diabetes mellitus), long-term medication or medical history of systemic antibiotic therapy within last six months, pregnancy, alcohol and drug use, and the presence of lesions in the vicinity of the sampling area.

In short, study participants were recruited from the Department of Oral Pathology and Periodontology University of Split Hospital Centre. Clinical parameters such as probing depth, gingival recession, clinical attachment level, full-mouth plaque score and full-mouth bleeding scores were recorded. Patients were selected only after referral for clinical crown lengthening (both groups), surgical periodontal treatment, and/or tooth extraction

(periodontitis group only). The samples of gingiva were stored in sealed containers with paraformaldehyde and immediately taken to the laboratory for further processing.

Each participant received, reviewed, and signed two documents: informed consent to participate in the study and consent to the collection and processing of personal data, all in accordance with the WMA Declaration of Helsinki [19], the EU General Data Protection Regulation, and Croatian laws: Health Protection Act, Health Data and Information Act, Patients' Rights Protection Act, and Dentistry Act.

2.2. Immunohistochemistry and Immunofluorescence Staining

Immunohistochemical staining (IHC) was performed on every 10th slide using hematoxylin/eosin (H/E) to verify the preservation of tissue morphology and proper alignment of tissue compartments (gingival epithelium, gingival sulcus epithelium, and subepithelial stroma). We also used the Alcian Blue staining kit (pH 1.0, mucin staining) (ab150661) (Abcam plc, Cambridge, UK), a polyvalent basic dye that binds to highly sulfated mucosubstances (including glycosaminoglycans). Staining with Alcian Blue was performed according to the manufacturer's instructions.

The IF staining protocol from our laboratory has been described previously [20,21]. For staining with anti-HS3G10, a minor adaptation of the protocol was necessary including pretreatment of histological slides with the enzyme Heparinase III (0.02 IU/50 μ L) (Seikagaku Corp, Tokyo, Japan) at 37 °C for 2 h was performed before antigen retrieval [22]. The primary and secondary antibodies used for this study are listed in Table 1.

Table 1. Primary antibodies are used for IF staining of histological sections of gingiva.

Primary Antibody	Dilution	Description/Function
Mouse monoclonal anti-Sdc1 (ab34164) * ^a	1:100	HSPGs; type 1 transmembrane proteins; cell surface receptors for HS GAG which participate in cell proliferation, cell migration and cell-matrix interactions; members of syndecan protein family
Rabbit polyclonal anti-Sdc2 (ab191062) * ^b	1:200	
Rabbit polyclonal anti-Sdc4 (ab24511) * ^b	1:100	
Rabbit polyclonal anti-EXT1 (ab126305) * ^b	1:100	Exostosins; endoplasmic reticulum resident type 2 transmembrane glycosyltransferases; involved in biosynthesis of HS GAG (chain elongation step); members of the GAGosome complex
Rabbit polyclonal anti-EXT2 (ab102843) * ^b	1:50	
Rabbit polyclonal anti-NDST1 (ab129248) * ^b	1:50	Bifunctional enzymes involved in biosynthesis of HS GAG; catalyze N-deacetylation and N-sulfation of glucosamine monosaccharides of HS GAG (initial sulfation step); members of the GAGosome complex
Rabbit polyclonal anti-NDST2 (ab151141) * ^b	1:100	
Mouse monoclonal anti-HS3G10 (370260-1) ^{†c}	1:100	HS GAG marker; reacts with HS GAG 3G10 epitope generated after the digestion of HS GAG with heparinase III enzyme; binds to non-sulfated regions of HS GAG; does not react with other classes of GAGs
Mouse monoclonal anti-HS10E4 (370255-1) ^{†c}	1:100	HS GAG marker; reacts with HS GAG 10E4 epitope which includes N-sulfated glucosamines; reactivity abolished after treatment with heparinase III enzyme; does not react with other classes of GAGs
Rabbit polyclonal anti-HPSE1 (ab85543) * ^b	1:200	Heparanase 1 enzyme (endoglycosidase); degrades HS GAG at cell surface and within ECM into shorter oligosaccharide fragments; facilitates shedding of syndecans' extracellular domains
Rabbit polyclonal anti-SULF1 (ab32763) * ^b	1:200	Heparan sulfate 6-O-endo-sulfatases; selectively remove 6-O-sulfate groups from HS chains of HSPGs (HS GAG desulfation); modulate activity of HS GAG by altering binding sites for signaling molecules
Mouse monoclonal [2B4] anti-SULF2 (ab113405) * ^c	1:25	
Rabbit polyclonal anti-SLC26A2 (ab238591) * ^b	1:200	Transmembrane glycoprotein from the solute carrier protein family; involved in the transport of cellular sulfate ions essential for sulfation of HS GAG.
Rabbit polyclonal anti-CD44 (ab157107) * ^b	1:500	Cell-surface receptor for hyaluronan; also binds HS GAG and interacts with Sdcs, collagens, matrix metalloproteinases; involved in cell- interactions, cell adhesion and migration
Mouse monoclonal anti-CD45 (PTPRC) (ab8216) * ^c	1:200	Protein tyrosine phosphatase; type 1 transmembrane protein present in differentiated hematopoietic cells of myeloid and lymphoid lineage (common leukocyte antigen)

Table 1. Cont.

Primary Antibody	Dilution	Description/Function
Rabbit polyclonal anti-RANKL (TNFSF11) (LS-B1425-0.05) † ^b	1:200	Receptor activator of nuclear kappa-B ligand (TNF receptor superfamily); type II membrane protein involved in bone remodeling and immune reactions; promotes differentiation and activation of osteoclasts and specific populations of immune cells
Rabbit polyclonal anti-OPG (TNFRSF11B) (ab73400) * ^b	1:500	Osteoclastogenesis inhibitory factor (TNF receptor superfamily); decoy receptor for RANKL; inhibits osteoclastogenesis and bone resorption

Manufacturer: * Abcam plc, Cambridge, UK; † Seikagaku corp, Tokyo, Japan; ‡ LSBio inc, Seattle, WA, USA
 Secondary antibodies: ^a Donkey polyclonal anti-mouse Alexa Fluor 594 (ab150108); ^b Goat polyclonal anti-rabbit Alexa Fluor 488 (ab150077); ^c Donkey polyclonal anti-mouse Alexa Fluor 488 (ab150105); Secondary antibodies used at dilution 1:400.

2.3. Image Acquisition and Processing

Acquisition and processing of images of histological sections of gingiva have been described previously [18,22,23]. Slides were photographed using the panoramic technique at $\times 10$ magnification with a Zeiss Axiocam 506 digital color camera (resolution 2752×2208 pixels (px)) mounted on a Zeiss Axio Observer inverted epifluorescence microscope (Carl Zeiss Microscopy GmbH; Jena, Germany). Equalization and automatic stitching of the individual photomicrographs (tiles) was performed in the software ZEN Blue 2.5 (Carl Zeiss Microscopy; Jena, Germany) using the “stitching tool” after all tiles had been acquired. The panoramic images were saved in the proprietary Zeiss CZI raw format and exported to the 8-bit TIFF format for further processing.

Panoramic TIFF images were processed using Adobe Photoshop 2020 (Adobe Inc., San Jose, CA, USA) as previously described [18,22]. The processed images were then used for quantification of IF signals and/or IHC staining.

2.4. Histomorphometry and IF Signal Quantification

The procedures for histomorphometry and quantification of IF signals from panoramic images have been described in detail previously [18,22]. Here, we focused exclusively on quantifying the spatial gradients of IF signals, i.e., determining the intensity/amount of IF signal per unit of space. The intensity/amount of IF signals is calculated as the average grey value (GV) or luminance of pixels (px) per unit of space with dimensions of 1 px (height) \times number of px corresponding to the panoramic image width. The values are plotted in a top-down (T-D) 2D plots, which may contain several thousand values for each panoramic image. The T-D plots were created in ImageJ (ImageJ software, U.S. National Institutes of Health, Bethesda, MD, USA) and exported as Excel spreadsheets (Microsoft Office Excel 2016; Microsoft Corporation, Redmond, WA, USA). These were subsequently used for compatibility testing of serial sections (T-D plots of DAPI staining), in silico co-localization of IF from multiple markers, and statistical modeling. For better visual representation of the signal intensity of IF, 4-color heat maps were created. The heatmaps show the distribution of different intensity of IF signals on a scale of 0–255 px GV as follows: BLUE (10–49 px GV; low intensity), GREEN (50–149 px GV; moderate intensity), RED (150–254 px GV; strong intensity), and YELLOW (255 px GV; very strong intensity). The procedure for the making of heatmaps was described previously [24].

2.5. Statistical Analysis and Modeling

Only T-D plots of panoramic images of gingival sections from the periodontitis group were used for statistical modeling. To exclude background px around the histologic sections, values from the raw T-D plots were recalculated as relative values and expressed as percentages of the maximum (MAX) GV as previously described (ref.). T-D plots for each marker were then aggregated and transformed by calculating moving averages at intervals of 5000 data points. The compressed T-D plots (each containing 7000 data points) were then incorporated into a system of regression equations (first-level models) that could be used to simulate the network effects of the interactions between HS GAG, HS GAG-related factors

(HSPGs and enzymes), the inflammatory infiltrate (visualized by the general inflammatory cell marker CD45 (PTPRC)), and alveolar bone degradation/regeneration (RANKL/OPG axis). The advantage of such a system is that each variable can act simultaneously as a predictor (independent variable) and outcome (dependent variable). The template for pairing the variables in the regression equation system was based on the representation of the functional protein network using the STRING reactome database [25]. Because the factors studied belong to the same functional group and are closely related, the construction of the regression equation system was divided into four modules. The main outcome variable from each module was set as the main predictor (link) for the subsequent module until all modules were closed in a loop.

Predictions from the original regression equations were calculated for each outcome variable. Predictions were made by varying the mean spatial gradient value of the predictor in 60 steps from 0 (virtual knockout—VKO) to 4-fold overexpression relative to baseline in diseased gingiva. Predictors were recorded both as the mean spatial gradient of the outcome variable and as the deviation from the mean spatial gradient of the baseline value in diseased gingiva (in percent; % change). For this purpose, another set of matrices was created. These matrices were used to calculate additional regression functions (second-level models) that were incorporated into the final regression equation system (third-level models) for predicting the expression profiles of the factors studied.

Spline (piecewise) regression (SplR) and multiple linear regression (MLR) were used interchangeably for function fitting in first-level models. The knots for SplR were set manually for each pair of variables depending on the shape of the spatial gradient curve. Segments between the knots were fitted either linearly (simple linear regression) or non-linearly (2nd and 3rd order polynomial nonlinear regression). The decision for the type of adjustment was made according to the following guidelines: (i) known effect of the predictor on the outcome variable based on experimental data from the relevant literature dictating the type of correlation between the two (positive correlation, negative correlation, linear, nonlinear); (ii) since data in T-D plots are expressed as percentages (fractions of MAX px GV), the value of the y -axis intercept should be between 0 and 100; (iii) the coefficient of determination (R^2) per segment should not be less than 0.9 to minimize the cumulative error for the model representation of each outcome variable; (iv) for very short segments up to 4 data points, linear fitting is preferred to nonlinear fitting if the y -axis intercept condition is met; (v) the functions included in SplR must reflect the effect of peak or floor plateaus—because the model variables represent ECM components and factors associated with ECM components that exhibit such characteristics, some degree of nonlinearity had to be introduced by SplR for each pair of variables. The second and third level models were fitted with non-linear functions (polynomial regression) only.

According to ASA Statement on Statistical Significance and p -values, p -values for regression tests were presented as calculated and should be interpreted accordingly [26]. Statistical analysis was performed in Microsoft Office Excel 2016 (Microsoft Corporation, Redmond, WA, USA). Regression matrices and calculator for prediction of expression profiles are included in the supplemental material (Supplementary Datasets S1–S4).

3. Results

3.1. Expression of HS GAG and Associated Factors in Healthy Gingiva and in Gingiva of Patients Affected by Periodontitis

Healthy gingival tissue shows an abundance of highly sulfated mucosubstances throughout the subepithelial stroma compared with the subepithelial stroma of gingiva from patients with periodontitis. HS GAGs labeled by HS10E4 and HS3G10 staining are highly expressed in the epithelial compartment of both healthy and diseased gingiva, whereas their expression is sparsely distributed in the subepithelial stroma. The majority of HS GAG in the subepithelial stroma is bound to connective tissue strands and blood vessel walls (Figure 1). Different populations of stromal cells express HS GAG, including fibrocytes, vascular endothelial cells, and inflammatory cells. Similar expression patterns

can be observed for the HS GAG cell surface receptors and enzymes for the synthesis and modification of HS GAG at the interface between infiltrated and noninfiltrated subepithelial stroma and alveolar bone (Figure 2). Comparison of the mean spatial gradients of HS GAG in healthy and diseased gingiva indicates different expression profiles of healthy and diseased gingiva (Figure 3, Supplementary Dataset S3). The latter is characterized by a slightly lower amount of less sulfated HS GAG, a much higher RANKL/OPG ratio and the presence of inflammatory infiltrate (CD45).

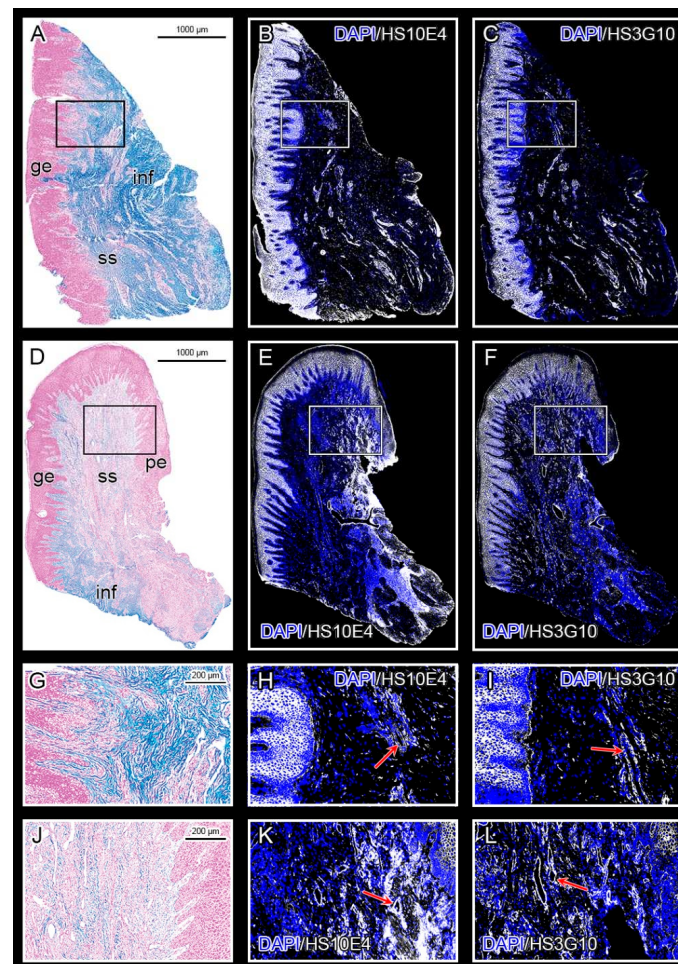


Figure 1. Panoramic images of healthy gingiva (control sample DK -NV2-ZK) (A–C) and diseased gingiva (severe periodontitis sample DK -SL17-CHP) (D–F); Alcian Blue staining (A,D); IF staining with primary antibodies against HS GAG, anti-HS10E4 (B,E) and anti-HS3G10 (C,F); The subepithelial stroma of healthy gingiva is rich in highly sulfated mucosubstances including GAGs (A, blue color), whereas their abundance is reduced in diseased gingiva (D). Reactivity with anti-HS10E4 (marks the sulfated regions of HS GAG chains) and anti-HS3G10 (marks the non-sulfated stumps of HS GAG) is visible mainly in the epithelial compartment of both healthy and diseased gingiva (white color; blue color—DAPI background staining); Reactivity to both antibodies is also seen in the subepithelial stroma (walls of blood vessels, inflammatory infiltrate), although it is more pronounced in the diseased gingiva. Magnified framed areas from Alcian Blue (G,J) and IF (H,I,K,L) panoramic images show the interface between the epithelial compartment and the subepithelial stroma with blood vessels (red arrows) strongly expressing HS GAG. (Magnification: $\times 10$; Designations: gingival epithelium (ge), subepithelial stroma (ss), periodontal pocket epithelium (pe), and inflammatory infiltrate (inf). Image created in Adobe Photoshop 2020, version 21.2.0.

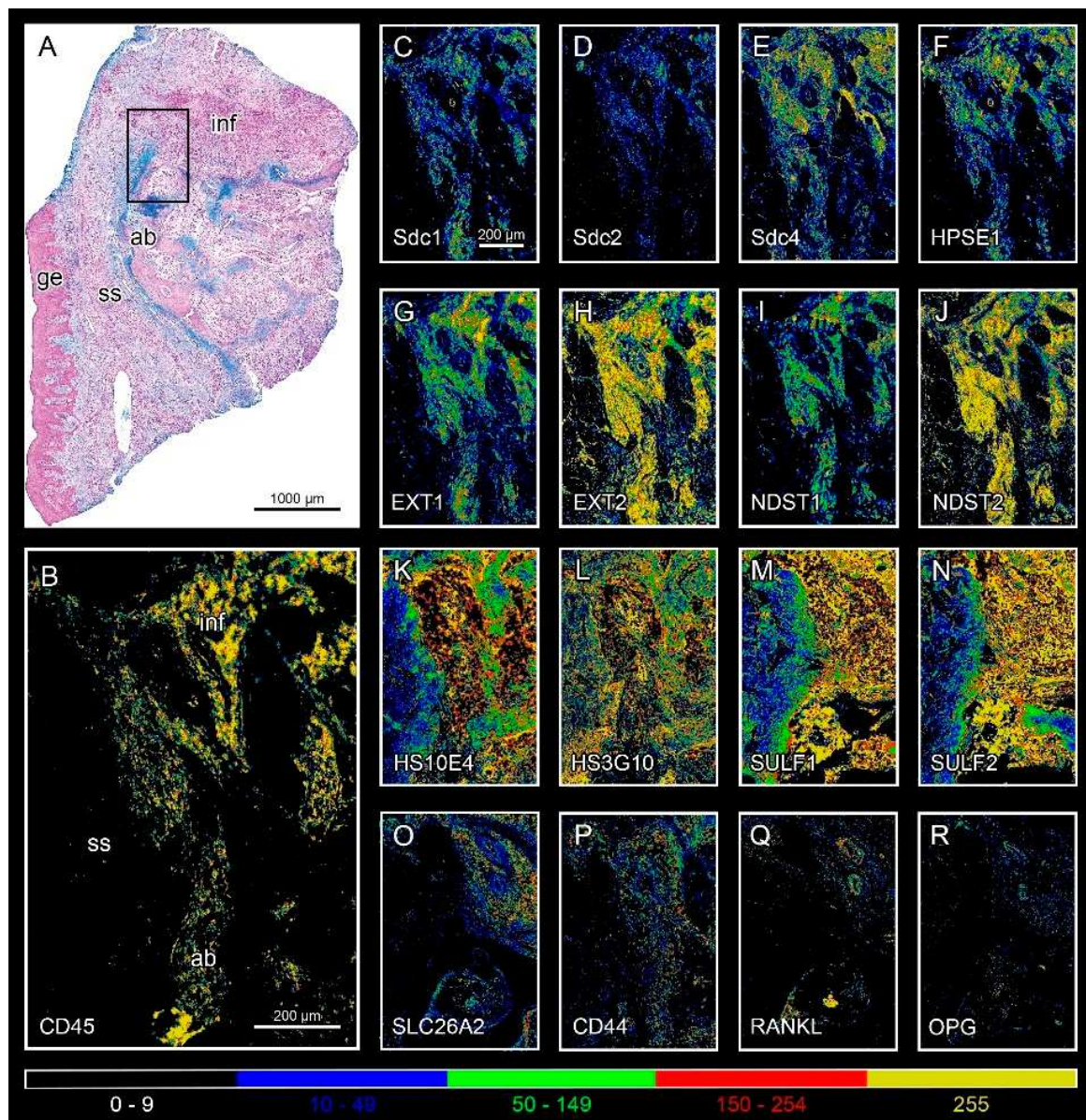


Figure 2. Expression of the studied markers in diseased gingiva (severe periodontitis sample DK-IP13-CHP) at the interface between noninfiltrated subepithelial stroma, alveolar bone, and inflammatory infiltrate (framed area on Alcian Blue panoramic image (A)). All markers are expressed in the area with different intensity (HS GAG cell surface receptors (C–E,P); HS GAG (K,L); HS GAG biosynthesis and degradation factors (F–J,M–O); inflammatory cell marker (CD45) (B); bone resorption/formation markers (RANKL, OPG) (Q,R); heatmap colors represent the intensity of IF signals: background (0–9 px GV; black), weak (10–49 px GV; blue), moderate (50–149 px GV; green), strong (150–254 px GV; red), and very strong intensity (255 px GV; yellow). (Magnification: $\times 10$; Designations: gingival epithelium (ge), subepithelial stroma (ss), alveolar bone (ab), and inflammatory infiltrate (inf)). The image was created with Adobe Photoshop 2020, version 21.2.0.

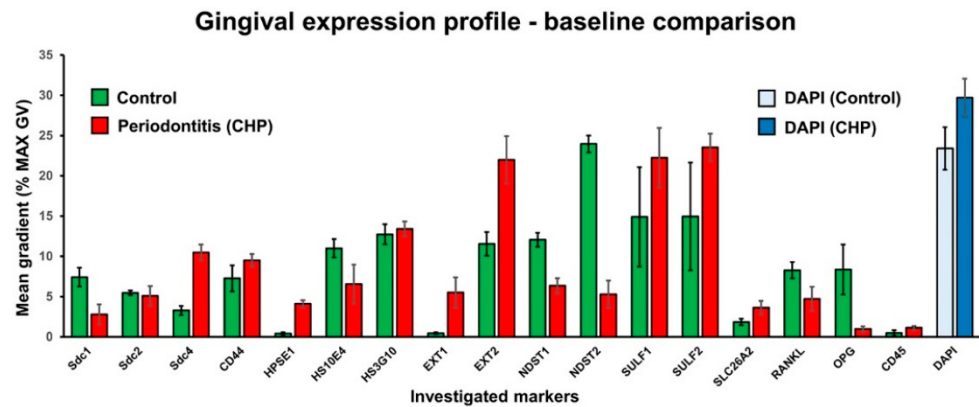


Figure 3. Bar-chart comparison of the expression profiles of the investigated markers in healthy (control) and diseased (severe periodontitis) gingiva samples. The expression of each marker is shown as the mean spatial gradient with standard deviation. The mean spatial gradients of DAPI staining are shown as reference values. The image was processed in Adobe Photoshop 2020, version 21.2.0.

3.2. Parameters of Regression Equation System

Pairing of variables and creation of the regression equation system was done using the STRING reactome network of factors under study as a template (Figure 4). The system consisted of 32 regression equations, of which 22 were SplR pairs, and 11 were MLRs. On average, the goodness of fit for SplRs was $R^2 = 0.99992$ and for MLRs $R^2 = 0.86061$ with $p \approx 0$. A total of 12,342 knots were introduced for SplRs. A detailed list of statistical parameters for the first-level models can be found in Table 2.

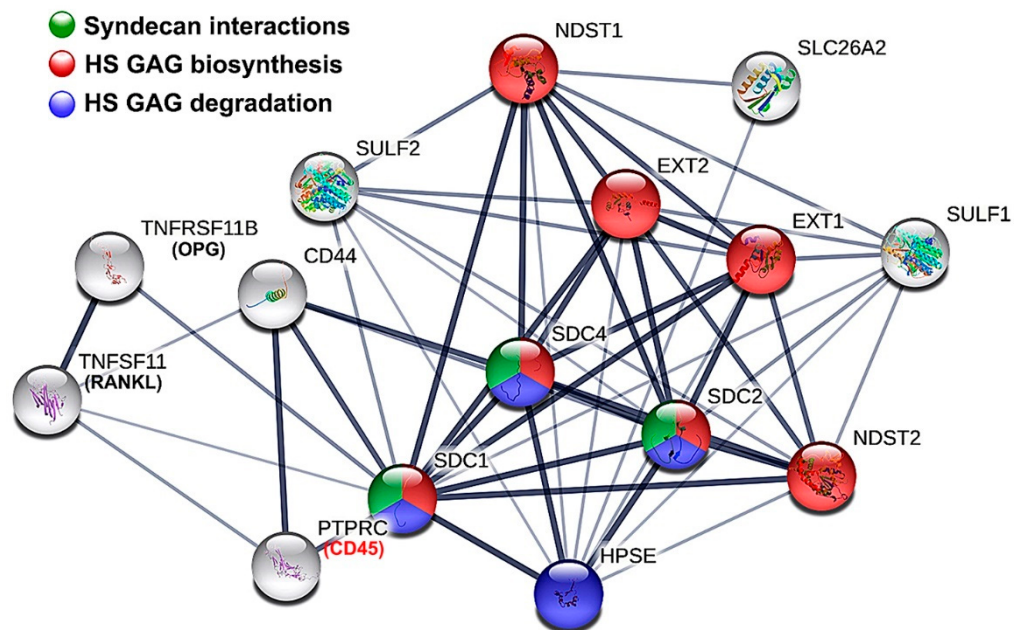


Figure 4. Functional protein network and enrichment from the STRING Reactome database. Network nodes represent the first shell and only 5 proteins from the second shell of interactors. Edges indicate confidence in functional and physical protein association. Colored nodes represent significantly enriched reactome pathways HSA-2022928 (HS GAG biosynthesis), HSA-2024096 (HS GAG degradation) and HSA-3000170 (Sdc interactions). Image processed in Adobe Photoshop 2020, version 21.2.0.

Table 2. Regression parameters for SplR pairs and MLRs in first-level modeling of spatial gradients of investigated markers.

Model Parameters								
Predictors	Marker	Outcomes Mean *	Std. Error	R ²	Df †	FIT ‡	Knots	MODULE §
HPSE1	Sdc1	2.80123	0.03626	0.99912	1		545	
	Sdc2	5.07486	0.00304	0.99999	1	SplR	579	
	Sdc4	10.49152	0.00395	0.99998	1		570	1
Sdcs	HS10E4	6.54086	0.32258	0.98241	3	MLR	N/A	
	HS10E4	6.54091	0.00663	0.99999	1		358	
HS10E4	EXT1	5.50899	0.00479	0.99999	1		226	
	EXT2	21.97313	0.01919	0.99996	1	SplR	188	
	NDST1	6.346521	0.00357	0.99998	1		357	
EXTs, NDSTs	NDST2	5.29767	0.00963	0.99997	1		217	
	HS10E4	6.54091	0.31644	0.99795	4			2
	HS3G10	13.41192	0.42029	0.99902	4	MLR	N/A	
HS10E4	HS10E4	6.54103	0.02772	0.99987	1		185	
	HS3G10	13.41494	0.01222	0.99981	1	SplR	451	
HPSE1, Sdcs, EXTs, NDSTs	SULF1	22.24313	0.55832	0.97743	7			
	SULF2	23.54117	0.34153	0.95915	7	MLR	N/A	
HPSE1, NDST1	SLC26A2	3.62778	0.53376	0.58391	2			
	SULF1	22.24361	0.01709	0.99998	1		642	
SULF2	SULF2	23.54061	0.01529	0.99992	1	SplR	730	3
	SLC26A2	3.62767	0.00372	0.99998	1		646	
SULFs, SLC26A2	HS10E4	6.54181	0.37448	0.97629	3	MLR	N/A	
	HS10E4	6.54103	0.00194	0.99999	1	SplR	1104	
Sdc1	HS10E4	0.97662	0.00158	0.99998	1		454	
	OPG	0.97665	0.00209	0.99996	1	SplR	437	
OPGa, OPGb	OPG	0.97671	0.00125	0.99998	2	MLR	N/A	
	RANKL	4.72004	0.00279	0.99999	1		495	
RANKL/OPG RATIO	CD45	1.11445	0.00105	0.99999	1	SplR	776	
	Sdcs	9.51209	0.64461	0.32535	3	MLR	N/A	
CD44	CD44	9.51218	0.00318	0.99998	1		712	4
	CD45	1.11444	0.00188	0.99993	1	SplR	888	
Sdc1, HS10E4	CD45	1.11445	0.13179	0.66525	2	MLR	N/A	
	CD45	1.11445	0.00076	0.99998	1	SplR	683	
CD45a, CD45b, CD45c	CD45	1.11445	0.00049	0.99999	3	MLR	N/A	
	HPSE1	4.10009	0.00481	0.99989	1	SplR	841	

* Mean value of investigated markers' spatial gradients in diseased gingiva (periodontitis group) calculated from 7000 data points large T-D plots (n = 7000); values measured in % from px MAX GV; † degrees of freedom; ‡ Spline regression (SplR) or multiple regression (MLR) p-value for all models $p \approx 0$ with confidence interval $CI = 10^{-8}$; § Modules for the second- and third-level modeling corresponding to the reconstruction of functional protein network from STRING reactome databa.se.

3.3. The Effects of HPSE1 and Sdcs on the Expression/ECM Content of HS GAG—Module 1

The variables included in Module 1 are as follows: HPSE1 (main predictor), Sdc1–4 (intermediate predictors), and HS10E4 (main outcome; main predictor/link to module 2) (Figure 5A,B). The SplR pairs were modeled according to the well-documented role of HPSE1 as an endoglycosidase enzyme that cleaves HS GAG chains and facilitates shedding of the extracellular domains of Sdc [27–29]. Therefore, VKO or the absence of HPSE1 (–100% of baseline expression measured in diseased gingiva) is predicted to increase the expression of HS GAG and Sdcs. Conversely, overexpression of HPSE1 is predicted to lead to a gradual decrease in the expression of HS GAG and Sdcs. Peak levels at which overexpression of HPSE1 irreversibly downregulates the expression of HS GAG and Sdcs are predicted at 195% (2.95-fold) and 260% (3.6-fold) HPSE1 overexpression for the entire Sdcs complement and HS GAG, respectively. A nonlinear correlation between Sdcs expression and HS GAG is modeled (3rd order polynomial function). Sdcs are major cell surface receptors for HS GAG, and their presence partially overlaps with the expression of HS GAG in the ECM adjacent to cells. Thus, VKO of Sdcs is predicted to decrease the expression of HS GAG by nearly 50% (–2-fold), whereas the steady increase in the total amount of Sdcs positively correlates with the expression of HS GAG, up to a peak

extrapolated at approximately 600% (7-fold) overexpression of Sdcs relative to baseline levels measured in diseased gingiva (Supplementary Datasets S1 and S3).

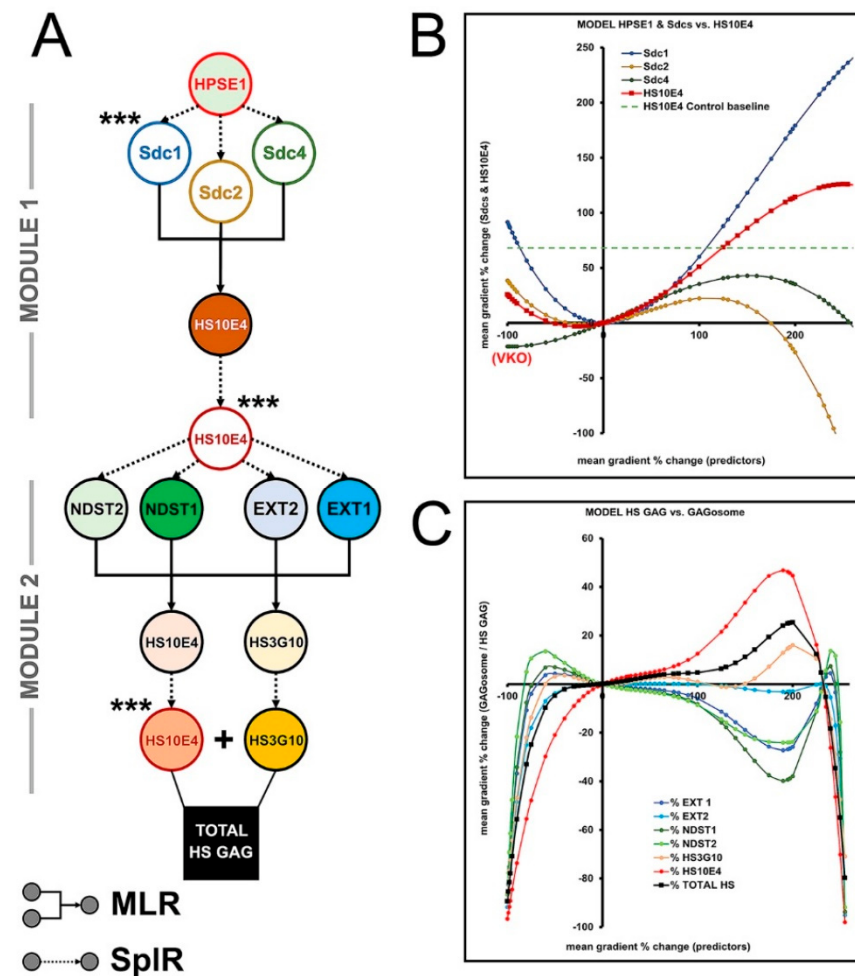


Figure 5. Modeling flowchart (A) and predictions (B,C) for the effects of HPSE1, Sdcs, and GAGosome enzymes on gingival HS GAG—Modules 1 and 2. Nodes in the flowchart represent individual variables. Note that the variables HS10E4 and HS3G10 were modeled iteratively. The total amount of HS GAG was calculated as the sum of HS10E4 and HS3G10 after the last iteration (Module 2). The values on the *x*-axis correspond to the difference between the input and baseline levels of the mean spatial gradients of the predictors measured in the diseased gingiva (severe periodontitis group). The values on the *y*-axis correspond to the difference between the predicted and baseline levels of the mean spatial gradients of the outcome variables measured in the diseased gingiva (severe periodontitis group). (Designations: multiple linear regression (MLR; furnished elbow arrows); spline regression (SplR; dotted arrows); virtual knockout (VKO); *** linking variable to succeeding module(s)). Image processed in Adobe Photoshop 2020, version 21.2.0.

3.4. Biosynthesis of HS GAG and Feedback Loop between HS GAG and GAGosome Enzymes—Module 2

In Module 2, the balance between the ECM-located (external) HS GAG and the newly synthesized intracellular HS GAG was modeled. The latter is represented by four key enzymes responsible for the biosynthesis of HS GAG (EXT1-2, NDST1-2), forming the so-called GAGosome complex in the endoplasmic reticulum (ER) [30,31]. Therefore, the HS10E4 model from Module 1 was set as the main predictor with EXTs and NSDTs as intermediate predictors. Given the known functions of EXTs and NDSTs, HS10E4 and HS3G10 were set as the main outcomes for Module 2, representing total synthesized of HS GAG (HS10E4 + HS3G10) (Figure 5A,C). The assumption that quadruple VKO of EXTs and

NDSTs leads to attenuation of HS GAG synthesis was also introduced. While EXTs have been shown to be essential for HS GAG biosynthesis, there is evidence that EXTs and NDSTs have overlapping functions [32–34]. Together with the relative concentrations of EXTs and NDSTs within the GAGosome complex, this has a major impact on the amount of newly synthesized HS GAG [35]. According to the models from Module 2, the amount of newly synthesized HS GAG varies nonlinearly (6th order polynomial function) as a function of differential expression of EXTs and NDSTs. The peak is predicted at 230% (3.3-fold) overexpression of HS GAG compared to baseline levels in diseased gingiva, after which GAGosome complex shutdown should occur (Figure 5C, Supplementary Datasets S1 and S3).

3.5. The Effects of SULF1-2 and SLC26A2 on Changes in Sulfation of HS GAG—Module 3

Module 3 was added as an open-ended side module to predict variation in sulfation of HS GAG in addition to its initial sulfation by the GAGosome enzymes modeled in Module 2. SLC26A2 and SULF1-2 were set as intermediate predictors with links to multiple variables (main predictors) from Module 1 and Module 2 based on the reconstruction of the STRING reactome network (Figures 4 and 6A,B). SLC26A2 and SULF1-2 affect the sulfation of HS GAG in different ways, with SLC26A2 being a major supplier of sulfate ions (substrate), while SULF1-2 removes sulfate groups at specific sites in HS GAG chains (desulfation) [36–39]. As the main outcome, an artificial HS10E4 model variable was created and used to calculate the corrected values of HS GAG sulfation (expressed as a percentage) according to the simple formula $(HS10E4 / \text{Total HS GAG}) * 100$. Depending on the differential expression of SLC26A2 and SULF1-2, the sulfation of HS GAG is predicted to vary below and above the value measured in healthy gingiva, which is on average 40% (1.4-fold) above the baseline value in diseased gingiva (Figure 6B, Supplementary Datasets S1 and S3).

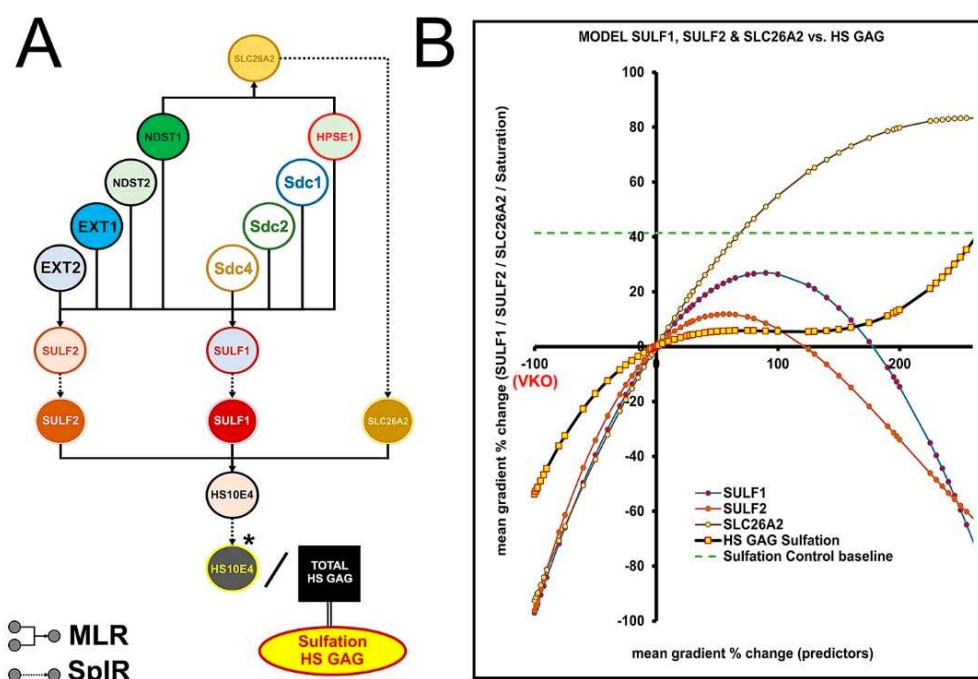


Figure 6. Modeling flowchart (A) and predictions (B) for the effects of SULF1–2 and SLC26A2 on sulfation of HS GAG – Module 3. Note that the artificial variable for HS10E4 was introduced to model the sulfation of HS GAG. The predicted values for the sulfation of HS GAG are below and above the baseline control level. (Designations: multiple linear regression (MLR; bifurcated elbow arrows); spline regression (SpIR; dotted arrows); virtual knockout (VKO); * artificial variable). Image processed in Adobe Photoshop 2020, version 21.2.0.

3.6. Modulation of RANKL/OPG Ratio and CD45 Expression by HS GAG—Module 4

Modulation of the RANKL/OPG ratio and CD45 expression in the gingiva by HS GAG and related factors was modeled in Module 4. Thus, the RANKL/OPG ratio and CD45 were set as the main outcomes, with CD45 being the link variable to Module 1 (via the model variable HPSE1) (Figure 7A). In addition to STRING reactome network reconstruction (Figure 4), these assumptions were also considered for the arrangement of the main predictors (HS10E4, Sdc1, CD44) and the intermediate predictors (artificial variables OPGa–b; CD45a–c): (i) Sdc1 binds to OPG via HS GAG chains, making OPG less available to act as a decoy receptor for RANKL [40–42]. Thus, Sdc1 and HS GAG may shift the RANKL/OPG ratio in favor of RANKL, promoting bone resorption and inflammatory conditions; (ii) depletion of HS GAG content and lack of expression of Sdc1 and CD44 promote inflammatory conditions [43–45]; (iii) overexpression of Sdc1 and CD44 is also observed in some inflammatory conditions [18,46,47]. As predicted by the models in Module 4, VKO and overexpression of HS GAG could have opposite effects on the RANKL/OPG ratio and expression of CD45 (Figure 7B,C). However, the restoration of the RANKL/OPG ratio in healthy gingiva (approximately –80%, –5-fold compared with baseline in diseased gingiva) and CD45 expression (approximately –57%, –2.3-fold compared with baseline in diseased gingiva) could not be predicted for the entire range of HS GAG expression (VKO to 300%, 4-fold overexpression compared with baseline in diseased gingiva) (Supplementary Datasets S1 and S3).

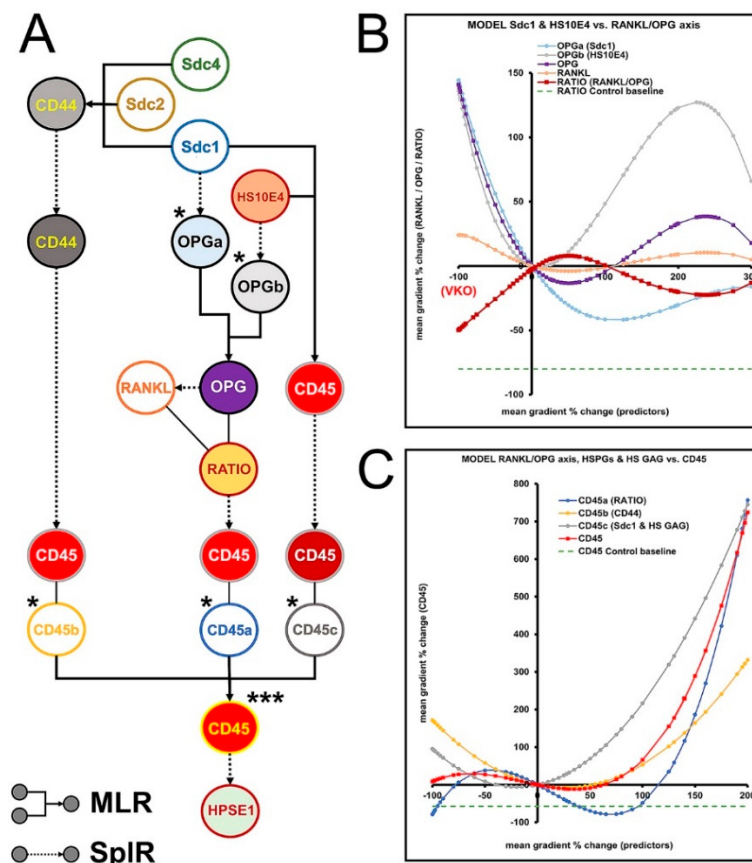


Figure 7. Modeling flowchart (A) and predictions for modulation of RANKL/OPG ratio (B) and CD45 expression (C) by HS GAG – Module 4. Artificial variables for OPG (OPGa–b) and CD45 (CD45a–c) are introduced to model the combined effect of a list of predictors (Sdcs, HS10E4, and CD44) on the main outcomes (RANKL/OPG ratio, CD45). (Designations: multiple linear regression (MLR; furcated elbow arrows); spline regression (SpIR; dotted arrows); virtual knockout (VKO); * artificial variables; *** link variable to Module 1). Image processed in Adobe Photoshop 2020, version 21.2.0.

3.7. Predicted Effects of Native HS GAG on Gingival Inflammatory Infiltrate and Alveolar Bone Formation/Degradation from the Overall Model

The expression profiles for HS GAG, the RANKL/OPG ratio, and CD45 were reproduced considering the cumulative network effect from Modules 1–4 (Figure 8). On this basis, it is predicted that decreasing presence of native HS GAG (from baseline level in diseased gingiva to VKO) decreases the RANKL/OPG ratio, while increasing expression of CD45. Similar effects on RANKL/OPG ratio and CD45 were predicted for overexpression of native HS GAG (200%, 3-fold overexpression from baseline in diseased gingiva). However, a steady increase in native HS GAG to these peaks is predicted to stabilize both the RANKL/OPG ratio and CD45 expression near baseline levels in diseased gingiva (Supplementary Datasets S1, S3, S4).

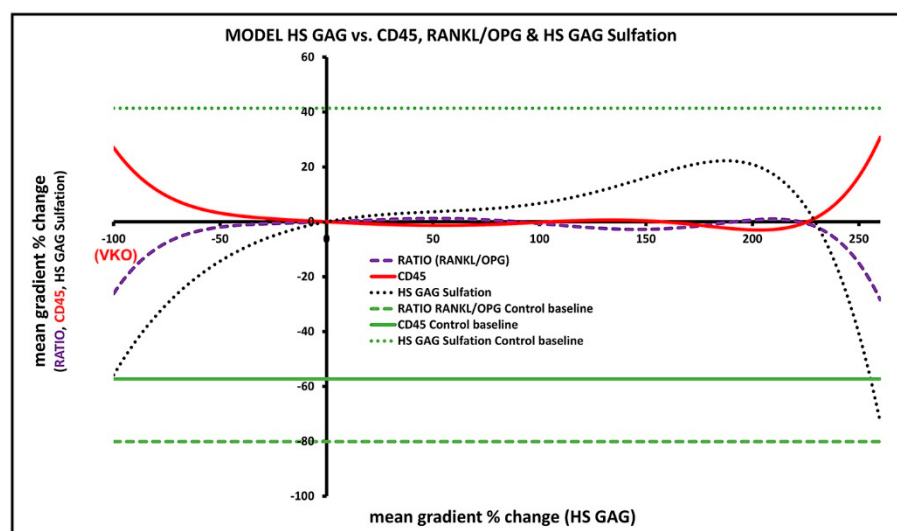


Figure 8. Overall model predictions for the effect of native HS GAG on inflammatory infiltrate in the gingiva and alveolar bone formation/degradation. Note the contrasting effects of altered expression of HS GAG (from VKO to 3.5-fold overexpression of HS GAG from baseline in diseased gingiva) on the RANKL/OPG ratio and CD45. However, for most of the overexpression range, HS GAG is predicted to stabilize the RANKL/OPG ratio and CD45 expression above control values in healthy gingiva. The image was processed in Adobe Photoshop 2020, version 21.2.0.

4. Discussion

The aim of this study was to evaluate the effects of native HS GAG on inflammatory infiltrate formation and alveolar bone resorption in severe periodontitis in humans using statistical modeling of data from IF staining of samples of human gingiva. The amount and structure (sulfation) of HS GAG differ between healthy and diseased gingiva, consistent with different expression profiles of proteins associated with biosynthesis and posttranslational modifications of HS GAG reported in our previous study [18]. The predictions of the statistical model imply that an increasing amount of native HS GAG in diseased gingiva could stabilize the spread of the inflammatory infiltrate and osteoclastogenic activity. On the other hand, the decreased presence (or absence) of native HS GAG could promote the spread of the inflammatory infiltrate while suppressing osteoclastogenic activity by lowering the RANKL/OPG ratio. However, we were unable to predict that increasing or decreasing the presence of native HS GAG in diseased gingiva could reduce formation of the inflammatory infiltrate and osteoclastogenic activity at levels observed in healthy gingiva.

The predictions of our model do not fully support the results of studies on the efficacy of supplementing degraded native HS GAG with its synthetic derivative (HS GAG mimetic) performed on experimental rodent models of periodontitis [16,48–50]. As reported, the administration of synthetic HS GAG was well tolerated by the animals, and the inflammation of soft periodontal tissues was significantly reduced. In addition, there were detectable

signs of periodontal tissue regeneration after treatment with synthetic HS GAG. A proposed explanation was that synthetic HS GAG may be more resistant to fragmentation by degradative enzymes than native HS GAG due to its altered biochemical properties. However, the beneficial effects on periodontal tissue depended on the optimal dosage of synthetic HS GAG - it was found that administration of lower or higher doses may equally exacerbate the course of experimental periodontitis.

In animal models of periodontitis, researchers can replicate the clinical signs (gingivitis, alveolar bone resorption) but not the baseline conditions and the exact pathogenetic mechanism of periodontitis as it occurs in humans [51–55]. Therefore, the significant advantage of the model of periodontitis presented here is that it is based on the raw data obtained from human participants suffering from the real form of severe periodontitis. By combining the data from protein ontology databases and various regression techniques, a dynamic statistical model can be created, in which different roles of the factors under study can be incorporated, while the effects of their changing expression on the outcome(s) of interest can be replicated simultaneously. The arrangement of individual modules, quantification of IF in terms of spatial gradients, and selection of dominant functions for fitting segments in SplR pairs in first-level models were made under the assumption that key determinants of the biological roles of glycans, proteins, and other classes of molecules—hierarchical positioning within regulatory networks and spatial distribution within tissue—are just as important as the biochemical properties of individual molecules [56–58]. The problem with HS GAG and the proteins associated with HS GAG is that their roles in regulating pathogenetic mechanisms are as diverse as they are tissue- and species-specific. It is difficult to study them in humans, where experiments are not possible for ethical reasons. Therefore, the main advantage of this approach is that it shows how the effects of inhibition/absence or overexpression of specific factors (usually achieved by blocking antibodies or knock-out/knockin of the corresponding genes in experimental animals) can be simulated in humans, at least virtually. It should be noted that these effects cannot be predicted simply by comparing the expression profiles of healthy and diseased tissue, nor can they be taken at face value from the studies on experimental animals [51,59].

There are several limitations to this study. Due to ethical considerations in research involving human participants, we could only create in silico model but could not experimentally test it in vivo. We were able to include only a limited number of variables while omitting many factors from the vast HS GAG reactome—these refer to enzymes responsible for HS GAG chain elongation (EXTL1-3), sulfation (NDST3, NDST4, 2-O- and 3-O-sulfotransferases), other cell-surface/ECM proteoglycans that bind HS GAG (agrin, HSPG2, glypicans), and many inflammatory mediators [60,61]. Therefore, certain aspects of the biosynthesis and posttranslational modifications of HS GAG, as well as its role in the formation and maintenance of gradients of inflammatory mediators, could not be modeled. As described previously, this limitation is due to the methodology for quantification and co-localization of IF from multiple markers. It relies on morphological similarity of serial histological sections, which limits the number of different markers whose IF signals can be co-localized (between 20 and 30 markers) [22]. There are additional tradeoffs from the application of IF/IHC and currently available commercial antibodies. For example, fragmentation of HS GAG and shedding of Sdcs cannot be visualized by IF/IHC staining with primary antibodies against HS GAG and Sdcs nor can they be extrapolated by overlapping their expression patterns with those of degradative enzymes such as HPSE1. Specifically, the antibodies against HPSE1 do not distinguish between active and inactive forms (proenzyme) of HPSE1, which means that the observed expression patterns of HPSE1 do not necessarily correspond to the actual enzymatic activity of HPSE1 [18,24]. It must be noted that the statistical model presented here is not deterministic and should be extended. This is a difficult task, both because of the inherent methodological limitations described above and because of the lack of data from experimental in vivo and in vitro studies from which the model assumptions are derived. Nevertheless, statistical modeling of human tissue data may provide an additional tool for evaluating potential molecular targets on

which to base in vivo experiments for alternative treatment of chronic diseases such as severe periodontitis in both experimental animals and human participants. As with other chronic diseases, this may be of particular importance because their complex pathogenic mechanisms cannot be faithfully replicated in controlled laboratory settings.

5. Conclusions

Based on the predictions of our statistical model, we hypothesize that supplementation of native HS GAG may be of some benefit in the treatment of severe periodontitis in humans, but not as a sole treatment, as has been demonstrated in experimental animal models of periodontitis. The model supports the notion that intrinsic changes in the molecular structure of periodontal tissue are critical to the irreversible progression of severe periodontitis. This implies that effectively influencing the host (immune) response to treat severe periodontitis should go beyond the standard approach, which focuses on containing infectious agents from the microbial biofilm. Supplementing and/or targeting degraded ECM components with their synthetic derivatives (such as HS GAG mimetics) could be useful to improve the outcomes of standard treatment of severe forms of periodontitis, which usually falls short of periodontal tissue regeneration. However, more knowledge is needed about the complex biology of HS GAG and the factors associated with HS GAG.

Supplementary Materials: The following supporting information can be downloaded at: <https://www.mdpi.com/article/10.3390/bioengineering9100566/s1>, Supplementary Dataset S1: First and second level models – Regression matrices; Dataset S2: Second level models—Calculator; Dataset S3: Data for Results section; Dataset S4: Third level models—Regression matrices.

Author Contributions: Conceptualization, D.K.; methodology, R.D., M.R. and D.K.; validation, R.D., M.R., D.B. and D.K.; formal analysis, D.K.; investigation, R.D., M.R., D.B. and D.K.; resources, M.R. and D.B.; data curation, R.D. and D.K.; writing—original draft preparation, R.D. and D.K.; writing—review and editing, R.D., M.R. and D.K.; writing—review: D.B.; visualization, R.D. and D.K.; supervision, D.K.; funding acquisition, R.D., D.B. and D.K. All authors have read and agreed to the published version of the manuscript.

Funding: R.D. was supported by PhD students grant (University of Split, School of Medicine); D.B. was supported by the annual researcher grant (University of Zagreb); D.K. was supported by the annual researcher grant (University of Split).

Institutional Review Board Statement: The study was conducted in accordance with the Declaration of Helsinki and approved by the Ethics and Drug Committee of SCHOOL OF MEDICINE, UNIVERSITY OF SPLIT (Class: 003-08/17-03/0001, No: 2181-198-03-04-17-0043) and by the Ethics and Drug Committee of SCHOOL OF DENTAL MEDICINE, UNIVERSITY OF ZAGREB (No: 05- PA -15-6/2017).

Informed Consent Statement: Informed consent was obtained from all subjects involved.

Data Availability Statement: Data is contained within the article and Supplementary Material.

Acknowledgments: We wish to thank Asja Miletic and Marica Maretic for their expert technical assistance in preparation of histological slides. Special thanks to Marina Degoricija for providing us with beautiful (and very useful) reactome schematics from STRING database.

Conflicts of Interest: The authors declare no conflict of interest.

References

1. Slots, J. Periodontitis: Facts, fallacies and the future. *Periodontology 2000* **2017**, *75*, 7–23. [[CrossRef](#)] [[PubMed](#)]
2. Tonetti, M.S.; Greenwell, H.; Kornman, K.S. Staging and grading of periodontitis: Framework and proposal of a new classification and case definition. *J. Periodontol.* **2018**, *89* (Suppl. 1), S159–S172. [[CrossRef](#)] [[PubMed](#)]
3. Tonetti, M.S.; Jepsen, S.; Jin, L.; Otomo-Corgel, J. Impact of the global burden of periodontal diseases on health, nutrition and wellbeing of mankind: A call for global action. *J. Clin. Periodontol.* **2017**, *44*, 456–462. [[CrossRef](#)] [[PubMed](#)]
4. Alexopoulou, A.N.; Multhaupt, H.A.; Couchman, J.R. Syndecans in wound healing, inflammation and vascular biology. *Int. J. Biochem. Cell Biol.* **2007**, *39*, 505–528. [[CrossRef](#)] [[PubMed](#)]

5. Bonnans, C.; Chou, J.; Werb, Z. Remodelling the extracellular matrix in development and disease. *Nat. Rev. Mol. Cell Biol.* **2014**, *15*, 786–801. [[CrossRef](#)] [[PubMed](#)]
6. Stepp, M.A.; Pal-Ghosh, S.; Tadvalkar, G.; Pajoohesh-Ganji, A. Syndecan-1 and Its Expanding List of Contacts. *Adv. Wound Care* **2015**, *4*, 235–249. [[CrossRef](#)] [[PubMed](#)]
7. Teng, Y.H.-F.; Aquino, R.S.; Park, P.W. Molecular functions of syndecan-1 in disease. *Matrix Biol.* **2012**, *31*, 3–16. [[CrossRef](#)] [[PubMed](#)]
8. Gopal, S. Syndecans in Inflammation at a Glance. *Front. Immunol.* **2020**, *11*, 227. [[CrossRef](#)]
9. Szatmári, T.; Mundt, F.; Heidari-Hamedani, G.; Zong, F.; Ferolla, E.; Alexeyenko, A.; Hjerpe, A.; Dobra, K. Novel Genes and Pathways Modulated by Syndecan-1: Implications for the Proliferation and Cell-Cycle Regulation of Malignant Mesothelioma Cells. *PLoS ONE* **2012**, *7*, e48091. [[CrossRef](#)] [[PubMed](#)]
10. Esztermáry, T.; Edobra, K. The Role of Syndecan-1 in Cellular Signaling and its Effects on Heparan Sulfate Biosynthesis in Mesenchymal Tumors. *Front. Oncol.* **2013**, *3*, 310. [[CrossRef](#)]
11. Talsma, D.T.; Katta, K.; Ettema, M.A.B.; Kel, B.; Kusche-Gullberg, M.; Daha, M.R.; Stegeman, C.A.; van den Born, J.; Wang, L. Endothelial heparan sulfate deficiency reduces inflammation and fibrosis in murine diabetic nephropathy. *Lab. Invest.* **2018**, *98*, 427–438. [[CrossRef](#)] [[PubMed](#)]
12. Sanderson, R.D.; Elkin, M.; Rapraeger, A.C.; Ilan, N.; Vlodavsky, I. Heparanase regulation of cancer, autophagy and inflammation: New mechanisms and targets for therapy. *FEBS J.* **2016**, *284*, 42–55. [[CrossRef](#)] [[PubMed](#)]
13. Na Ge, X.; Bastan, I.; Gil Ha, S.; Greenberg, Y.G.; Esko, J.D.; Rao, S.P.; Sriramarao, P. Regulation of eosinophil recruitment and allergic airway inflammation by heparan sulfate proteoglycan (HSPG) modifying enzymes. *Exp. Lung Res.* **2018**, *44*, 98–112. [[CrossRef](#)]
14. Andreas, D. Implications of Heparan Sulfate and Heparanase in Inflammatory Diseases. Ph.D. Dissertation, Uppsala University, Uppsala, Sweden, 2017.
15. Sanz, M.; Herrera, D.; Kebschull, M.; Chapple, I.; Jepsen, S.; Berglundh, T.; Sculean, A.; Tonetti, M.S.; Aass, A.M.; Aimetti, M.; et al. Treatment of stage I–III periodontitis—The EFP S3 level clinical practice guideline. *J. Clin. Periodontol.* **2020**, *47* (Suppl. 22), 4–60. [[CrossRef](#)] [[PubMed](#)]
16. Coyac, B.R.; Detzen, L.; Doucet, P.; Baroukh, B.; Llorens, A.; Bonnaure-Mallet, M.; Gosset, M.; Barritault, D.; Colombier, M.-L.; Saffar, J.-L. Periodontal reconstruction by heparan sulfate mimetic-based matrix therapy in *Porphyromonas gingivalis*-infected mice. *Heliyon* **2018**, *4*, e00719. [[CrossRef](#)]
17. Papapanou, P.N.; Sanz, M.; Buduneli, N.; Dietrich, T.; Feres, M.; Fine, D.H.; Flemmig, T.F.; Garcia, R.; Giannobile, W.V.; Graziani, F.; et al. Periodontitis: Consensus report of workgroup 2 of the 2017 World Workshop on the Classification of Periodontal and Peri-Implant Diseases and Conditions. *J. Periodontol.* **2018**, *89* (Suppl. 1), S173–S182. [[CrossRef](#)]
18. Duplancic, R.; Roguljic, M.; Puhar, I.; Vecek, N.; Dragun, R.; Vukojevic, K.; Saraga-Babic, M.; Kero, D. Syndecans and Enzymes for Heparan Sulfate Biosynthesis and Modification Differentially Correlate With Presence of Inflammatory Infiltrate in Periodontitis. *Front. Physiol.* **2019**, *10*, 1248. [[CrossRef](#)]
19. World Medical Association. World Medical Association Declaration of Helsinki: Ethical principles for medical research involving human subjects. *JAMA* **2013**, *310*, 2191–2194. [[CrossRef](#)]
20. Kero, D.; Cigic, L.; Mikic, I.M.; Galic, T.; Cubela, M.; Vukojevic, K.; Saraga-Babic, M. Involvement of IGF-2, IGF-1R, IGF-2R and PTEN in development of human tooth germ—An immunohistochemical study. *Organogenesis* **2016**, *12*, 152–167. [[CrossRef](#)]
21. Kero, D.; Vukojevic, K.; Stazic, P.; Sundov, D.; Brakus, S.M.; Saraga-Babic, M. Regulation of proliferation in developing human tooth germs by MSX homeodomain proteins and cyclin-dependent kinase inhibitor p19INK4d. *Organogenesis* **2017**, *13*, 141–155. [[CrossRef](#)]
22. Duplancic, R.; Kero, D. Novel approach for quantification of multiple immunofluorescent signals using histograms and 2D plot profiling of whole-section panoramic images. *Sci. Rep.* **2021**, *11*, 8619. [[CrossRef](#)] [[PubMed](#)]
23. Kero, D.; Čavar, I. Correlation of the expression of hyaluronan and CD44 with the presence of gingival inflammatory infiltrate in advanced generalized periodontitis. *St Open* **2020**, *1*, 1–16. [[CrossRef](#)]
24. Kero, D.; Bilandzija, T.S.; Arapovic, L.L.; Vukojevic, K.; Saraga-Babić, M. Syndecans and Enzymes Involved in Heparan Sulfate Biosynthesis and Degradation Are Differentially Expressed During Human Odontogenesis. *Front. Physiol.* **2018**, *9*, 732. [[CrossRef](#)] [[PubMed](#)]
25. von Mering, C.; Huynen, M.; Jaeggi, D.; Schmidt, S.; Bork, P.; Snel, B. STRING: A database of predicted functional associations between proteins. *Nucleic Acids Res.* **2003**, *31*, 258–261. [[CrossRef](#)]
26. Yaddanapudi, L.N. The American Statistical Association statement on *P*-values explained. *J. Anaesthesiol. Clin. Pharmacol.* **2016**, *32*, 421–423. [[CrossRef](#)] [[PubMed](#)]
27. Jin, H.; Zhou, S.; Yang, S.; Cao, H.-M. Heparanase overexpression down-regulates syndecan-1 expression in a gallbladder carcinoma cell line. *J. Int. Med Res.* **2017**, *45*, 662–672. [[CrossRef](#)] [[PubMed](#)]
28. David, G.; Zimmermann, P. Heparanase tailors syndecan for exosome production. *Mol. Cell. Oncol.* **2016**, *3*, e1047556. [[CrossRef](#)] [[PubMed](#)]
29. Yu, S.; Lv, H.; Zhang, H.; Jiang, Y.; Hong, Y.; Xia, R.; Zhang, Q.; Ju, W.; Jiang, L.; Ou, G.; et al. Heparanase-1-induced shedding of heparan sulfate from syndecan-1 in hepatocarcinoma cell facilitates lymphatic endothelial cell proliferation via VEGF-C/ERK pathway. *Biochem. Biophys. Res. Commun.* **2017**, *485*, 432–439. [[CrossRef](#)] [[PubMed](#)]

30. Esko, J.D.; Selleck, S.B. Order Out of Chaos: Assembly of Ligand Binding Sites in Heparan Sulfate. *Annu. Rev. Biochem.* **2002**, *71*, 435–471. [[CrossRef](#)]
31. Carlsson, P.; Presto, J.; Spillmann, D.; Lindahl, U.; Kjellén, L. Heparin/Heparan Sulfate Biosynthesis: Processive formation of N-sulfated domains. *J. Biol. Chem.* **2008**, *283*, 20008–20014. [[CrossRef](#)]
32. McCormick, C.; LeDuc, Y.; Martindale, D.; Mattison, K.; Esford, L.; Dyer, A.; Tufaro, F. The putative tumour suppressor EXT1 alters the expression of cell-surface heparan sulfate. *Nat. Genet.* **1998**, *19*, 158–161. [[CrossRef](#)] [[PubMed](#)]
33. Presto, J.; Thuveson, M.; Carlsson, P.; Busse, M.; Wilén, M.; Eriksson, I.; Kusche-Gullberg, M.; Kjellén, L. Heparan sulfate biosynthesis enzymes EXT1 and EXT2 affect NDST1 expression and heparan sulfate sulfation. *Proc. Natl. Acad. Sci. USA* **2008**, *105*, 4751–4756. [[CrossRef](#)]
34. Deligny, A.; Dierker, T.; Dagälv, A.; Lundequist, A.; Eriksson, I.; Nairn, A.; Moremen, K.W.; Merry, C.; Kjellén, L. NDST2 (N-Deacetylase/N-Sulfotransferase-2) Enzyme Regulates Heparan Sulfate Chain Length. *J. Biol. Chem.* **2016**, *291*, 18600–18607. [[CrossRef](#)] [[PubMed](#)]
35. Zhang, X.; Wang, F.; Sheng, J. “Coding” and “Decoding”: Hypothesis for the regulatory mechanism involved in heparan sulfate biosynthesis. *Carbohydr. Res.* **2016**, *428*, 1–7. [[CrossRef](#)] [[PubMed](#)]
36. Buresh-Stiemke, R.A.; Malinowski, R.L.; Keil, K.P.; Vezina, C.M.; Oosterhof, A.; Van Kuppevelt, T.H.; Marker, P.C. Distinct expression patterns of *Sulf1* and *Hs6st1* spatially regulate heparan sulfate sulfation during prostate development. *Dev. Dyn.* **2012**, *241*, 2005–2013. [[CrossRef](#)]
37. Kim, H.-J.; Kim, H.-S.; Hong, Y.-H. Sulfatase 1 and sulfatase 2 as novel regulators of macrophage antigen presentation and phagocytosis. *Yeungnam Univ. J. Med.* **2021**, *38*, 326–336. [[CrossRef](#)]
38. Hästbacka, J.; Superti-Furga, A.; Wilcox, W.R.; Rimoin, D.L.; Cohn, D.H.; Lander, E.S. Atelosteogenesis type II is caused by mutations in the diastrophic dysplasia sulfate-transporter gene (DTDST): Evidence for a phenotypic series involving three chondrodysplasias. *Am. J. Hum. Genet.* **1996**, *58*, 255–262.
39. Alper, S.L.; Sharma, A.K. The SLC26 gene family of anion transporters and channels. *Mol. Asp. Med.* **2013**, *34*, 494–515. [[CrossRef](#)]
40. Kelly, T.; Suva, L.J.; Nicks, K.M.; MacLeod, V.; Sanderson, R.D. Tumor-derived syndecan-1 mediates distal cross-talk with bone that enhances osteoclastogenesis. *J. Bone Miner. Res.* **2010**, *25*, 1295–1304. [[CrossRef](#)]
41. Benad-Mehner, P.; Thiele, S.; Rachner, T.D.; Göbel, A.; Rauner, M.; Hofbauer, L.C. Targeting syndecan-1 in breast cancer inhibits osteoclast functions through up-regulation of osteoprotegerin. *J. Bone Oncol.* **2013**, *3*, 18–24. [[CrossRef](#)]
42. Timmen, M.; Hidding, H.; Götte, M.; El Khassawna, T.; Kronenberg, D.; Stange, R. The heparan sulfate proteoglycan Syndecan-1 influences local bone cell communication via the RANKL/OPG axis. *Sci. Rep.* **2020**, *10*, 20510. [[CrossRef](#)] [[PubMed](#)]
43. Agere, S.A.; Kim, E.Y.; Akhtar, N.; Ahmed, S. Syndecans in chronic inflammatory and autoimmune diseases: Pathological insights and therapeutic opportunities. *J. Cell. Physiol.* **2017**, *233*, 6346–6358. [[CrossRef](#)] [[PubMed](#)]
44. Morla, S. Glycosaminoglycans and Glycosaminoglycan Mimetics in Cancer and Inflammation. *Int. J. Mol. Sci.* **2019**, *20*, 1963. [[CrossRef](#)] [[PubMed](#)]
45. Misra, S.; Hascall, V.C.; Markwald, R.R.; Ghatak, S. Interactions between Hyaluronan and Its Receptors (CD44, RHAMM) Regulate the Activities of Inflammation and Cancer. *Front. Immunol.* **2015**, *6*, 201. [[CrossRef](#)] [[PubMed](#)]
46. Nedvetzki, S.; Gonen, E.; Assayag, N.; Reich, R.; Williams, R.O.; Thurmond, R.L.; Huang, J.-F.; Neudecker, B.A.; Wang, F.-S.; Turley, E.A.; et al. RHAMM, a receptor for hyaluronan-mediated motility, compensates for CD44 in inflamed CD44-knockout mice: A different interpretation of redundancy. *Proc. Natl. Acad. Sci. USA* **2004**, *101*, 18081–18086. [[CrossRef](#)]
47. Man, M.; Elias, P.M.; Man, W.; Wu, Y.; Bourguignon, L.Y.W.; Feingold, K.R.; Man, M.-Q. The role of CD44 in cutaneous inflammation. *Exp. Dermatol.* **2009**, *18*, 962–968. [[CrossRef](#)] [[PubMed](#)]
48. Escartin, Q.; Lallam-Laroye, C.; Baroukh, B.; Morvan, F.O.; Caruelle, J.P.; Godeau, G.; Barritault, D.; Saffar, J.-L. A new approach to treat tissue destruction in periodontitis with chemically modified dextran polymers. *FASEB J.* **2003**, *17*, 644–651. [[CrossRef](#)] [[PubMed](#)]
49. Lallam-Laroye, C.; Escartin, Q.; Zlowodzki, A.-S.; Barritault, D.; Caruelle, J.-P.; Baroukh, B.; Saffar, J.-L.; Colombier, M.-L. Periodontitis destructions are restored by synthetic glycosaminoglycan mimetic. *J. Biomed. Mater. Res. Part A* **2006**, *79*, 675–683. [[CrossRef](#)] [[PubMed](#)]
50. Lallam-Laroye, C.; Baroukh, B.; Doucet, P.; Barritault, D.; Saffar, J.-L.; Colombier, M.-L. ReGeneraTing Agents Matrix Therapy Regenerates a Functional Root Attachment in Hamsters with Periodontitis. *Tissue Eng. Part A* **2011**, *17*, 2359–2367. [[CrossRef](#)] [[PubMed](#)]
51. De Vries, T.J.; Andreotta, S.; Loos, B.G.; Nicu, E.A. Genes Critical for Developing Periodontitis: Lessons from Mouse Models. *Front. Immunol.* **2017**, *8*, 1395. [[CrossRef](#)] [[PubMed](#)]
52. Marchesan, J.; Girnary, M.S.; Jing, L.; Miao, M.Z.; Zhang, S.; Sun, L.; Morelli, T.; Schoenfish, M.H.; Inohara, N.; Offenbacher, S.; et al. An experimental murine model to study periodontitis. *Nat. Protoc.* **2018**, *13*, 2247–2267. [[CrossRef](#)] [[PubMed](#)]
53. Martinon, P.; Fraticelli, L.; Giboreau, A.; Dussart, C.; Bourgeois, D.; Carrouel, F. Nutrition as a Key Modifiable Factor for Periodontitis and Main Chronic Diseases. *J. Clin. Med.* **2021**, *10*, 197. [[CrossRef](#)] [[PubMed](#)]
54. Khocht, A.; Orlich, M.; Paster, B.; Bellinger, D.; Lenoir, L.; Irani, C.; Fraser, G. Cross-sectional comparisons of subgingival microbiome and gingival fluid inflammatory cytokines in periodontally healthy vegetarians versus non-vegetarians. *J. Periodontal Res.* **2021**, *56*, 1079–1090. [[CrossRef](#)] [[PubMed](#)]

55. Silva, N.; Abusleme, L.; Bravo, D.; Dutzan, N.; Garcia-Sesnich, J.; Vernal, R.; Hernández, M.; Gamonal, J. Host response mechanisms in periodontal diseases. *J. Appl. Oral Sci.* **2015**, *23*, 329–355. [[CrossRef](#)] [[PubMed](#)]
56. Schubert, W.; Bonnekoh, B.; Pommer, A.J.; Philipsen, L.; Böckelmann, R.; Malykh, Y.; Gollnick, H.; Friedenberger, M.; Bode, M.; Dress, A.W.M. Analyzing proteome topology and function by automated multidimensional fluorescence microscopy. *Nat. Biotechnol.* **2006**, *24*, 1270–1278. [[CrossRef](#)] [[PubMed](#)]
57. Park, C.C.; Georgescu, W.; Polyzos, A.; Pham, C.; Ahmed, K.M.; Zhang, H.; Costes, S.V. Rapid and automated multidimensional fluorescence microscopy profiling of 3D human breast cultures. *Integr. Biol.* **2013**, *5*, 681–691. [[CrossRef](#)] [[PubMed](#)]
58. Kero, D.; Saraga-Babic, M. Odontogenesis—A Masterful Orchestration of Functional Redundancy or What Makes Tooth Bioengineering an Intrinsically Difficult Concept. *Int. J. Stem Cell Res. Ther.* **2016**, *1*, 7. [[CrossRef](#)]
59. Zhang, S.; Yu, N.; Arce, R.M. Periodontal inflammation: Integrating genes and dysbiosis. *Periodontology 2000* **2020**, *82*, 129–142. [[CrossRef](#)]
60. Chanalaris, A.; Clarke, H.; Guimond, S.E.; Vincent, T.L.; Turnbull, J.E.; Troeberg, L. Heparan Sulfate Proteoglycan Synthesis Is Dysregulated in Human Osteoarthritic Cartilage. *Am. J. Pathol.* **2019**, *189*, 632–647. [[CrossRef](#)] [[PubMed](#)]
61. Bishop, J.R.; Schuksz, M.; Esko, J.D. Heparan sulphate proteoglycans fine-tune mammalian physiology. *Nature* **2007**, *446*, 1030–1037. [[CrossRef](#)]